

A Unified Framework for Evaluating Microscopic Pedestrian Simulation Models

DISSERTATION

submitted in partial fulfillment of the requirements for the degree of

Doktor der Technischen Wissenschaften

by

Dipl.-Ing.(FH) Stefan Seer

Registration Number 0826992

to the Faculty of Informatics
at the Vienna University of Technology

Advisor: Ao.Univ.Prof.i.R. Dipl.-Ing. Dr.rer.nat. Dr.sc.med. Dr.techn. Frank Rattay

The dissertation has been reviewed by:

Frank Rattay

Dietmar Bauer

Vienna, 21st August, 2015

Stefan Seer

Erklärung zur Verfassung der Arbeit

Dipl.-Ing.(FH) Stefan Seer
Karajangasse 6/32, 1200 Wien

Hiermit erkläre ich, dass ich diese Arbeit selbständig verfasst habe, dass ich die verwendeten Quellen und Hilfsmittel vollständig angegeben habe und dass ich die Stellen der Arbeit – einschließlich Tabellen, Karten und Abbildungen –, die anderen Werken oder dem Internet im Wortlaut oder dem Sinn nach entnommen sind, auf jeden Fall unter Angabe der Quelle als Entlehnung kenntlich gemacht habe.

Wien, 21. August 2015

Stefan Seer

To my family.

Acknowledgements

Foremost, I would like to express my appreciation to Prof. Frank Rattay for his guidance during my doctoral research endeavor for the past years. In particular, I would like to thank Prof. Dietmar Bauer for being an immense source of inspiration and knowledge, and for agreeing to evaluate this thesis.

Most of the work contained in this thesis has been possible only because of the help of the great people at the Dynamic Transportation Systems group at the Austrian Institute of Technology. I want to thank all of them, and in particular Dr. Norbert Brändle, Dr. Christian Rudloff, Christian Kogler, Thomas Matyus, Martin Stubenschrott, Helmut Schrom-Feiertag, and Silvia Klettner for their extremely valuable contributions and stimulating discussions. My appreciation also goes to Martin Höfner for all the times in which his assistance helped me along the way.

A central role in the development of this research had the MIT Senseable City Lab with its brilliant people and ideas. I am particularly grateful to Prof. Carlo Ratti for giving me the opportunity of being part of his team and for inspiring and supporting my work.

I am very grateful to Katja Schechtner for mentoring and encouraging me since the beginning of my professional career. I greatly value her friendship and moral support that helped me to overcome setbacks.

As for everything else I do, I am truly and deeply thankful to my family for their continuous support and love over the years. I am also grateful to my dear friends for their understanding and for keeping me calm and then again finding the right way to push me forward.

I owe my gratitude to all these wonderful people. Without their invaluable support I may not have gotten to where I am today.

Kurzfassung

Mikroskopische Simulationsmodelle werden in vielen Anwendungen zur Vorhersage von Fußgängerströmen mit hoher Granularität verwendet. Sie haben sich als ein wertvolles Instrument bewährt, das die Entwicklung und Evaluierung von Architekturplänen unterstützt, Verkehrsnachfragen und -kapazitäten abschätzt, die Sicherheit, Effizienz und Komfort in stark frequentierten Bereichen erhöht und Szenarien für Notevakuierungen analysiert. Wenngleich in der wissenschaftlichen Literatur eine Vielzahl von mikroskopischen Modellen verfügbar ist, ermöglichen aktuell implementierte Simulatoren in der Regel keinen einfachen und schnellen Wechsel zwischen einzelnen Modellen noch geben diese Einsicht in Details zu ihrer Funktionalität und Implementierung preis. Darüber hinaus mangelt es noch an zuverlässigen menschlichen Bewegungsdaten, welche jedoch eine Voraussetzung für die Entwicklung von realitätsnahen Modellen sowie für die Modellkalibrierung und -validierung darstellen. Diese Defizite hemmen die Evaluierung der Fähigkeiten verschiedener Modelle. Dadurch werden quantitative Vergleiche zwischen verschiedenen Ansätzen derzeit nur selten durchgeführt.

Diese Doktorarbeit entwickelt erstmals ein einheitliches Framework zur strukturierten Untersuchung der Stärken und Schwächen von verschiedenen mikroskopischen Fußgängersimulationsmodellen auf Basis eines empirischen Referenzdatensatzes und der Implementierung dieser Modelle in einem Simulations-Framework.

Die empirische Grundlage dieser Arbeit stellt ein hochgenauer Referenzdatensatz mit 2674 Personentrajektorien dar, welcher unter realen Bedingungen in einem bidirektionalen Korridor mit einem neuartigen Ansatz zur Datenerfassung unter Verwendung des Low-Cost-Sensors Microsoft Kinect gemessen wurde. Dieser innovative Algorithmus zur Erkennung und Verfolgung von Personen basiert auf agglomerativem Clustering von anonymisierten Tiefendaten, welche von einem erhöhten Blickwinkel mit mehreren Kinects erfasst werden. Die Pedestrian Detection Rate beträgt bis zu 94% bei einer Multiple Object Tracking Precision von 4 cm.

Das präsentierte Simulations-Framework besteht aus einer skalierbaren und flexiblen Systemarchitektur, welche die einfache Integration unterschiedlicher Simulationsmodelle und damit die konsistente und effiziente Kalibrierung und Validierung von Modellen ermöglicht. Drei Ansätze des Social Force Modells, ein Cellular Automaton Modell, das Optimal Reciprocal Collision Avoidance Modell und zwei Varianten des Optimal Steps Modell wurden in das Simulations-Framework implementiert. Als ersten Schritt in Richtung Verifizierung und Validierung der Modelle, wurden ausgewählte Testfälle

der RiMEA-Richtlinie simuliert, welche die Definition eines Mindeststandards für Evaluierungsanalysen anstrebt. Das Potential des Simulations-Frameworks für einfaches und schnelles Umschalten und Kombinieren von Modellen wird anhand von zwei realen Fallstudien gezeigt: zwei Versionen des Social Force Ansatzes sowie das Optimal Reciprocal Collision Avoidance Modell werden innerhalb des Frameworks für die Simulation des Fahrgastwechsels in einem Zug angewendet. Zusätzlich wird die Fähigkeit des Simulations-Frameworks demonstriert, Modellansätze mit unterschiedlicher Granularität für hohe Passagierströme in einer U-Bahnstation zu kombinieren.

In der Evaluierung werden die Prognosen der sieben im Simulations-Framework implementierten Modelle mit den empirischen Referenzdatensatz aus dem Kinect-basierten Tracking sowie untereinander verglichen. Um eine einheitliche Grundlage für den Vergleich herzustellen, wurden die untersuchten Modelle zuerst auf einem Teil des Referenzdatensatzes kalibriert. Zwei Methoden zur Kalibrierung von Social Force basierten Modellen auf Basis von individuellen Trajektorien werden präsentiert – Modellschätzung durch das nichtlineare Least-Square-Verfahren und der Vergleich von realen und simulierten Trajektorien. Darüber hinaus wurde eine strukturierte Evaluierungsumgebung entwickelt, die auf Kriterien zur Bewertung der Fähigkeiten von Fußgängersimulationsmodellen hinsichtlich der Darstellung von wichtigen mikroskopischen und makroskopischen Eigenschaften des menschlichen Bewegungsverhaltens basiert. Im Simulations-Framework wurde ein simulationsbasiertes Kalibrierungsverfahren angewendet, um die Parameterwerte für die verschiedenen Modellansätze anhand der definierten Evaluierungskriterien zu schätzen. Es hat sich gezeigt, dass durch die Kalibrierung die Anpassung an die beobachteten Daten in allen Modellen verbessert werden konnte. Der durch die Kalibrierung erzielbare Anpassungsgrad einzelner Modelle variiert jedoch. Die Modelle zeigen auch unterschiedliche Übertragbarkeit auf weitere Datensätze über jene die für die Kalibrierung verwendet wurden.

Die präsentierte Evaluierungsmethode kann leicht auf weitere Fußgängermodellierungsansätze angewendet werden, indem diese als separate, zusätzliche Module in das Simulations-Framework integriert werden. Für zukünftige Studien wird dies die Untersuchung der einzelnen Modelleigenschaften und den Vergleich neuartiger Modellierungsansätze mit bestehenden Modellen unterstützen.

Abstract

Microscopic simulation models are used in many applications for predicting pedestrian flows with high granularity. They have proven to be a valuable tool to support the design and evaluation of architectural plans, to estimate necessary capacities, to increase safety, efficiency and comfort in crowded areas, and to analyze scenarios for emergency evacuations. Although in the scientific literature a multitude of microscopic models is available, currently implemented simulators typically do not allow for easy and quick switching between models nor do they give insight in their functionality and implementation details. Moreover, there is still a lack of reliable human movement data, which however is a prerequisite for developing models that are able to represent realistic pedestrian behavior as well as for performing model calibration and validation. These shortcomings inhibit to evaluate the capabilities of different models. As a consequence, quantitative comparisons between various approaches are still rare.

This doctoral thesis develops for the first time a unified framework for the structured investigation on strengths and weaknesses of different microscopic pedestrian movement simulation models based on an empirical benchmark data set and on implemented models within a simulation framework.

The empirical baseline of this work is a highly accurate benchmark data set of 2674 human trajectories measured under real life conditions in a bidirectional corridor with a novel data collection approach using the low-cost sensor Microsoft Kinect. Our innovative human detection and tracking algorithm is based on agglomerative clustering of privacy-preserving depth data captured from an elevated view with multiple Kinects providing a Pedestrian Detection Rate of up to 94% and a Multiple Object Tracking Precision of 4 cm.

The proposed simulation framework is built on a scalable and flexible system architecture to easily integrate different simulation models. Hence it allows for consistent and efficient model calibration and validation. Three approaches of the Social Force model, a Cellular Automaton model, the Optimal Reciprocal Collision Avoidance model and two variants of the Optimal Steps Model were implemented in the simulation framework. As a first step towards model verification and validation, we have simulated selected test cases from the RiMEA-Guideline, which aspires to define a minimum standard for evacuation analysis. The potential of the simulation framework for easy and quick switching and combining models is demonstrated using two real world case studies: first, two versions of the Social Force approach and the Optimal Reciprocal Collision Avoidance model are applied within our framework for passenger flow simulation during boarding and

alighting of a train. Second, the ability of the proposed simulation framework to combine modeling approaches with varying granularity is demonstrated for high volume passenger flows in a subway station.

In the evaluation, the predictions of seven models implemented within the simulation framework are compared to the empirical benchmark data from the Kinect-based tracking and among each other. In order to establish a solid baseline for model comparison, every model is calibrated first on a subset of the benchmark data. Two methodologies for calibrating Social Force based models on the individual trajectory level are presented, i.e. model estimation by nonlinear least square methods and comparison of real and simulated trajectories. Furthermore, we introduce a structured evaluation environment based on measures to assess individual model capabilities of representing important microscopic and macroscopic characteristics of human movement behavior. A simulation-based calibration procedure is applied in our simulation framework to estimate the parameter values for the different modeling approaches with the defined set of evaluation measures. It was found that the calibration has improved the fit to the observed data set in all models. However, the grade to which individual models can be influenced by the calibration varies. The evaluation also revealed that the investigated models have diverse capabilities concerning transferability to an independent data set.

Our presented evaluation technique can easily be applied to a wider range of pedestrian modeling approaches by including them as separate, additional modules in the simulation framework. For future studies this will enhance the understanding of individual model characteristics and the comparison of novel modeling approaches to existing ones.

Contents

Kurzfassung	ix
Abstract	xi
Contents	xiii
1 Introduction	1
1.1 Aim of the Work	3
1.2 Methodological Approach	3
1.3 Structure of the Work	4
2 Obtaining Benchmarking Data on Pedestrian Movement	5
2.1 Kinect-based Human Detection and Tracking	9
2.2 Tracking Evaluation	16
2.3 Walking Experiments	19
2.4 Summary	20
3 Modeling Approaches for Pedestrian Simulation	23
3.1 Description of Pedestrian Modeling Approaches	23
3.2 Model Verification and Validation using RiMEA Test Cases	36
3.3 Summary	46
4 Pedestrian Simulation Framework	47
4.1 Concept of the Simulation Framework	49
4.2 Framework Modules	55
4.3 Case Studies	61
4.4 Summary	77
	xiii

5	Calibration Procedures for Social-Force Models	79
5.1	Model Parameter Estimation with Non-linear Regression	80
5.2	Simulation-based Model Parameter Estimation	86
5.3	Summary	90
6	Structured Evaluation of Pedestrian Modeling Approaches	91
6.1	Evaluation Measures for Model Comparison	91
6.2	Generalized Calibration Procedure	99
6.3	Evaluation and Comparison Results	100
6.4	Summary	106
7	Conclusion and Future Research	109
7.1	Discussion	109
7.2	Outlook	112
A	Detailed Calibration And Validation Results	113
A.1	Model Fit based on the Calibration Data Set	113
A.2	Model Fit based on the Validation Data Set	116
	Bibliography	119
	Abbreviations	131
	Curriculum Vitae	133

Introduction

With 66% of the world's population projected to live in urban areas by 2050, crowd management and modeling is becoming an urgent issue of global concern (United Nations (2014)). A better understanding of pedestrian movement can lead to an improved use of public spaces, to the appropriate dimensioning of urban infrastructure such as airports, stations and commercial centers.

Over the last years, crowd simulations have proven to be a valuable tool to predict pedestrian flows for the evaluation of architectural designs and operational plans in a variety of highly frequented urban places. The applications for which simulation tools can be useful cover the entire spectrum, from a detailed analysis of human interaction of a few individuals in a single room (Rudloff et al. (2011a)) to evacuating a concert with tens of thousands of spectators (Hamacher et al. (2011)). Furthermore, the conditions (e.g. the physical complexity of the environment or the number of individuals) in various application fields can differ greatly. Hence, there is a wide range of questions for which simulations should be able to provide answers.

In the scientific literature, simulation models are categorized according to their granularity of modeling the interaction between the pedestrians into *microscopic*, *macroscopic* or *mesoscopic* (see e.g. the classification for general traffic models in Cascetta (2009)).

Microscopic models define detailed behavior of individual humans and represent collective phenomena such as emergent behavior. The most common microscopic approaches noted in the scientific literature are Cellular Automata (Burstedde et al. (2001)) with grid-based motion decisions, discrete choice models (Antonini et al. (2006); Guo et al. (2010)) where pedestrians optimize their utility while moving, and Social Force models (Helbing and Molnár (1995)) which use a continuous representation of space.

Macroscopic models are often based on the analogy with fluid or gas dynamics and describe human movement dynamics as spatial distributions of densities using partial differential equations (Helbing (1992); Hoogendoorn and Bovy (2000); Henderson (1971)). Situated between the microscopic and the macroscopic methodology are mesoscopic models such as queuing models (Løvås (1994)).

On a different dimension Hoogendoorn and Bovy (2004) explained pedestrian behavior by providing a hierarchy of decisions. Accordingly, we differentiate between three levels of decision making in this work:

1. *Strategic Level*: on this level a person decides on general activity and trip purposes.
2. *Tactical Level*: on this level route-choice and intermediate goals are selected.
3. *Operational Level*: actual movement at each time instant towards the next goal – including collision avoidance based on interactions with other pedestrians and the environment.

Choices at higher levels serve as input for modeling pedestrian behavior at lower levels (e.g. goal setting steers the subsequent move) and, vice versa, choices at lower levels may influence higher levels (e.g. selecting a certain route instead of another might change the activity order). In the research of this thesis, this general modeling paradigm is pursued.

In order to develop a model that is able to represent realistic movement behavior one has to perform model calibration and validation of the results. Validation to examine the characteristics of a specific microscopic model is still sparse (e.g. Campanella et al. (2014), Zhang et al. (2014)). One reason for this is the lack of reliable human movement data, such as spatio-temporal motion trajectories. To take full advantage of the rich information included in human motion trajectories for the calibration and validation of microscopic models it is essential to measure all people in a given scene. The need for comprehensive and highly accurate human movement data from different movement settings is well documented in the scientific literature (Boltes and Seyfried (2013)). However, publicly available benchmarking data sets based on real-world observation are severely limited in terms of accuracy and number of observations. This motivates the need for improved automatic approaches to collect human movement data which have to fulfill the quality requirements for calibrating and validating microscopic models.

Although a multitude of different models is described in the literature, currently available simulation programs typically allow modeling pedestrian movement using only a single pre-specified simulation model. This is also reflected in the body of research, where often a specific simulator, movement data and set of evaluation criteria are applied. Quantitative comparisons between different models are still rare since currently available simulators do not allow for easily switching the model nor do they give insight in their functionality and implementation details (Wagoum et al. (2014)). This inhibits to evaluate the capabilities of different models. For objectively comparing different implementations of microscopic pedestrian simulation models, their performance has to be assessed quantitatively based on evaluation measures with respect to accuracy (e.g. reproducibility of pedestrian densities) and computational feasibility. As of now, several evaluation measures have been described and used in the literature. However, there is no consensus within the scientific community on which measures provide plausible results with respect to an objective evaluation. Consequently, a quality standard for validation of crowd simulation models is still missing (see also Rogsch et al. (2014)).

1.1 Aim of the Work

The goal of this doctoral thesis is to develop a framework that constitutes an optimal basis for structured investigation on strengths and weaknesses of microscopic pedestrian movement simulation models. The contributions of this thesis can be summarized as follows:

1. Generation of a benchmark data set by empirically collecting pedestrian movement data under real life conditions using an innovative people tracking approach with affordable sensor technologies.
2. Design and implementation of a novel simulation framework with a highly flexible system architecture to easily switch simulation models and allowing for consistent and efficient model calibration and validation.
3. Structured evaluation of microscopic pedestrian simulation models based on the empirical benchmark data set and the implemented models within the simulation framework.

1.2 Methodological Approach

Our methodological approach combines empirical benchmark data, calibration and validation strategies, and evaluation measures into a unified framework for evaluating microscopic pedestrian movement simulation models.

First, we present a methodology for collecting benchmark data on pedestrian movement and interaction behavior. Within this thesis, novel approaches for obtaining highly accurate people trajectories were developed using low cost sensors such as the Microsoft Kinect. We apply the human detection and tracking algorithms in highly frequented real-world scenarios. The resulting benchmarking data sets include a comprehensive set of individual trajectories representing evasive behavior with varying numbers and positions of human obstacles.

Furthermore, we design a simulation framework which provides a scalable and flexible system architecture for an easy integration of different simulation models. For flexibility, a modular architecture including three functional layers is used: the scenario layer allows to define the specifications for each simulation run, e.g. infrastructure layout, composition of the simulated crowd, etc. The application layer provides the possibility to configure simulation related parameters and to start a simulation run. In addition, it implements different strategies for estimating model parameters and evaluating a model's performance. The simulation layer includes a simulation core as central control component that communicates with several modules performing the actual simulation run. These individual modules contain all necessary functions for performing pedestrian simulations and can be switched or combined easily. The modular architecture of the simulation framework provides several important advantages since certain behavioral aspects can be separated from one another (e.g. route-choice on the tactical level or collision avoidance on the operational level) and thus form a logical encapsulation.

As part of the structured evaluation, we compare the predictions of specific pedestrian simulation models to observations of human movement and among each other. In total seven microscopic pedestrian simulation models were implemented as functional modules within the framework: the Social Force (SF) approaches from Helbing and Molnár (1995), Helbing and Johansson (2009) and Rudloff et al. (2011b), the Cellular Automaton (CA) model from Kirchner and Schadschneider (2002), the Optimal Reciprocal Collision Avoidance (ORCA) model from van den Berg et al. (2011) and two variations of the Optimal Steps Model (OSM) from Seitz and Köster (2012) and Seitz and Köster (2014), respectively. In order to establish a baseline for comparison, these models need to be calibrated with the pedestrian movement scenarios in our benchmark data set. Therefore, we present two strategies for calibrating and validating models that are based on the Social Force approach, i.e. model estimation by nonlinear least square methods and determination of model parameter values using simulation-based optimization, using individual human trajectories. We go further by introducing a structured environment including a set of methodologies for the investigation of strengths and weaknesses of various microscopic pedestrian movement simulation models. This involves the definition of additional evaluation measures based on microscopic and macroscopic characteristics (e.g. comparisons between simulated and observed trajectories, density, walking times, etc.) and a generalized procedure for model parameter estimation. A main criteria for assessing a model’s performance is the goodness-of-fit that indicates how well a model represents a certain evaluation measure from the benchmark data set.

1.3 Structure of the Work

This dissertation is structured as follows: Chapter 2 outlines and demonstrates the approach with multiple Microsoft Kinect sensors for obtaining highly accurate tracking data from an elevated view for pedestrian modeling. Chapter 3 describes state-of-the-art modeling approaches for pedestrian simulation used in this work and provides new insights into the processes of model verification and evaluation based on standardized test cases. Chapter 4 introduces a novel pedestrian simulation framework which allows to easily switch or combine various simulation models based on a highly flexible system architecture. We will describe the overall concept, architectural software design and implementation and demonstrate the potential of the simulation framework on two real world case studies. Chapter 5 presents general calibration and validation strategies for pedestrian models by means of Social Force based modeling approaches. Chapter 6 brings together the benchmark data, the pedestrian models, the calibration and validation strategies, and the evaluation measures within the simulation framework. The evaluation will compare the modeling approaches to the empirical benchmarking data and examine their particular differences related to model behavior. Chapter 7 concludes the main results and gives an outlook for further research.

Obtaining Benchmarking Data on Pedestrian Movement

An essential step in model development is the calibration with relevant datasets and the validation on different realistic scenarios. Model parameter estimation can be very complex due to large numbers of parameters or the limited availability of real-world datasets (see Rudloff et al. (2011b)). Some papers show that the calibrated models reproduce self organizing behavior such as lane formation (e.g. Helbing and Molnár (1997), Moussaïd et al. (2010)) and provide quantitative calibration results (Johansson et al. (2007)). However, research in microscopic pedestrian simulation mostly concentrates on model development, while calibration and validation processes are often neglected. One way to calibrate microscopic pedestrian simulation models is to use aggregated data such as density-flow relationships (according to so-called *Fundamental Diagrams*) as described in Davidich and Köster (2012). Developing and calibrating models for detailed human interaction behavior (e.g. collision avoidance) requires *highly accurate* data on pedestrian movements, i.e. spatio-temporal motion trajectories as well as the analysis of *all* people in a given scene.

In the pedestrian simulation community, such data is traditionally collected by manually annotating the positions of people in individual frames of recorded video data of highly frequented areas (Antonini et al. (2006), Berrou et al. (2007)). Sometimes additional attributes such as age or gender are assigned to people during the annotation process. Manual annotation, however, is tedious and time-consuming, in particular for dense scenes with many pedestrians. This limits the amount of data that can be analyzed. Semi-automated video annotation approaches can facilitate the generation of motion data by providing automatically computed position predictions which support manual annotation (Plaue et al. (2011), Johansson and Helbing (2010)). Semi-automated video annotation can provide significant speedup compared to purely manual annotation, but is still time-consuming. In some experimental setups for pedestrian simulation modeling, participants of the experiments are equipped with distinctive wear such as colored hats

for better identification. Naturally, such distinctive wear makes automated extraction of trajectories a relatively easy task. The free software *PeTrack* presented in Boltes et al. (2010) has been applied on video recordings of a bottleneck experiment. The automatic tracking approaches of Hoogendoorn et al. (2003) and Hoogendoorn and Daamen (2005) collected trajectory data in a narrow bottleneck and a four-directional crossing flow experiment. Controlled experiments allow the setting of environmental conditions that are hard to observe in real world circumstances as in Daamen and Hoogendoorn (2012), where emergency settings were reenacted including acoustic and visual signals. However, such setups only allow for a limited sample size and include a significant bias in the data since participants are usually aware of being observed.

Large scale and real-world data on human motion can be obtained from video only when applying tools for automatic vision-based people detection and tracking. Vision based tracking has seen considerable progress in recent years, with current systems able to track people through long and challenging sequences (Pellegrini et al. (2009)). There exist many approaches for multi-camera people tracking assuming overlapping fields of view, e.g. Fleuret et al. (2008), Eshel and Moses (2010), Sternig et al. (2011). Approaches dealing with camera networks with non-overlapping fields of view include Javed et al. (2007), Loy et al. (2009) and Pflugfelder and Bischof (2010). The advanced computer vision methods are mostly not concerned with highly accurate tracking (in the sense of giving a position estimate within centimeters of the actual position), but are more concerned with working under difficult conditions (occlusions, clutter, lighting, ...), which limits their reliability and makes them less appropriate for measurement tasks. The computer vision community provides publicly available benchmark sequence datasets with manually or semi-automatically annotated data for testing common surveillance tasks, such as pedestrian detection, tracking and behavior analysis, e.g. PETS (PETS (2009)) and VIRAT (Oh et al. (2011)). Many of these sequences were captured with people *acting* behavior according to a script, often also due to legal and privacy issues. The 3DPeS dataset of Baltieri et al. (2011) provides a benchmark dataset primarily for people re-identification, where subjects were notified of the presence of cameras, but not coached or instructed in any way. Benchmark datasets where subjects were not notified of the presence of cameras are provided in the BIWI walking dataset of ETH Zurich (Pellegrini et al. (2009)) and the 'crowds-by-example' dataset of University of Cyprus Computer Graphics Lab (2011). These datasets were generated by manual or semi-automated annotation for the sake of ground truth, and were used, for example, to demonstrate novel people tracking algorithms improved with Social Force Models (Pellegrini et al. (2009)) or algorithms for automatically inferring groups with Social Force Models (Sochman and Hogg (2011)). Notably, these algorithms are published by renowned computer vision labs and critically rely on accurate trajectory data of every person in the scene, and are still *evaluated only on the manually or semi-automatically annotated ground truth trajectory data*.

Mutual occlusions of people are one of the major challenges for automatic multiple people tracking from oblique camera views, and they can be minimized or avoided when capturing the scenes from a top-down view. The Edinburgh Informatics Forum Pedestrian

Database (Bob Fisher (2010)) provides a comprehensive set of trajectories computed in video from a fixed overhead camera 23 meters from the floor. This elevated height covers a large area, and the authors in (Bob Fisher (2010)) note that there are usually only a few individuals in each video frame (1 person in 46 % of the frames, four or less persons in 93 % of the frames), and that scenes with many people (events) cause difficulties in the tracker. The dataset has been used to demonstrate surveillance algorithms, in particular to detect unusual behavior, for example in Calderara et al. (2011).

In this work we propose an approach for calibrating microscopic pedestrian simulation models with highly accurate and comprehensive trajectory data on individual pedestrian movement using Microsoft Kinects mounted in top-down positions. The Kinect is an inexpensive motion sensing input device which was originally developed for the Xbox 360 video game console and delivers RGB camera images and a 3D depth map (Microsoft Corp. (2012a)). It was originally designed to accurately detect three dimensional positions of body joints (Shotton et al. (2011)) and to estimate human pose (Girshick et al. (2011)). Figure 2.1 illustrates the *skeletal tracking* which is the key component of the video game user interface. With its built-in functionality, the Kinect can detect up to six people (two of them using the skeletal tracking) provided that all persons face the sensor in frontal view with their upper bodies visible. Since its market introduction in 2010, the Kinect has also been used in a broad variety of other research fields: Noonan et al. (2011) showed the use of the Kinect for tracking body motions in clinical scanning procedures. Animation of the hand avatar in a virtual reality setting by combining the Kinect with wearable haptic devices was developed in Frati and Prattichizzo (2011). The Kinect was used in Izadi et al. (2011) to create detailed three dimensional reconstructions of an indoor scene. Weiss et al. (2011) presented a method for human shape reconstruction using three dimensional and RGB data provided by the Kinect. Choi et al. (2013) demonstrate their method for multiple people tracking from a moving camera using Kinect datasets.

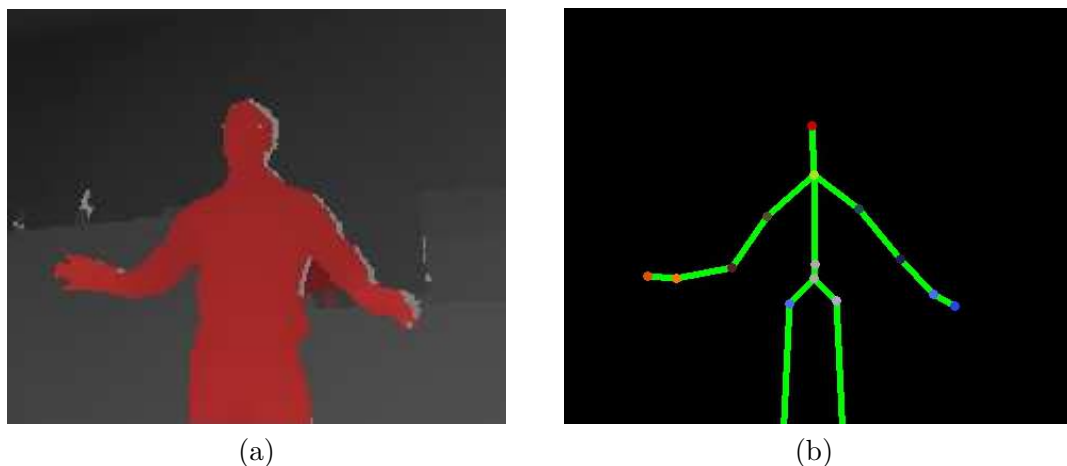


Figure 2.1: Microsoft Kinect provides the depth data stream (a), with the detected person in red and different gray levels encoding the depth information, and skeletal tracking (b).

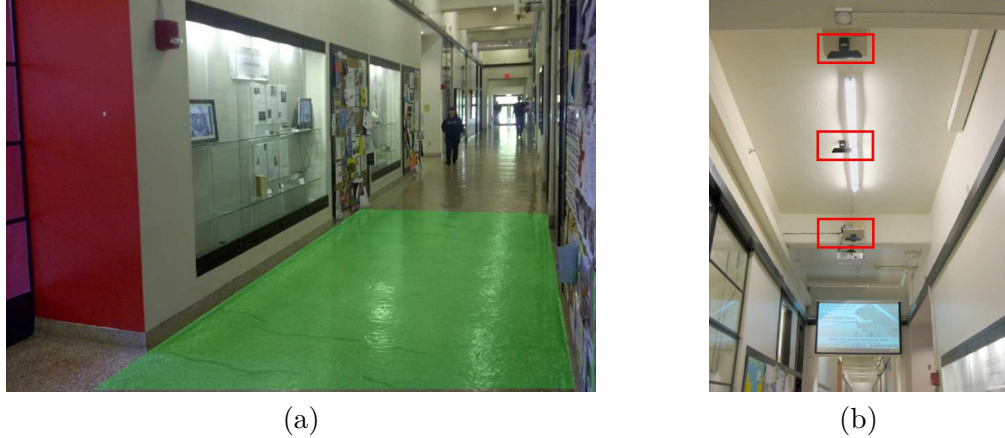


Figure 2.2: MIT's Infinite Corridor with (a) the observed area (green) and (b) the Kinect setting on the ceiling.

To the best of our knowledge, the Microsoft Kinect has not yet been used to obtain data for modeling pedestrian motion behavior. The built-in skeletal tracking cannot be directly used for accurately measuring pedestrian movement.

In this work we provide a contribution for pedestrian researchers by presenting an alternative approach using multiple Microsoft Kinects for obtaining highly accurate tracking data from an elevated view for pedestrian modeling (Seer et al. (2014a))¹. The approach processes only information from the 3D depth sensor, thus avoiding any legal and privacy issues arising when observing people in real-world scenarios with imaging in the visual spectrum. We demonstrate the high accuracy of the trajectories in a real world setup and show how such an automatically obtained set of more than 2600 trajectories is used to calibrate and compare microscopic pedestrian simulation models. The overall added value with respect to previous approaches is the feasibility to automatically obtain large and accurate sets of human movement data at low cost paving the way for many pedestrian researchers to better calibrate and validate their simulation models.

We combined three Kinect sensors and collected a large dataset on pedestrian movement inside the Massachusetts Institute of Technology (MIT)'s Infinite Corridor, the longest hallway that serves as the most direct indoor route between the east and west ends of the campus and is highly frequented by students and visitors. Figure 2.2a shows the area identified for the data collection in this work, and Figure 2.2b shows the Kinect sensors mounted at the ceiling. In our setting, a single Kinect sensor is capable of covering an area of roughly $2\text{ m} \times 2\text{ m}$. Since we have suspended three Kinect sensors from the ceiling, human movement behavior in an overall scanning area of around 12 m^2 could be measured. In order to observe various pedestrian behaviors we performed different walking experiments in this environment.

¹The work in this chapter was published by S. Seer, N. Brändle and C. Ratti, "Kinects and Human Kinetics: A New Approach for Studying Pedestrian Behavior", In: *Transportation Research Part C: Emerging Technologies*, DOI: 10.1016/j.trc.2014.08.012, pp. 212-228, 2014.

2.1 Kinect-based Human Detection and Tracking

The Kinect provides a sequence of standard RGB color frames and a 3-dimensional depth image for each frame. The depth image of a scene indicates the distance of each picture element of that particular scene from the Kinect. Depth images and RGB color images are both accessible with the *Kinect for Windows SDK* by Microsoft Corp. (2012b). Figure 2.3 illustrates a snapshot of the depth image, the RGB image and a combination of depth and RGB from three Kinects mounted at a height of 4.5 meters and a top view position in the MIT’s Infinite Corridor. With this setup a section of 6 meters of the corridor can be captured. Note that the glass case introduces a significant amount of artifacts due to specular reflections. In order to meet privacy concerns – most of the observed persons are not aware of any data collection experiment – our approach does not process RGB information from the visible spectrum.

In order to compute pedestrian trajectories from depth image sequences of multiple Kinects, we 1) map depth information from individual Kinect sequences into a common world coordinate system, 2) group depth information from a single Kinect in the world coordinate system into individual pedestrians and 3) track the pedestrians to obtain trajectories throughout the sensing areas of multiple Kinect sensors. These three steps are described in the following subsections.

2.1.1 Obtaining World Coordinates

A Kinect sensor S_k from a set of K devices generates a time series of 640×480 depth pixel images. Each depth image encodes a set of valid three-dimensional points $\mathbf{x}_{c_i} = [x_{c_i} \ y_{c_i} \ z_{c_i}]^T$, with $i \leq 640 \times 480$, in the local Kinect 3D camera coordinate system, computed with the value of the focal length f provided by Microsoft Corp. (2012b). The physical constraints of the Kinect 3D-measurement setup limit the range of z_{c_i} within which reliable depth data can be computed to a maximum distance of 4 meters. Objects which are located more than 4 meters away from the sensor can not be captured.

A human trajectory \mathcal{T} is denoted as a sequence of N four-dimensional vectors

$$\mathcal{T} = \{[t_i \ x_{w_i} \ y_{w_i} \ z_{w_i}]^T\}_{i=1 \dots N}, \quad (2.1)$$

where the vectors are composed of a timestamp t_i and a 3D position $\mathbf{x}_{w_i} = [x_{w_i} \ y_{w_i} \ z_{w_i}]^T$ in a common world coordinate system: For a trajectory to represent people walking throughout the sensing areas of multiple Kinect sensors, the points of the local 3D coordinate systems of the mounted Kinect sensors must first be mapped to the world coordinate system.

The actual point mapping between the coordinate system of sensor S_k and the world coordinate system is represented by a rigid transformation, composed of a translation vector \mathbf{t}_k between the two origins of the coordinate systems and a 3×3 rotation matrix \mathbf{R}_k such that

$$\mathbf{x}_{w_i} = \mathbf{R}_k \mathbf{x}_{c_i} + \mathbf{t}_k. \quad (2.2)$$



Figure 2.3: Kinect sensor field of view; raw depth data stream (left), RGB stream (middle) and both data streams in an overlay (right).

Note that we do not model nonlinear lens distortion. As elaborated in Konolige and Mihelich (2012), the Kinect lenses are already very good compared to, for example, typical webcams, with a reprojection error (deviation of the camera from the ideal pinhole model) of 0.34 pixel for the IR camera. Konolige and Mihelich (2012) show that modeling lens correction could reduce the reprojection error by factor of 3. Lens correction is useful for RGB images with subpixel accuracy applications. Kinect IR depth images, however, are already smoothed over a neighborhood of pixels by the correlation window, hence correcting a third of a pixel would not significantly change the depth result.

The three parameter values for translation \mathbf{t}_k of sensor S_k and its three rotation angles in \mathbf{R}_k are determined by a set of M point matches $\langle \mathbf{x}_{w_i}, \mathbf{x}_{c_i} \rangle$, $i \in M$ and subsequently minimizing the error

$$E = \sum_{i=1}^M \|\mathbf{x}_{w_i} - \mathbf{R}_k \mathbf{x}_{c_i} - \mathbf{t}_k\|^2 \quad (2.3)$$

by solving an overdetermined equation system as described in Forsyth and Ponce (2002).

We determine the M point matches $\langle \mathbf{x}_{w_i}, \mathbf{x}_{c_i} \rangle$ in world coordinates \mathbf{x}_{w_i} manually from the depth images. Since only depth information and no visual information is available for the sensed area, sensor calibration must be based on pre-determined calibration objects with well-defined depth discontinuities. Our sensor calibration setup is composed of a rectangular piece of cardboard placed on a tripod with a height of 1587 mm from the ground. We marked multiple reference points on the ground assuring that they are equally distributed within the field of view. One by one, the tripod with the mounted cardboard on top was placed perpendicular to a single reference point and the depth data was recorded for a couple of seconds. The reference points in world coordinates \mathbf{x}_{w_i} are determined as the center of gravity of the extracted cardboard corners in the depth images. The raw depth data including the reference points and the results of the calibration for all sensors are shown in Figure 2.4. Table 2.1 shows that the Root-Mean-Square Error (RMSE) between the reference points in the world coordinates and the reference points in camera coordinates transformed with (2.2) lies within the range of a few centimeters.

	Sensor S_1	Sensor S_2	Sensor S_3
RMSE	64 mm	67 mm	19 mm

Table 2.1: Accuracy of calibration computed on reference points.

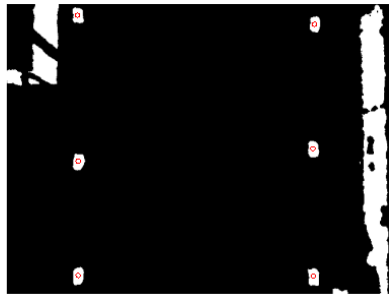
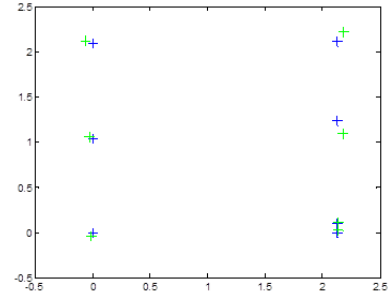
2.1.2 Detection Algorithm

Let \mathcal{D} denote the set of points \mathbf{x}_{w_i} obtained by applying the rigid transform (2.2) to the 3D camera coordinates from the Kinect depth images. The objective of human detection is to extract from \mathcal{D} connected sets of points belonging to a person and to represent the person with a point \mathbf{x}_{p_i} , that is the center of the head. Human tracking associates detections of individuals over time. Human detection is composed of the following steps:

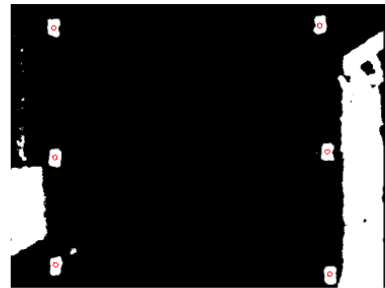
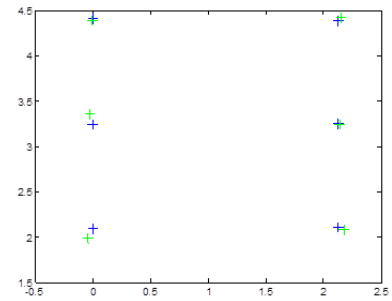
1. **Data Reduction by Background Subtraction.** Identifying a set of points which do not change or only change slowly over time – the background – supports the segmentation of walking persons from other objects and reduces the number of depth points to be processed. This can be achieved by classic background subtraction techniques from the domain of video analysis, e.g. the adaptive background modeling with Gaussian Mixture Models described in Stauffer and Grimson (2000). In our particular case of the Infinite Corridor, the background model is handcrafted, since the locations of background objects such as walls are well-known in advance.
2. **Data Reduction by Cutoff.** The cutoff step first removes all 3D points which remain after background subtraction with height z_{w_i} larger than a tall person’s height, e.g. 2.1 meters for adults, and all 3D points with height z_{w_i} smaller than a typical upper body region, e.g. 1.5 meters. The second cutoff value determines the minimal height of detectable persons, and is necessary to exclude noisy measurements of objects near the floor. Applying the cutoff values to z_{w_i} results in a subset \mathcal{D}' .



Sensor S_1



Sensor S_2



Sensor S_3

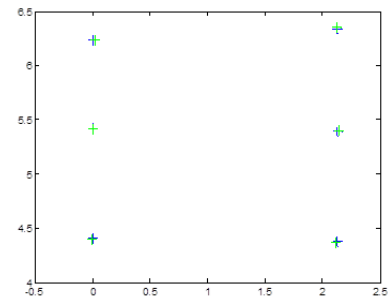


Figure 2.4: Left column - Raw data from sensor including reference points (red circles); Right column - sensor calibration results with measured reference (blue) and estimated (green) points.

3. **Hierarchical Clustering on the Reduced Set.** In order to group the points \mathcal{D}' into natural clusters corresponding to individual persons, we first build a cluster tree by agglomerative clustering with the complete-linkage algorithm (Duda et al. (2001)). For computational reasons we randomly select a subset \mathcal{D}'' of R points from \mathcal{D}' for clustering, where typically $R = 500$. The complete-linkage algorithm uses the following distance $d(\mathcal{D}_i'', \mathcal{D}_j'')$ to measure the dissimilarity between subsets of \mathcal{D}'' :

$$d(\mathcal{D}_i'', \mathcal{D}_j'') = \max_{\substack{\mathbf{x} \in \mathcal{D}_i'' \\ \mathbf{x}' \in \mathcal{D}_j''}} \|\mathbf{x} - \mathbf{x}'\|, \quad (2.4)$$

with $\|\cdot\|$ as the Euclidean distance. Using metric (2.4) avoids elongated clusters and is advantageous when the true clusters are compact and roughly equal in size (Duda et al. (2001)). All leaves at or below a node with a height less than a threshold are grouped into a cluster, where the threshold is based on a typical human shoulder width, e.g. 0.6 meters.

4. **Grouping of \mathcal{D}' and Cleanup.** All available observation points of \mathcal{D}' are assigned to a cluster, given that they are sufficiently close to the cluster center. Otherwise they are removed. Small clusters which originate from noise or people on the border of the field of view are removed.
5. **Identifying a Cluster Representative.** For every cluster \mathcal{D}_i'' , the point \mathbf{x}_{p_i} representing the pedestrian location of a trajectory (2.1) is selected as the point with the 95th percentile of the height z_{w_i} in \mathcal{D}_i'' , defined as the person's height.

This process provides robust people detections of all individuals in a single depth image.

2.1.3 Tracking over Multiple Sensor Views

In order to establish correspondences between consecutive detections and obtain trajectories \mathcal{T} as defined in (2.1), we perform global tracking of the people detections \mathbf{x}_{w_i} in the world coordinate system by a simple nearest neighbor matching based on position predictions linearly extrapolating individuals' positions of the previous n detections. We search for the nearest detection in the neighborhood within a spatial and temporal threshold.

While other applications use more complex approaches for object tracking (see Berclaz et al. (2011) for an overview), we take advantage of the high rate of 30 frames per second provided by the Kinect. We experimentally determined $n = 5$, taking into account a sufficient number of observations for obtaining a reliable estimate of the predictions. Figure 2.5 illustrates the tracking results of a short sequence as red lines, superimposed to raw depth data of a Kinect sensor from a single frame.

The algorithm effectively tracks pedestrian heads, and the question might arise whether the head of a pedestrian is the most stable object to track. Increased variability of vertical head translation and pitch rotation of the head with respect to pitch trunk

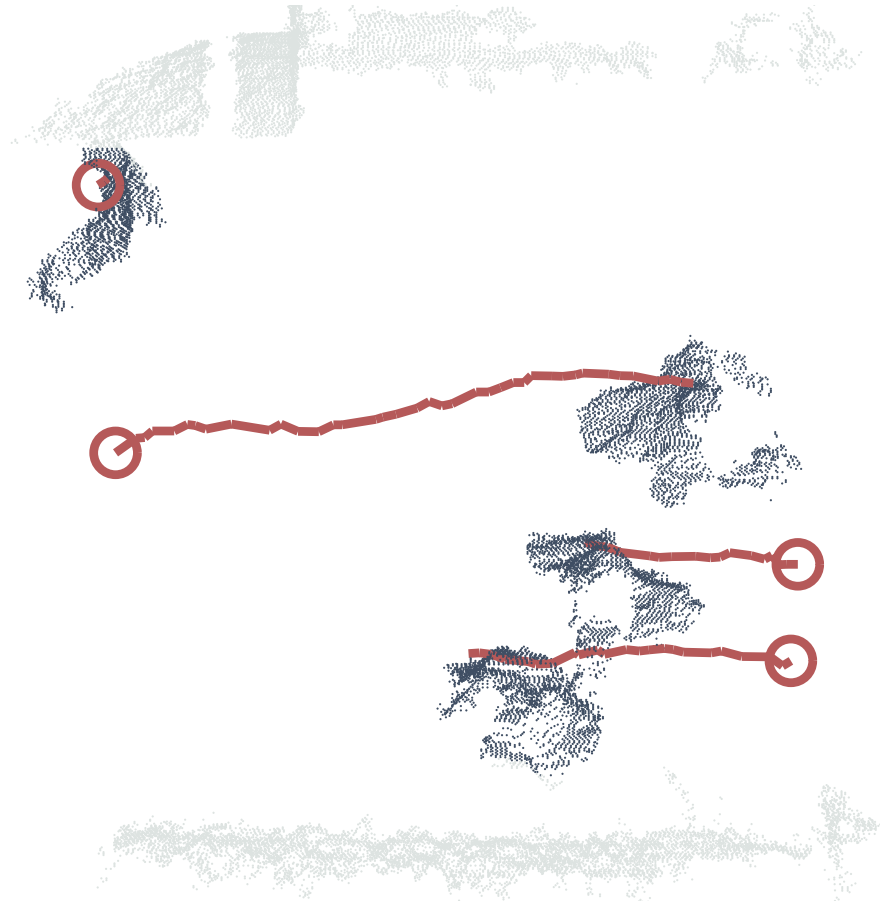


Figure 2.5: Kinect depth raw data in 3D from a single frame (walls are light gray and detected objects are dark gray) with automatically obtained trajectories (red circles denote the starting point of a trajectory and red lines the individual paths until the current frame).

rotation was observed only for fast speeds (> 1.4 m/s) during experimental setups in Hirasaki et al. (1999). Additional variation might occur due to yaw rotation of the head for persons looking around while walking or standing in the observed area. Hence, shoulders as viewed from above might be a bit more stable when compared to head variations, in particular for fast speeds. Despite this, we prefer detection of head center points in the 3D data from the Kinect as the more straightforward and less error-prone approach, supported by the evaluation results of Section 2.2.

Having the Kinect sensors in a slightly overlapping setting avoids unobserved regions without any information on the location of pedestrians, and consequently enables more robust tracking. Figure 2.6 illustrates the results of our automatic tracking approach in a scene with three persons (current position denoted by dashed circles) based on detections from three slightly overlapping views. When using overlapping sensors a single person

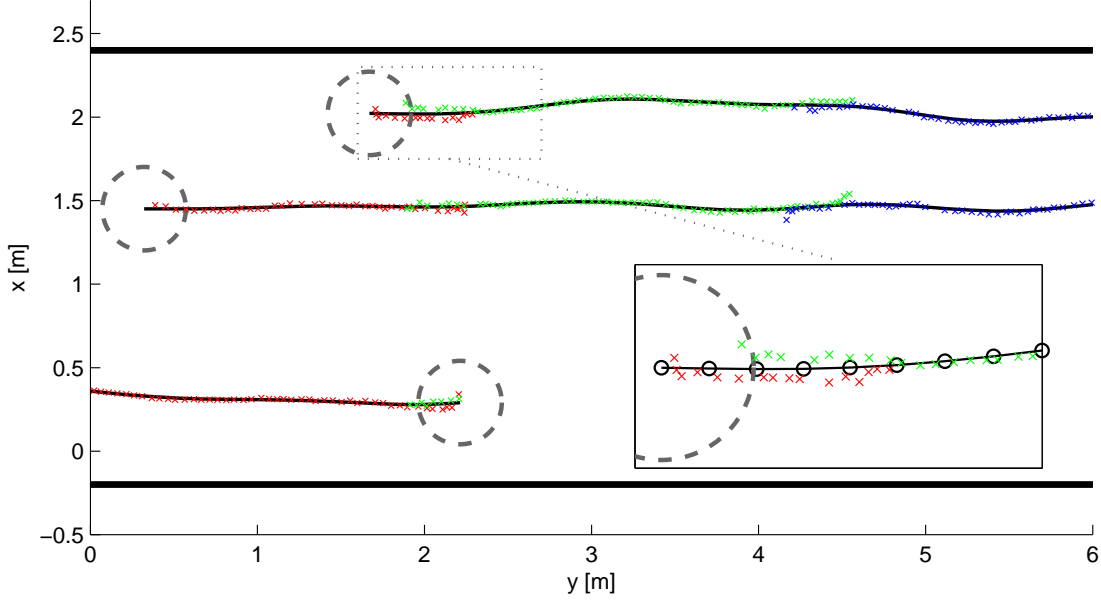


Figure 2.6: Automatic tracking of three persons (current position denoted by dashed circles) based on detections from three slightly overlapping views (crossings in red, green and blue) with the resulting smoothed trajectories (black curve with circles, within the magnified box).

potentially creates more than one detection in world coordinate space. This leads to artifacts within the resulting trajectories in form of small fluctuations (see magnification in Figure 2.6). We therefore resample each individual trajectory \mathcal{T} as defined in (2.1) comprising N detections to a trajectory \mathcal{T}' with M vectors defined as

$$\mathcal{T}' = \{[t'_i \ x'_{w_i} \ y'_{w_i}]^T\}_{i=1 \dots M}, \quad (2.5)$$

where $t'_i = t_1, t_1 + \Delta t', t_1 + 2\Delta t', \dots, t_N$ with a sample rate $\Delta t' = 0.1$ seconds. Note that since the approaches for pedestrian modeling and calibration used in this work make use of trajectories in 2-dimensional space only, we can omit z'_{w_i} in (2.5). The corresponding x'_{w_i} and y'_{w_i} at the regular time intervals t'_i are obtained by cubic spline approximation according to De Boor (2001) using a smoothing parameter $p = 0.98$, which smoothes out the mentioned fluctuations and other small local variations along the trajectory (see black curve within the magnified box in Figure 2.6).

2.2 Tracking Evaluation

Real data for pedestrian simulation calibration is often confined to trajectories which have been manually extracted from video data sets. The reason is that the required accuracy of the trajectories is very high, and often only manually extracted trajectories can fulfill such accuracy requirements. It is thus necessary to compare the output of the Kinect pedestrian tracking described above with the "gold standard" of manually generated trajectories in order to have an idea how suitable automatic collection of really large data sets are.

A human observer annotated the locations of all individuals in single frames using the raw depth sensor data from a single Kinect sensor. While the Kinect's depth data does not allow for identifying persons, the body shape of individuals is still recognizable. Our evaluation data is composed of two trajectory sets: the first data set comprises 15578 frames (≈ 590 seconds) with pedestrian flows of low to medium density, i.e. up to 0.5 persons/m^2 , and a total number of 128 persons. The second sequence includes 251 frames (≈ 12 seconds) with a total number of 21 persons and comparably higher densities of up to 1 person/m^2 . Note that the stated densities are averaged over the covered area. Thus, the data do contain local densities well above 1 person/m^2 , for instance in case that several pedestrians stand or walk closer together although a larger area is available. Figure 2.7 illustrates a single frame from the second dataset.



Figure 2.7: Kinect depth raw data in 3D (gray) with manually annotated head positions of individuals (red circles).

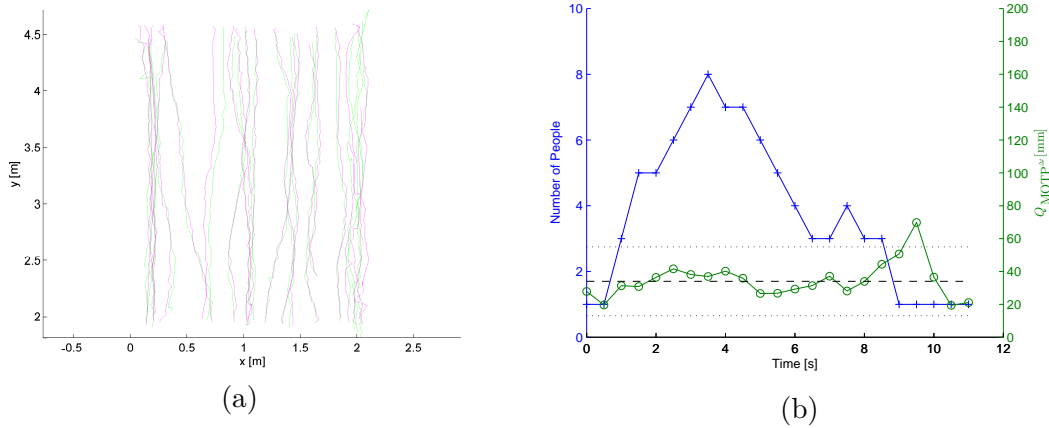


Figure 2.8: Tracking performance evaluation including 21 persons with up to 1 person/ m^2 based on (a) ground truth (green) and automatic trajectories (magenta) and (b) the temporal aspects of the Multiple Object Tracking Precision (MOTP) with average (dashed line) and standard deviation (dotted line).

In the first step of the evaluation, every automatically computed trajectory \mathcal{T} is assigned to a ground truth trajectory \mathcal{T}^G by minimizing a trajectory distance metric. Quantifying the pairwise trajectory dissimilarity in a distance metric is not trivial due to the usually different number of points. Here we used the discrete Fréchet distance (Eiter and Mannila (1994)). Following an informal interpretation, the Fréchet distance between two trajectories is the minimum length of a leash that allows a dog and its owner to walk along their respective trajectories, from one end to the other, without backtracking. Taking into account the location and ordering of points along the trajectories, the Fréchet distance is well-suited for the comparison of trajectories and is less sensitive to outlier points than alternatives for arbitrary point sets such as the Hausdorff distance.

As a result of the trajectory assignment we derive a set of P matching trajectory pairs for a time stamp t . Any remaining automatically computed trajectories which could not be matched are considered as false positives. Similarly, any remaining ground truth trajectories which could not be matched are considered as misses. Figure 2.8a shows the results based on trajectories from the second sequence. Our dataset produced zero false positives and one miss. It was seen in the data that this missed person was smaller than the defined cutoff value of 1.5 meters. In order to quantify the position error for all correctly tracked objects over all frames, we use the Multiple Object Tracking Precision (MOTP) as described in Bernardin and Stiefelhagen (2008), which is defined as

$$Q_{\text{MOTP}} = \frac{\sum_{i,t} \|\mathbf{x}_{i,t} - \mathbf{x}_{i,t}^G\|}{\sum_t c_t}, \quad (2.6)$$

where c_t is the number of matches found at time t . For each match i , the Euclidean distance between the automatically computed trajectory point $\mathbf{x}_{i,t}$ and the ground truth trajectory point $\mathbf{x}_{i,t}^G$ at time t is computed.

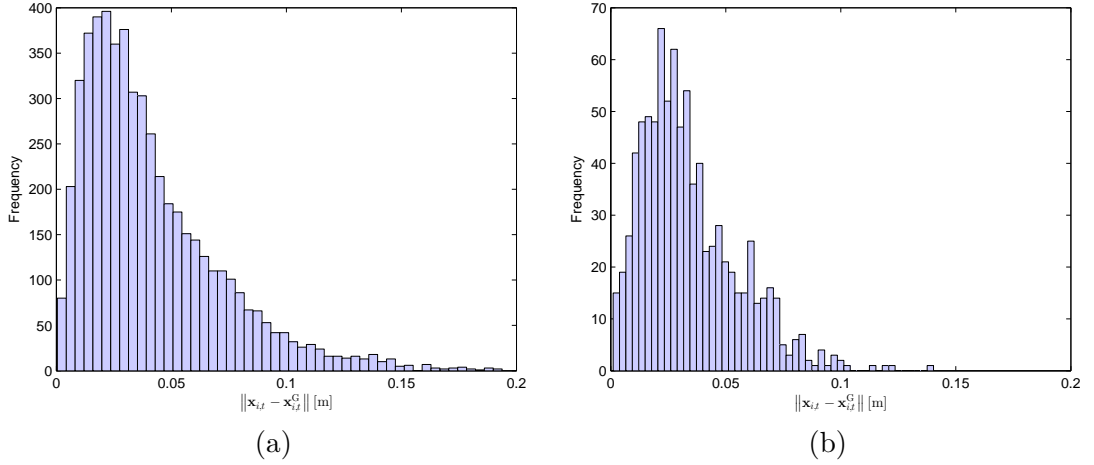


Figure 2.9: Tracking evaluation results, showing the distribution of the Euclidean distance between the corresponding automatic trajectory point $\mathbf{x}_{i,t}$ and the ground truth trajectory point $\mathbf{x}_{i,t}^G$ for (a) Sequence 1 and (b) Sequence 2.

The evaluation results for our detection and tracking approach are shown in Table 2.2 and reveal that the localization errors in terms of MOTP are only within a few centimeters for both sequences. Figure 2.8b illustrates the evolvement of MOTP over short time intervals based on the second sequence: for each time interval $\Delta t = 0.5$ seconds, the tracking precision $Q_{\text{MOTP}\Delta t}$ is computed equivalently to (2.6). This analysis reveals that tracking accuracy is stable independent of the number of people. Figure 2.9 illustrates the distribution of the Euclidean distances $\|\mathbf{x}_{i,t} - \mathbf{x}_{i,t}^G\|$ according to (2.6) for all matches i between corresponding automatic and ground truth trajectory points for both sequences. Compared to other scientific work such as Heath and Guibas (2008), where MOTP was in the range between 16 and 19 cm our approach shows significantly higher accuracy.

The Pedestrian Detection Rate (PDR) measures the rate at which tracked pedestrians are matched to the ground truth. The value of PDR varies between 0 and 1. While 0 means poor pedestrian detection, 1 means that all ground truth pedestrians are matched. The metric is given by

$$Q_{\text{PDR}} = \frac{\text{TP}}{\text{TP} + \text{FN}}, \quad (2.7)$$

where the number of matched ground truth pedestrians is denoted by true positives TP. False negatives FN state the number of missing detections. Table 2.2 provides the evaluation results for our detection and tracking approach. Based on the PDR, our approach performs well on both sequences, with detection rates above 94%.

For Sequence 1 the PDR's for 115 out of 127 tracked persons are higher than 90% whereas the remaining 12 persons are lying in the range between 26.5 to 88.6%. For Sequence 2 the PDR's for 19 out of 21 persons are above 90% with the remaining 2 persons being in the range between 36.2 and 46.3%.

	$Q_{\text{PDR}}[\%]$	$Q_{\text{MOTP}}[mm]$
Sequence 1	96.20 (12.39)	41.3 (30.2)
Sequence 2	93.86 (17.64)	34.0 (21.0)

Table 2.2: Tracking evaluation results, showing Pedestrian Detection Rate (PDR) and Multiple Object Tracking Precision (MOTP), and its standard deviation in brackets.

2.3 Walking Experiments

The people trajectories automatically obtained by the Kinect people detection and tracking described above have a positioning error of only a few centimeters with respect to manual annotation (see Table 2.2). Thus, a set of mounted and calibrated Kinects can quickly and easily produce large datasets of accurate empirical observations. Such movement datasets covering a variety of walking behavior are exactly what microscopic pedestrian models must rely on in order to be realistic.

We performed a variety of walking experiments at the MIT’s Infinite Corridor described in the beginning of Chapter 2 while capturing depth image sequences of the three Kinect sensors. Applying the people tracking algorithm on the collected Kinect raw depth data produced a comprehensive amount of robust trajectories providing the necessary information for calibrating different types of microscopic pedestrian simulation models. The walking experiments were performed under real world conditions, meaning that the individuals traversing MIT’s Infinite Corridor had no information about being observed.

In the first walking experiment, a person standing in the center of the observed area served as an obstacle for passing people. The 685 trajectories of this setting were recorded during a period of approximately 28 minutes (see Figure 2.10a). The second walking experiment includes “normal” walking behavior without any external influence for a time span of around one hour. The 1989 trajectories computed with our Kinect approach are illustrated in Figure 2.10b. The red and blue trajectories in Figure 2.10a and b represent the two walking lanes in opposite directions which people form most of the time. From thorough investigation of both datasets we can confirm that various conditions are covered, including (but not exclusively) walking at different densities, walking-stopping-walking, abrupt changes of direction and random movement.

Figures 2.11a and b show the walking speed histograms computed from the trajectories of the two calibration data sets (the velocity of the person acting as an obstacle in experiment 1 is filtered out). Fitted parameters of a Gaussian function to the data set result in a mean speed of 1.33 m/s and a standard deviation of 0.26 m/s. Experiment 2 shows similar results for the walking speed distribution with a mean speed of 1.30 m/s and a standard deviation of 0.33 m/s. Our results are well in line with findings in the scientific literature. For instance, the literature review in Daamen and Hoogendoorn (2006) revealed that the walking speed of an individual appears to follow a normal distribution with an estimated mean of 1.34 m/s and a standard deviation of 0.37 m/s.

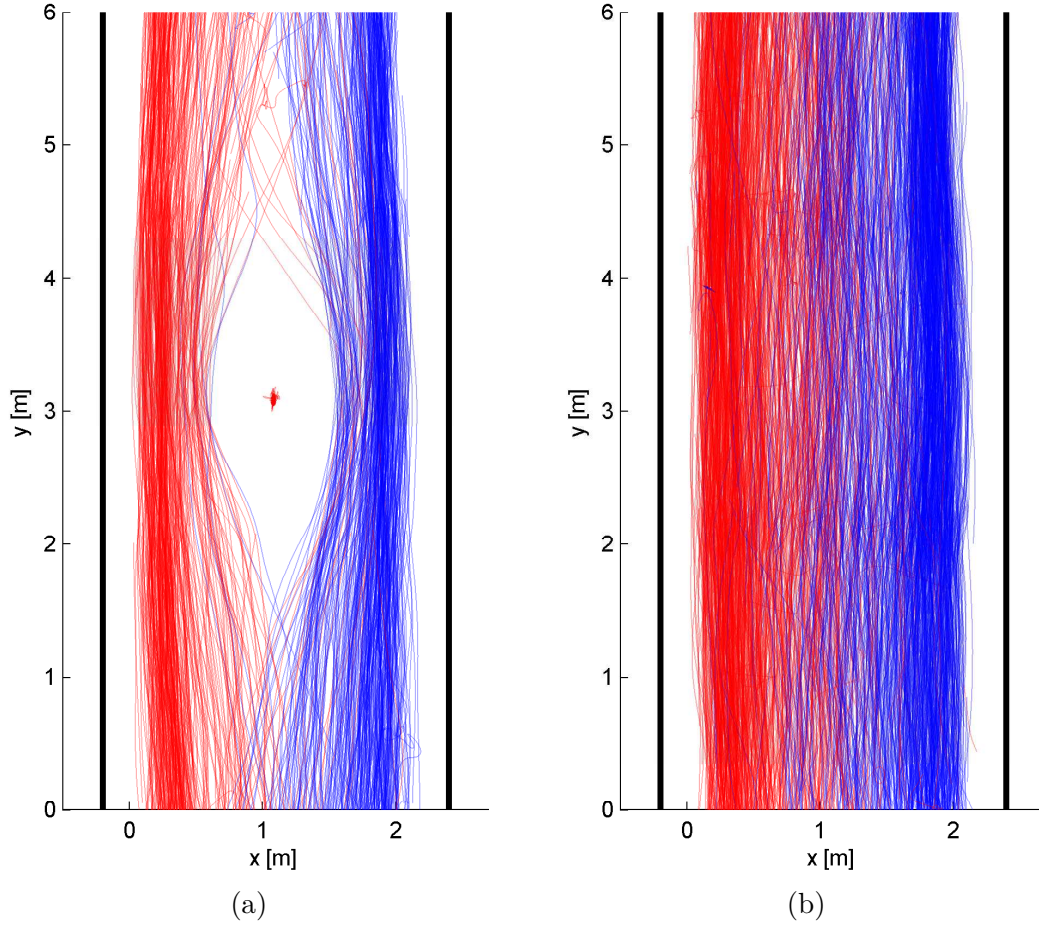
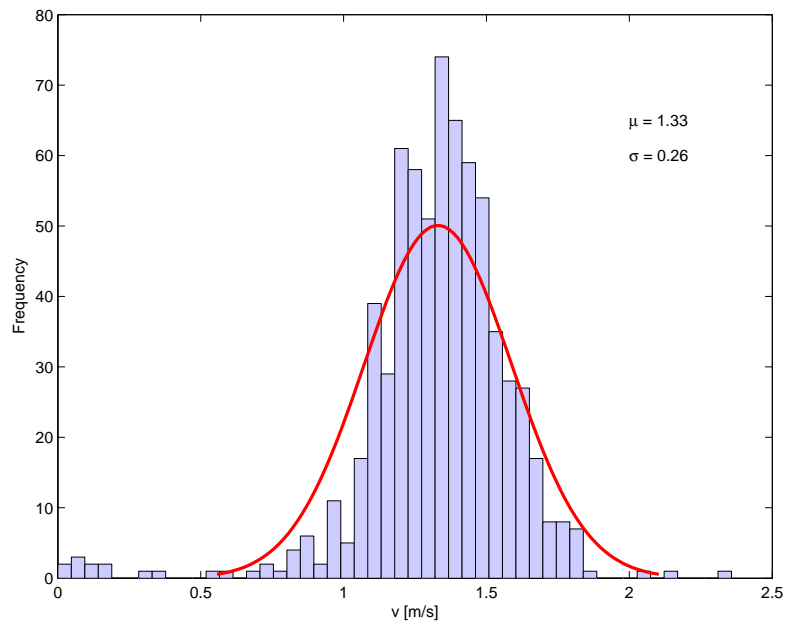


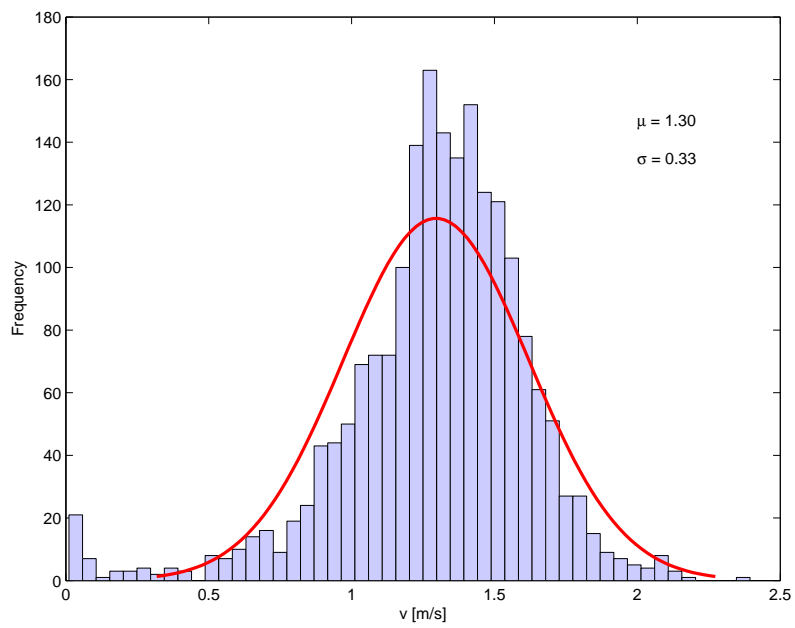
Figure 2.10: Trajectories of the benchmarking data set automatically retrieved from (a) experiment 1 and (b) experiment 2 (walking directions are encoded in red and blue).

2.4 Summary

In this chapter we have presented an algorithm for automatically collecting people trajectories using the Microsoft Kinect. The performed evaluation showed that our algorithm is capable of tracking individuals with high precision, that is a Pedestrian Detection Rate of up to 94% and a Multiple Object Tracking Precision of 4 cm. By applying our tracking approach in two walking experiments under real world conditions, we have obtained a benchmarking data set consisting of 2674 trajectories. In the rest of the dissertation this benchmarking dataset is used for calibration and validation of different microscopic pedestrian simulation approaches which will be described in Chapter 3.



(a)



(b)

Figure 2.11: Walking speed distribution from (a) experiment 1 and (b) experiment 2.

Modeling Approaches for Pedestrian Simulation

The objective of this thesis is to evaluate pedestrian simulation models with respect to the observed pedestrian movement from our benchmarking data set presented in Chapter 2 in order to reveal the individual capabilities and differences between the modeling approaches. This chapter describes the selected models which are part of the research in this thesis, that is Social Force models, a Cellular Automaton model, a velocity-based model and discrete-choice models. For each model, we explain the basic concept and the parameters which need to be considered in the model calibration.

Furthermore, the implementations of a selected subset of these models will be examined using test cases from the RiMEA-Guideline Rogsch et al. (2014). The results of this analysis provide an initial verification and validation of the models based on their parameter sets as reported in the respective literature.

3.1 Description of Pedestrian Modeling Approaches

For performing pedestrian simulations, various academic tools, e.g. NOMAD (Hoogendoorn (2003)), Hermes (Holl et al. (2014)), MATSim (Dobler and Lämmel (2014)), and commercial software, e.g. SimWalk (Savannah Simulations), PedGo (TraffGo), VisWalk (PTV), MassMotion (Oasys Software), Cast (ARC), Legion (Legion International Limited), AnyLogic (AnyLogic), Myriad II (Crowd Dynamics), exist.

On the operational level, many of them are based or are closely related to the *Social Force* approach which was first described in Helbing and Molnár (1995). Inspired by the principles of the Social Force model different variations have been proposed in the scientific literature such as in Lakoba et al. (2005), Parisi et al. (2009), Seyfried et al. (2006). Based on the research in the field of traffic flow simulations, Burstedde et al. (2001) developed an advanced *Cellular Automaton* approach which is also applicable for

simulating pedestrian movement. Within the last decade, this discrete-space model gained significant popularity since it requires less computational effort to perform simulations including a high number (i.e. more than 10000) of pedestrians in parallel due to its simple structure. To overcome some of the limitations of the Cellular Automaton model (e.g. all cells are identical, movement on a rectangular grid structure), the *Optimal Steps Model* from Seitz and Köster (2012) models stepwise movement as a local discretization on a circle around virtual pedestrians. The traditional approaches, such as the Social Force approach presented in Helbing and Molnár (1995) or the Cellular Automaton model from Burstedde et al. (2001) rely only on the current position of pedestrians in the scene for deriving the next step. Recently, more advanced models evolved which attempt to imitate more natural behavior by also including (short-term) predictions of individual movement. These models are termed *velocity based models* as they are based on the estimation of the velocity vector of each individual. One example of this class of models is the Optimal Reciprocal Collision Avoidance model from van den Berg et al. (2011). For a more comprehensive review on state-of-the-art crowd motion simulation models the reader is referred to Duives et al. (2013).

In this work, we focus our investigations on a selected set of operational pedestrian simulation models. The choice of models is based on including approaches which are widespread (i.e. Social Force and Cellular Automaton model) or have recently emerged and revealed promising results (i.e. Optimal Reciprocal Collision Avoidance and Optimal Steps model). The details of the selected models are described in the following.

3.1.1 Social Force Model

Given that the movement of a person depends on velocity and hence on acceleration, the principle of the Social Force model aims at representing individual walking behavior as a sum of different accelerations as

$$\mathbf{f}_\alpha(t) = \frac{v_\alpha^0 \mathbf{e}_\alpha - \mathbf{v}_\alpha}{\tau} + \sum_{\beta \neq \alpha} \mathbf{f}_{\alpha\beta}(t) + \sum_i \mathbf{f}_{\alpha i}(t). \quad (3.1)$$

The acceleration \mathbf{f}_α at time t of an individual α towards a certain goal is defined by the desired direction of movement \mathbf{e}_α with a desired speed v_α^0 . Here, the current velocity \mathbf{v}_α is adapted to the desired speed v_α^0 within a certain relaxation time τ . The movement of a pedestrian α is influenced by other pedestrians β which is modeled as a repulsive acceleration $\mathbf{f}_{\alpha\beta}$. A similar repulsive behavior for static obstacles i (e.g. walls) is represented by the acceleration $\mathbf{f}_{\alpha i}$. For notational simplicity, we omit the dependence on time t for the rest of the thesis.

From the set of different formulations of the Social Force model available in the scientific literature, we compare three variations of the Social Force model based on the general formulation (3.1).

SF^A: The first model from Helbing and Molnár (1995) is based on a circular specification of the repulsive force given as

$$\mathbf{f}_{\alpha\beta}^A = a_p e^{-\frac{(r_\alpha + r_\beta - \|\mathbf{d}_{\alpha\beta}\|)}{b_p}} \frac{\mathbf{d}_{\alpha\beta}}{\|\mathbf{d}_{\alpha\beta}\|}, \quad (3.2)$$

where r_α and r_β denote the radii of pedestrians α and β , and $\mathbf{d}_{\alpha\beta}$ is the distance vector pointing from pedestrian α to β . The interaction of pedestrian α is parameterized by the strength a_p and the range b_p , where their values are determined in the model calibration process. The model parameters which need to be calibrated are listed in Table 3.1.

SF^B: The second model uses the elliptical specification of the repulsive force as described in Helbing and Johansson (2009) determined by

$$\mathbf{f}_{\alpha\beta}^B = a_p e^{-\frac{w_{\alpha\beta}}{b_p}} \frac{\mathbf{d}_{\alpha\beta}}{\|\mathbf{d}_{\alpha\beta}\|}, \quad (3.3)$$

where the semi-minor axis $w_{\alpha\beta}$ of the elliptic formulation is given by

$$w_{\alpha\beta} = \frac{1}{2} \sqrt{(\|\mathbf{d}_{\alpha\beta}\| + \|\mathbf{d}_{\alpha\beta} - (\mathbf{v}_\beta - \mathbf{v}_\alpha) \Delta t\|)^2 - \|(\mathbf{v}_\beta - \mathbf{v}_\alpha) \Delta t\|^2}. \quad (3.4)$$

Here, the velocity vectors \mathbf{v}_α and \mathbf{v}_β of pedestrians α and β are included, allowing to take into account the step size of pedestrians. That is, the step size of pedestrian α is denoted by $v_\alpha \Delta t$. The model parameters which need to be calibrated are listed in Table 3.2.

SF^C: The third model is an implementation of Rudloff et al. (2011b) in which the repulsive force is split into one force directed in the opposite of the walking direction, i.e. the *deceleration force*, and another one perpendicular to it, i.e. the *evasive force*. Here, the repulsive force is given as

$$\mathbf{f}_{\alpha\beta}^C = \underbrace{\mathbf{n}_\alpha a_d e^{\frac{-b_d \theta_{\alpha\beta}^2}{v_{\text{rel}}} - c_d \|\mathbf{d}_{\alpha\beta}\|}}_{\text{deceleration force}} + \underbrace{\mathbf{p}_\alpha a_e e^{\frac{-b_e |\theta_{\alpha\beta}|}{v_{\text{rel}}} - c_e \|\mathbf{d}_{\alpha\beta}\|}}_{\text{evasive force}}, \quad (3.5)$$

where \mathbf{n}_α is the direction of movement of pedestrian α and \mathbf{p}_α its perpendicular vector directing away from pedestrian β . Furthermore, $\theta_{\alpha\beta}$ is the angle between \mathbf{n}_α and $\mathbf{d}_{\alpha\beta}$ and v_{rel} denotes the relative velocity between pedestrians α and β .

Note that the repulsive force from static obstacles $\mathbf{f}_{\alpha i}$ is modeled by using the same functional form as given by the repulsive force from pedestrians. Here, the point of an obstacle i closest to pedestrian α replaces the position β and \mathbf{v}_i is set to zero. Furthermore, we take into account that pedestrians have a higher response to other pedestrians in front of them by including an anisotropic behavior, as described in Helbing and Johansson (2009), into the first two formulations. In the model, this anisotropic behavior is represented by an angular-dependent prefactor defined by

$$w(\varphi_{\alpha\beta}) = \left(\lambda_\alpha + (1 - \lambda_\alpha) \frac{1 + \cos(\varphi_{\alpha\beta})}{2} \right), \quad (3.6)$$

where $\lambda_\alpha \in [0, 1]$ regulates the strength of interactions from behind. The model parameters which need to be calibrated are listed in Table 3.3.

Parameter	Description	Range
τ	Relaxation time.	$[0, 1]$
a_p	Strength of the interaction force between pedestrian α and other pedestrians.	$[0, \infty[$
b_p	Range of the interaction force between pedestrian α and other pedestrians.	$[0, \infty[$
a_o	Strength of the interaction force between pedestrian α and obstacles.	$[0, \infty[$
b_o	Range of the interaction force between pedestrian α and obstacles.	$[0, \infty[$

Table 3.1: List of parameters which are used for calibrating the SF^A model.

Parameter	Description	Range
τ	Relaxation time.	$[0, 1]$
a_p	Strength of the interaction force between pedestrian α and other pedestrians.	$[0, \infty[$
b_p	Range of the interaction force between pedestrian α and other pedestrians.	$[0, \infty[$
a_o	Strength of the interaction force between pedestrian α and obstacles.	$[0, \infty[$
b_o	Range of the interaction force between pedestrian α and obstacles.	$[0, \infty[$
$\lambda_{\alpha p}$	Anisotropic interaction behavior between pedestrian α and other pedestrians.	$[0, \infty[$
$\lambda_{\alpha o}$	Anisotropic interaction behavior between pedestrian α and obstacles.	$[0, \infty[$

Table 3.2: List of parameters which are used for calibrating the SF^B model.

Parameter	Description	Range
τ	Relaxation time.	$[0, 1]$
a_d	Strength of the deceleration force between pedestrian α and other pedestrians and obstacles.	$[0, \infty[$
b_d	Angular dependence of the deceleration force between pedestrian α and other pedestrians and obstacles.	$[0, \infty[$
c_d	Range of the deceleration force between pedestrian α and other pedestrians and obstacles.	$[0, \infty[$
a_e	Strength of the evasive force between pedestrian α and other pedestrians and obstacles.	$[0, \infty[$
b_e	Angular dependence of the evasive force between pedestrian α and other pedestrians and obstacles.	$[0, \infty[$
c_e	Range evasive behavior between pedestrian α and other pedestrians and obstacles.	$[0, \infty[$

Table 3.3: List of parameters which are used for calibrating the SF^C model.

3.1.2 Cellular Automaton Model

In Burstedde et al. (2001) a two-dimensional Cellular Automaton (CA) model is presented for simulating pedestrian movement. Each cell has a size of $40 \times 40 \text{ cm}^2$ and can either be empty or occupied by exactly one pedestrian. As illustrated in Figure 3.1, the probabilities for moving a pedestrian are encoded in a 3×3 matrix $M_{i,j}$ where the central element describes the probability for the pedestrian not to move at all, while the remaining 8 correspond to a move to the neighboring cells. If a cell is occupied, the probability is set to zero. The update is performed in parallel for all pedestrians and conflicts are resolved according to the following rules: If no other pedestrian targets the desired cell, the move is executed. If more than one pedestrian share the same target cell, one is chosen according to the relative probabilities based on which each pedestrian has chosen the target. The first ranked pedestrian moves while its rivals for the same target keep their position.

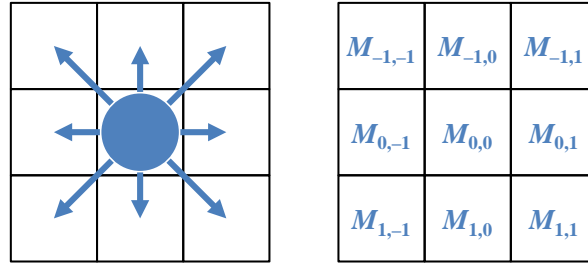


Figure 3.1: Possibilities for a pedestrian to move to the neighboring cells and probabilities for moving encoded in a 3×3 matrix.

To take into account interactions between pedestrians and the geometry of their surrounding environment, a static floor field $S_{i,j}$ is used which does not evolve over time. This allows to specify regions of space which are not accessible by pedestrians due to obstructions such as walls. The static floor field also describes the shortest distance to the target position of an individual. It is calculated such that the field values are increasing the closer they are to the target.

Long-range interactions between pedestrians are modeled using a dynamic floor field $D_{i,j}$ which modifies the transition probabilities to neighboring cells. The model is based on an idea similar to chemotaxis whereas pedestrians follow a virtual rather than a chemical trace. This allows, for instance, to model the behavior of following other pedestrians. The dynamic floor field can be modified by the motion of the pedestrians and is subject to diffusion and decay in order to broaden and dilute the trace. The model uses parameters to control the intensity of diffusion and the decay individually.

For the research in this thesis, we use the version of the Cellular Automaton model as described in Kirchner and Schadschneider (2002). Note that they use a matrix for the transition probabilities with Von Neumann neighborhood, thus limiting the freedom of movement to the four orthogonally surrounding cells of an individual.

In order to model the movement and interactions of pedestrians, the following update rules are applied to all pedestrians at the same time:

1. The dynamic floor field D decays with probability $\delta \in [0, 1]$ and diffuses with probability $\gamma \in [0, 1]$ to one of its neighboring cells.
2. For each pedestrian, the transition probabilities $p_{i,j}$ for a move to an unoccupied neighbor cell (i, j) are determined by

$$p_{ij} = N \exp(k_D D_{ij}) \exp(k_S S_{ij}) (1 - n_{ij}) \xi_{ij}, \quad (3.7)$$

where the two parameters $k_D \in [0, \infty[$ and $k_S \in [0, \infty[$ are used as weights for the values of the fields D and S . The occupation number n_{ij} and obstacle number ξ_{ij} are set to 0 if cell (i, j) is blocked by other pedestrians or walls, respectively, and are otherwise 1. Furthermore, the normalization factor N is set such that $\sum_{i,j} p_{ij} = 1$.

3. Each pedestrian selects a target cell based on the transition probabilities p_{ij} determined in the previous step.
4. Conflicts are resolved based on the relative probabilities of the individuals that have chosen the same target cell.
5. Whenever an individual moves from cell (i, j) to one of its neighboring cells, the starting cell is increased by one, i.e. $D_{i,j} \rightarrow D_{i,j} + 1$.

The model parameters for the Cellular Automaton which need to be calibrated are listed in Table 3.4.

Parameter	Description	Range
k_D	Weight of the dynamic floor field D .	$[0, \infty[$
k_S	Weight of the static floor field S .	$[0, \infty[$
γ	Diffusion probability of the dynamic floor field D .	$[0, 1]$
δ	Decay probability of the dynamic floor field D .	$[0, 1]$

Table 3.4: List of parameters which are used for calibrating the Cellular Automaton model.

3.1.3 Optimal Reciprocal Collision Avoidance Model

The approach of the Optimal Reciprocal Collision Avoidance (ORCA) model as described in van den Berg et al. (2011) implies that each individual takes into account the observed velocity of other individuals in order to avoid collisions. Individuals are reciprocally collision-avoiding (they "share the responsibility") and it is guaranteed that two particular individuals are collision-free for at least a fixed amount of time into the future. Note that the following description of the ORCA model is closely based on the paper of van den Berg et al. (2011).

Each pedestrian α has a current position \mathbf{p}_α , a current velocity \mathbf{v}_α and a radius r_α . It is assumed that these parameters can be observed by other pedestrians. Additionally, each pedestrian possess a preferred velocity $\mathbf{v}_\alpha^{\text{pref}}$ and a maximum speed v_α^{max} , which are both not observable by other pedestrians. Pedestrians cannot communicate with each other, however, they assume that all pedestrians use the same strategy for selecting a new velocity. The velocity obstacle $VO_{\alpha|\beta}^\tau$ is the set of all relative velocities of pedestrian α with respect to pedestrian β that will result in a collision between α and β at some moment before time τ , as illustrated in Figure 3.2. If pedestrians α and β keep moving at their current velocity, a collision will occur before time τ in case of $\mathbf{v}_\alpha - \mathbf{v}_\beta \in VO_{\alpha|\beta}^\tau$, or equivalently $\mathbf{v}_\beta - \mathbf{v}_\alpha \in VO_{\beta|\alpha}^\tau$. In turn, if $\mathbf{v}_\alpha - \mathbf{v}_\beta \notin VO_{\alpha|\beta}^\tau$, pedestrian α and β are guaranteed to be collision-free for at least τ time.

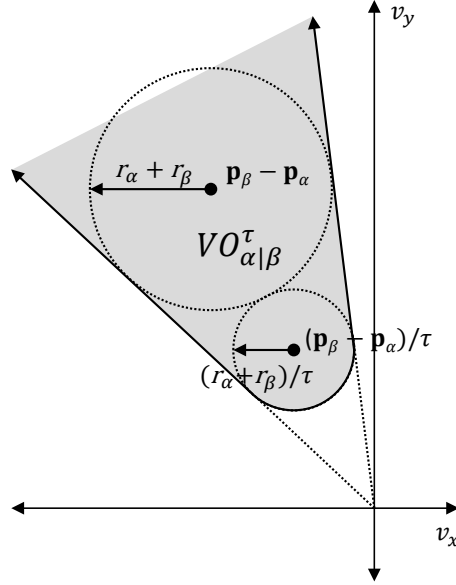


Figure 3.2: Geometric interpretation of the velocity obstacle $VO_{\alpha|\beta}^\tau$ (gray) as a truncated cone with its apex at the origin (in velocity space) and its legs tangent to the disc of radius $r_\alpha + r_\beta$ centered at $\mathbf{p}_\beta - \mathbf{p}_\alpha$. The cone is truncated by an arc of a disc of radius $(r_\alpha + r_\beta)/\tau$ centered at $(\mathbf{p}_\beta - \mathbf{p}_\alpha)/\tau$. The velocity obstacle shown here is for $\tau = 2$ (see van den Berg et al. (2011)).

For each other individual, the model derives a half-plane (in velocity-space) of velocities that are allowed to be selected in order to guarantee collision avoidance (see Figure 3.3). From the pairs of sets of velocities V_α for α and V_β for β one has to select the pair that maximizes the amount of permitted velocities *close* to optimization velocities $\mathbf{v}_\alpha^{\text{opt}}$ for α and $\mathbf{v}_\beta^{\text{opt}}$ for β . These sets are denoted $ORCA_{\alpha|\beta}^\tau$ for α and $ORCA_{\beta|\alpha}^\tau$ for β and represent each a half-plane which contains velocities that are reciprocally collision-avoiding and maximal. Assuming that adopting velocities $\mathbf{v}_\alpha^{\text{opt}}$ and $\mathbf{v}_\beta^{\text{opt}}$ will lead to a collision of α and β , i.e. $\mathbf{v}_\alpha^{\text{opt}} - \mathbf{v}_\beta^{\text{opt}} \in VO_{\alpha|\beta}^\tau$, vector \mathbf{u} denotes the shortest distance between $\mathbf{v}_\alpha^{\text{opt}} - \mathbf{v}_\beta^{\text{opt}}$ and the boundary of the velocity obstacle, and \mathbf{n} is the outward normal of the boundary. Since both individuals share the responsibility of avoiding collisions, each individual has to adapt its velocity by (at least) $\frac{1}{2}\mathbf{u}$. Thus, the set $ORCA_{\alpha|\beta}^\tau$ of permitted velocities for α is the half-plane pointing in the direction of \mathbf{n} starting at the point $\mathbf{v}_\alpha^{\text{opt}} + \frac{1}{2}\mathbf{u}$. As shown in Figure 3.3, the set $ORCA_{\beta|\alpha}^\tau$ for β is defined symmetrically.

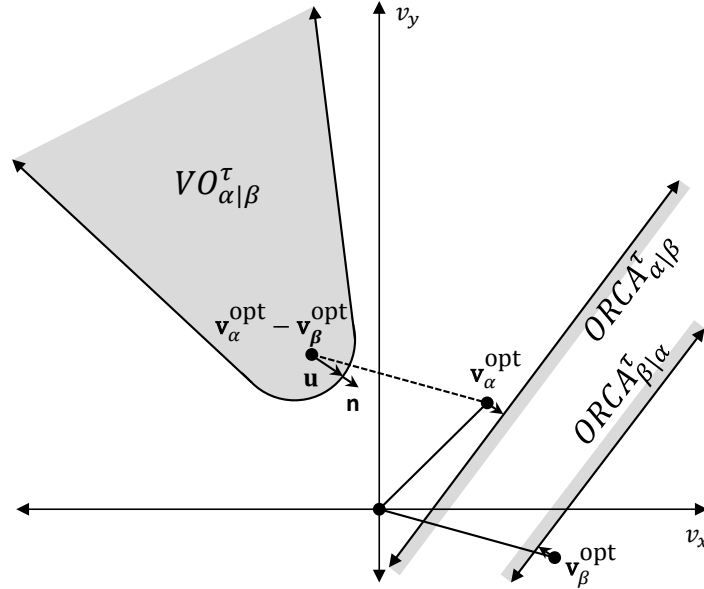


Figure 3.3: The set $ORCA_{\alpha|\beta}^\tau$ of permitted velocities for α for optimal reciprocal collision avoidance with β is a half-plane delimited by the line perpendicular to \mathbf{u} through the point $\mathbf{v}_\alpha^{\text{opt}} + \frac{1}{2}\mathbf{u}$, where \mathbf{u} is the vector from $\mathbf{v}_\alpha^{\text{opt}} - \mathbf{v}_\beta^{\text{opt}}$ to the closest point on the boundary of $VO_{\alpha|\beta}^\tau$ (see van den Berg et al. (2011)).

Each individual selects its optimal velocity from the intersection of all permitted half-planes, which can be computed efficiently using linear programming. Under certain conditions with high densities, the resulting linear program may be infeasible, in which case the ORCA model selects the *safest possible* velocity using a three-dimensional linear program. For avoiding collisions with static obstacles the same approach is used as for the pedestrians. Since obstacles do not move, however, the person takes full responsibility of avoiding collisions with them.

In this work we use the RVO2 C++ library¹ as the implementation of the ORCA algorithm. In order to setting up a simulation run, the RVO2 C++ library allows to define a set of parameters. For calibrating the ORCA model in this study, we only use a subset of the available model parameters which are illustrated in Table 3.5.

Parameter	Description	Range
τ_p	The minimal amount of time for which the agent's velocities that are computed by the simulation are safe with respect to other agents. The larger this number, the sooner this agent will respond to the presence of other agents, but the less freedom the agent has in choosing its velocities. Must be positive.	$[0, \infty[$
τ_o	The minimal amount of time for which the agent's velocities that are computed by the simulation are safe with respect to obstacles. The larger this number, the sooner this agent will respond to the presence of obstacles, but the less freedom the agent has in choosing its velocities. Must be positive.	$[0, \infty[$

Table 3.5: List of parameters which are used for calibrating the ORCA model (see <http://gamma.cs.unc.edu/RVO2/>).

¹RVO2 Library C++ v2.0.1 (released October 26, 2010), see <http://gamma.cs.unc.edu/RVO2/>

3.1.4 Optimal Steps Model

The Optimal Steps Model (OSM) was first described in Seitz and Köster (2012) and has been further developed in Seitz and Köster (2014). In this model, the movement of pedestrians is modeled stepwise in arbitrary directions using attractive and repulsive potentials. Hence, a spatial discretization within the simulation is used and reflects the idea of a natural stepwise movement to which individuals decide where to make the next step. While in Cellular Automaton pedestrians are represented by cells and limited to movement from cell to cell, the OSM models pedestrians by their position and extension in space. For each individual the next position is determined by the distance one can cover with one step. Hence, in Seitz and Köster (2012) the next position is the point with highest potential selected from a set of possible points which are distributed on a circle with the radius of the individual's step length around the current position. The potential for each point is derived by aggregating potential functions of attraction and repulsion from other pedestrians and static obstacles. Note that Antonini et al. (2006) presented a similar approach using a region of interest situated in front of a pedestrian embedded in a discrete choice framework.

An extension of the original OSM formulation was presented in Seitz and Köster (2014) where functions represent utilities on multiple circles within the possible step range and the next position is determined through maximization. In this work, both OSM approaches, Seitz and Köster (2012) and Seitz and Köster (2014), are used for the investigations. Note that in Seitz and Köster (2012) the term potential is used and higher values are more repulsive than lower values. For consistency reasons, this work uses the formulation of utility functions in both OSM approaches which are the negative potentials. In the following the approach from Seitz and Köster (2012) is denoted by OSM^A, and from Seitz and Köster (2014) by OSM^B respectively.

In both OSM approaches, the movement of a pedestrian towards a certain destination is represented by a potential field on a two-dimensional grid. This field encodes the shortest travel time from the destination to any cell in the grid given by the solution to the Eikonal equation. The Fast Marching algorithm by Sethian (1999) is an efficient numerical method to solve the Eikonal equation. To obtain a potential value for an arbitrary point \mathbf{x} in the plane bilinear interpolation is used. The negated arrival time is used as the utility function $u_t(\mathbf{x})$ for the attraction to the target.

In order to avoid collisions with other pedestrians or static obstacles, repulsive functions based on the Euclidean distance are used. The utility function of pedestrian β affecting another pedestrian at position \mathbf{x} is given by

$$u_{p,\beta}(\mathbf{x}) = \begin{cases} -\mu_p & \text{if } d_\beta(\mathbf{x}) - 2r \leq 0 \\ -h_p f_p(\mathbf{x}) & \text{if } 0 < d_\beta(\mathbf{x}) - 2r < w_p, \\ 0 & \text{else} \end{cases} \quad (3.8)$$

with $d_\beta(\mathbf{x})$ being the Euclidean distance from \mathbf{x} to the center of pedestrian β and r denoting the radius of a pedestrian's torso. In order to avoid that the torso of a pedestrian at position \mathbf{x} overlaps with the torso of pedestrian β , i.e. $d_\beta(\mathbf{x}) \leq 2r$, the utility is set to

a low level encoded by parameter μ_p . In the range from physical contact between two pedestrian torsos until w_p , utilities are modeled by $f_p(\mathbf{x})$. According to Seitz and Köster (2012) and Seitz and Köster (2014), we use $r = 0.2$ and $\mu_p = 1000$. Model parameters w_p (width) and h_p (height) control the reach and intensity of the function, respectively.

Following the scheme for repulsion from other pedestrians, the repulsive utility induced by obstacle i , is defined by

$$u_{o,i}(\mathbf{x}) = \begin{cases} -\mu_o & \text{if } d_i(\mathbf{x}) - r \leq 0 \\ -h_o f_o(\mathbf{x}) & \text{if } 0 < d_i(\mathbf{x}) - r < w_o, \\ 0 & \text{else} \end{cases} \quad (3.9)$$

where $d_i(\mathbf{x})$ is the distance to the closest point of the obstacle from position \mathbf{x} . Note that this function uses the shortest distance to the obstacle's border $d_i(\mathbf{x})$ minus the pedestrian's radius r . In case a pedestrian at position \mathbf{x} overlaps with an obstacle, we use the utility $\mu_o = 1000$ as described in Seitz and Köster (2014). If multiple obstacles influence the same point \mathbf{x} , only the one with the lowest utility at this point is considered².

Although, OSM^A and OSM^B both include the utility functions as described in (3.8) and (3.9), they differ in the formulations for $f_p(\mathbf{x})$ and $f_o(\mathbf{x})$.

OSM^A: The utility for repulsion of pedestrian β affecting another pedestrian at position \mathbf{x} within the vicinity of $d_\beta(\mathbf{x}) - 2r < w_p$ is given by

$$f_p^A(\mathbf{x}) = \exp\left(-a_p d_\beta(\mathbf{x})^{b_p}\right). \quad (3.10)$$

As described in Seitz and Köster (2012), we use $a_p = 1$, $b_p = 0.2$, $w_p = 1$, and $h_p = 0.4$ as default parameter values in this work. The utility function $f_o^A(\mathbf{x})$ for obstacles is modeled using the same functional form as in (3.10) with default parameter values $a_o = 3$, $b_o = 2$, $w_o = 6$, and $h_o = 0.2$.

OSM^B: The model uses a compact support utility function as defined by

$$f_p^B(\mathbf{x}) = \exp\left(\frac{1}{((d_\beta(\mathbf{x}) - 2r)/w_p)^2 - 1}\right). \quad (3.11)$$

According to Seitz and Köster (2014), we use $w_p = 0.33$ and $h_p = 1.05$ as default parameter values in this work. Again, we use the formulation in (3.11) to model the utility function $f_o^B(\mathbf{x})$ for obstacles, with default parameter values $w_o = 0.65$ and $h_o = 2$.

All utility functions are then superposed to the overall utility function given by

$$u(\mathbf{x}) = u_t(\mathbf{x}) + u_{p,\beta}(\mathbf{x}) + u_{o,i}(\mathbf{x}). \quad (3.12)$$

Pedestrians select a subset of reachable points for the next step to choose the one with the highest utility. The next step in the simulation represents the step of a real pedestrian.

²Note that in contrast to OSM^A used in this work, Seitz and Köster (2012) included the utility as a sum of all obstacles and set the utility to -10000 to avoid overlapping with obstacles.



Figure 3.4: Examples for step circle discretization (a) from OSM^A with single circle (Seitz and Köster (2012)) and (b) from OSM^B with multiple circles (Seitz and Köster (2014)).

The step length r_s is determined as a function of the individual desired speed v_α^0 defined by

$$r_s(v_\alpha^0) = \beta_0 + \beta_1 v_\alpha^0, \quad (3.13)$$

with $\beta_0 = 0.462$ and $\beta_1 = 0.235$.

OSM^A: a circle is placed around the current position of pedestrian α and the point with the highest utility on it is selected by solving a one-dimensional optimization problem. The radius r_s of the circle is determined by the pedestrian's step length. Hence, each point on the circle denotes a location that can be reached with the next movement step. As shown in Figure 3.4a, the optimization problem can be solved efficiently on an equidistant grid.

OSM^B: also smaller steps than the maximum step length are taken into consideration by solving a two-dimensional optimization problem. This is further simplified by using a two-dimensional equidistant grid over the area of the step circle as numerical optimization scheme. As illustrated in Figure 3.4b, the grid is placed on p concentric circles around the current position of pedestrian α . Furthermore, the pedestrian's direction of motion is constraint by the speed. Thus, only points which fall into the relative angle to the last direction given by the formula

$$\text{angle} = \pi - \text{speed} \quad (3.14)$$

are included. At zero speed a maximum angle of π relative to the last direction is allowed, i.e. pedestrians can move in an arbitrary direction after stopping.

To avoid systematic errors in both OSM approaches, the grid is rotated with a uniformly distributed random offset $\lambda \sim U(0, 1)$. For each position $l = 1, \dots, q_k$ on the step circle k in time step t can be defined by an angle

$$\varphi_{k,l} = \frac{2\pi}{q_k} (l + \lambda), \quad (3.15)$$

with number of grid points q_k given by

$$q_k = \lceil q_p \times k/p \rceil. \quad (3.16)$$

Here, $k = 1$ denotes the innermost and $k = p$ the outermost circle respectively. Note that in OSM^B the same spacing between circles as between the number of grid points q_p on the outermost circle can be derived by $p = \lceil q_p / (2\pi) \rceil$.

The next position within the step circle with radius r_s from the point with the highest utility $u(\mathbf{x}_{t+1})$ is given by

$$\mathbf{x}_{t+1} = \mathbf{x}_t + r_s \times \frac{k}{p} \times (\cos(\varphi_{k,l}), \sin(\varphi_{k,l})). \quad (3.17)$$

The model parameters which need to be calibrated for the OSM^A and OSM^B are listed in Tables 3.6 and 3.7, respectively.

Parameter	Description	Range
w_p	Range of the utility function for the interaction between pedestrians.	$[0, \infty[$
h_p	Intensity of the utility function for the interaction between pedestrians.	$[0, \infty[$
a_p	Intensity of the exponential decay in the utility function for the interaction between pedestrians.	$[0, \infty[$
b_p	Range of the exponential decay in the utility function for the interaction between pedestrians.	$[0, \infty[$
w_o	Range of the utility function for the interaction with obstacles.	$[0, \infty[$
h_o	Intensity of the utility function for the interaction with obstacles.	$[0, \infty[$
a_o	Intensity of the exponential decay in the utility function for the interaction with obstacles.	$[0, \infty[$
b_o	Range of the exponential decay in the utility function for the interaction with obstacles.	$[0, \infty[$

Table 3.6: List of parameters which are used for calibrating the OSM^A model.

Parameter	Description	Range
w_p	Range of the utility function for the interaction between pedestrians.	$[0, \infty[$
h_p	Intensity of the utility function for the interaction between pedestrians.	$[0, \infty[$
w_o	Range of the utility function for the interaction with obstacles.	$[0, \infty[$
h_o	Intensity of the utility function for the interaction with obstacles.	$[0, \infty[$

Table 3.7: List of parameters which are used for calibrating the OSM^B model.

3.2 Model Verification and Validation using RiMEA Test Cases

In order to objectively compare different implementations of microscopic pedestrian simulation models, their performance has to be assessed qualitatively with respect to emerging spatial-temporal patterns (e.g. lane formation) and quantitatively based on evaluation measures with respect to accuracy (e.g. reproducibility of pedestrian densities). As of now, several evaluation measures for assessing different implementations of microscopic pedestrian simulation models have been described and used in the literature. One recent attempt to define a minimum standard for evacuation analysis is stated by the development of the RiMEA-Guideline Rogsch et al. (2014) which includes fourteen test cases for evaluating implementations of pedestrian simulation models.

The RiMEA-Guideline (in German: RiMEA-Richtlinie, Richtlinie für Mikroskopische Evakuierungs Analysen - Guideline for Microscopic Evacuation Analyses; RiMEA-Guideline) is a guideline for German-speaking authorities to evaluate the quality of evacuation analyses for complex buildings. Based on the RiMEA-Guideline expert reports are written to ensure that the fundamental questions of an evacuation analysis are answered. The RiMEA-Guideline has been used in several scientific contributions for the demonstration and evaluation of pedestrian simulation models: in Kretz (2009) a dynamic distance potential field method for route choice on the operational level of pedestrian dynamics has been described and was applied in a simulation of a RiMEA test case. In Davidich and Köster (2012) a cellular automaton based on a hexagonal grid was calibrated and the simulation results were evaluated according to a test provided by RiMEA. Furthermore, the results of different commercial simulation tools (e.g. Viswalk, PedGo, ASERI) with respect to the RiMEA test cases are published on the RiMEA Website Brunner et al. (2009).

In addition the United States' National Institute of Standards and Technology (NIST) recommended a set of seventeen verification tests in order to verify building fire evacuation models Ronchi et al. (2013). In Isenhour and Löhner (2014) the tests recommended by NIST were simulated using the PEDFLOW tool, which lead to the identification of several shortcomings and modifications for further improvements of the tool.

The remainder of this section presents the validation and comparison of the microscopic pedestrian simulation models described in Section 3.1 based on selected test cases from the RiMEA-Guideline. We chose the following modeling approaches for this investigation: the Social Force model (SF^B) Helbing and Johansson (2009), the Optimal Reciprocal Collision Avoidance (ORCA) model van den Berg et al. (2011) and the Optimal Steps Model (OSM^A) Seitz and Köster (2012). The results will reveal the performance of each model individually with respect to the specific tests from the RiMEA-Guideline. Hence, we see this examination also as a first step into model verification (i.e. assessing a model's output for acceptability) and validation (i.e. assessing a model's ability to reproduce the real system). It also will give valuable insights into the major differences between the evaluated pedestrian simulation models which are important for model developers as well as for practitioners.

3.2.1 Description of RiMEA Test Cases

The RiMEA-Guideline Brunner et al. (2009) includes a description of different test cases for evaluating implementations of pedestrian simulation models to reproduce a set of requirements for an evacuation analysis. As of now, 14 test cases are defined in total. In this work we use the following three test cases for the model investigations:

- **Test Case 4:** Specific flow through an opening
- **Test Case 6:** Moving around a corner
- **Test Case 12:** Effects originating from bottlenecks

The comparison in this thesis has put the focus on the core functionality of the investigated operational models only. Hence, we apply test cases which do not include tactical behavior and aspects of dynamic routing (e.g. selection of exits). In the following subsections, the three test cases used in this study are described in detail.

Test Case 4

Based on a periodic boundary system, with a width of 4 m, the specific flow (in persons/ms) should be measured for different densities (in persons/m²) inside the system. The results of this test case are supposed to reveal the relation between specific flow and density in a so-called Fundamental Diagram Weidmann (1993) as shown in Figure 3.5.

Since periodic boundaries are hard to implement in a simulator, we use an approximation for this test case by modeling a corridor 60 m in length and 10 m in width as illustrated in Figure 3.6. Over the available area, we equally distributed pedestrians and varied their total number in different simulation runs in order to generate average

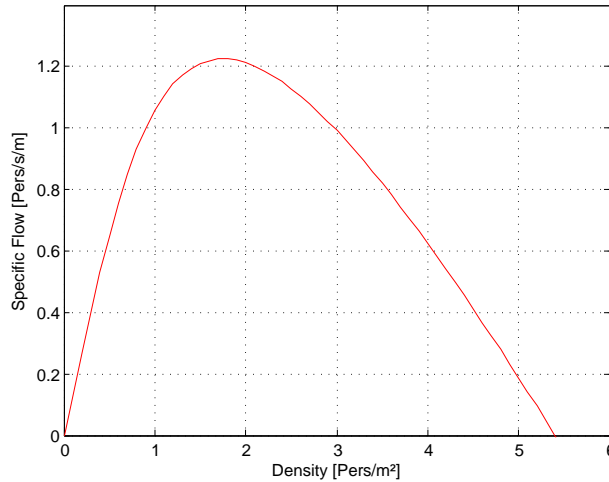


Figure 3.5: Fundamental Diagram representing specific flow (y-axis) and density (x-axis) based on Weidmann (1993).

densities of 1, 2, 3, 4 and 5 persons/m². Each pedestrian should move towards the same end of the corridor. The averages of density and velocity are measured in an interval of 1s inside an area of 4 x 4 m (see blue rectangle in Figure 3.6) located at the center of the corridor. Size and location of the measurement areas have been chosen in order that no boundary effects from walls are measured.

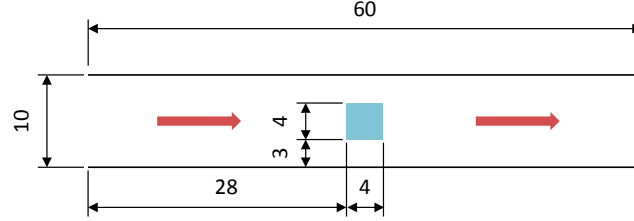


Figure 3.6: Test Case 4 - Pedestrians are equally distributed across the available area and move towards the right end (red line) of the corridor (red arrows denote walking direction). All measures are in m.

Test Case 6

In this test case 20 pedestrians should move around a 90° corner without "crossing" walls. The layout of the corner in this test case is illustrated in Figure 3.7. Furthermore, the walking time for each pedestrian is measured between L_{Start} and L_{End} .

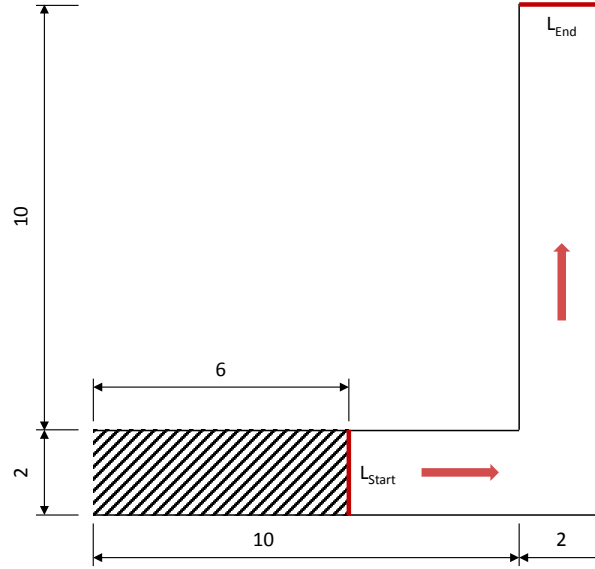


Figure 3.7: Test Case 6 - Pedestrians are placed in the crosshatched area and walk around the corner (red arrows denote walking direction) without crossing walls and corner. All measures are in m.

Test Case 12

In this test case 150 pedestrians should be placed in the crosshatched area of the first room (see Figure 3.8) and should move immediately towards the exit in the second room using the connecting corridor. The results should reveal if congestion appears at the exit. Since the pedestrian flow is limited by the bottleneck in the first room, it is expected that congestion only appears at this location and not at the exit in the second room. Therefore, the density is measured for each room in two different areas (see Figure 3.8): Area A (blue) covers a 1 x 1 m region directly in front of each bottleneck and Area B (orange) covers a region of 5 m² in the vicinity.

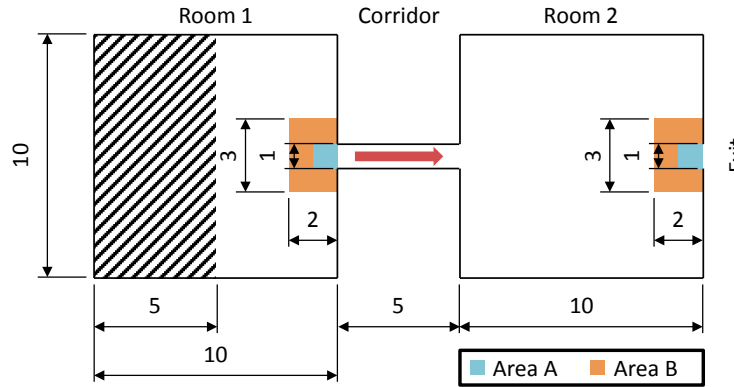


Figure 3.8: Test Case 12 - The bottleneck in Room 1 should lead to clogging while Room 2 is expected to be uncongested. All measures are in m.

3.2.2 Validation Results

We simulated the three test cases using the modeling approaches SF^B , ORCA and OSM^A . For all three models, we defined the desired speed v_α^0 according to Weidmann (1993) from a normal distribution with mean value $\mu = 1.34$ m/s and standard deviation $\sigma = 0.26$. The parameters of the SF^B model were set according to Rudloff et al. (2011b). For the ORCA model the default parameters from the RVO2 C++ library³ were used. The parameters of the OSM^A were set according to the specifications of Seitz and Köster (2012). Note that the parameter sets of the three models were left unchanged during all simulation runs.

In test cases 6 and 12 the final goal is not visible from every point in the starting zone. Therefore an intermediate goal is placed manually to guarantee the validity of all trajectories. The changeover to the final goal takes place when a pedestrian has approached the intermediate goal within the range of one meter.

³RVO2 Library C++ v2.0.1 (released October 26, 2010), see <http://gamma.cs.unc.edu/RVO2/>

Results for Test Case 4

We performed five simulation runs for each average density ranging from 1 to 5 persons/m². All of the tested models were able to simulate pedestrian movement in the defined corridor setting as demanded in the description of the test case in Section 2.1. The resulting estimated Fundamental Diagrams are shown in Figure 3.9.

We find that all three models have the typical flow over density relationship. However, all of them produce significant higher maximum flow rates than in the reference Fundamental Diagram from Weidmann (1993). In case of the ORCA model the maximum is almost four times of the reference Fundamental Diagram and shifted to a higher density. As displayed in Figure 3.9 the match with the Fundamental Diagram from Weidmann (1993) is very poor. By investigating the simulated trajectories, we found that the ORCA model moves the simulated pedestrians almost as a whole block which seems to facilitate that individuals can maintain higher velocities even in scenarios with increased density. The OSM^A produces a good match at low and high densities while exceeding the flow in between. Note that we did not apply the model adaption from Seitz and Köster (2012) to restrict pedestrians from movement if their current speed is higher than the theoretical speed from Weidmann (1993) for the current local density. Although Seitz and Köster (2012) showed that this mechanism results in a good approximation, it also requires using the Fundamental Diagram as an input to the model. It has to be examined if a parameter set can be found that provides a better fit of the Fundamental Diagram without including this mechanism in the model. In this test, the SF^B shows the closest match with the reference Fundamental Diagram from Weidmann (1993).

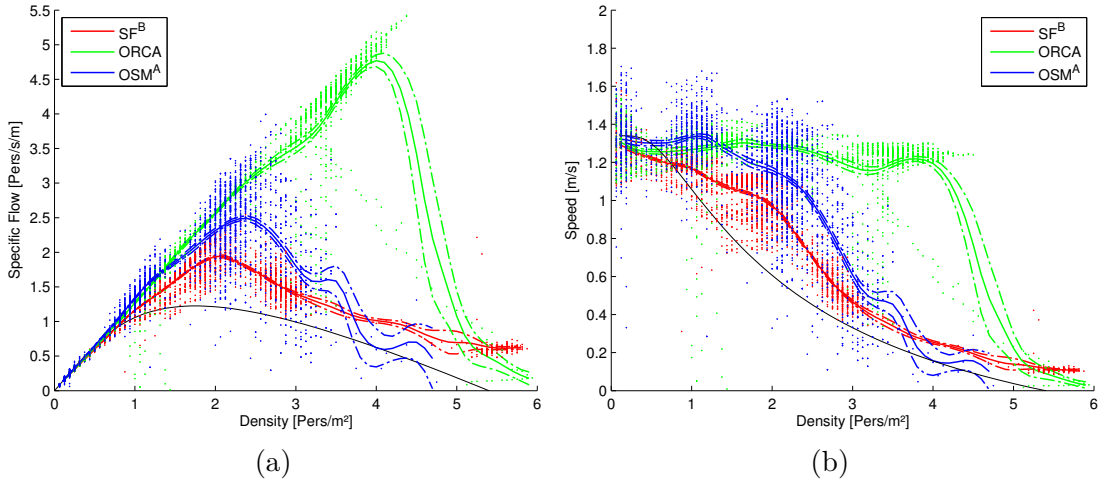


Figure 3.9: Estimated Fundamental Diagrams with (a) flow and (b) speed over density as result from the three tested models using a measurement area of 4 x 4 m from Test Case 4. The black line corresponds to the Fundamental Diagram in Weidmann (1993).

Results for Test Case 6

In this test case, we have performed 10 simulation runs for each model. Our results confirm that all tested models are able to replicate movement around a corner without stepping through the walls. A qualitative evaluation of the simulation for walking around a corner is illustrated in Figure 3.10. It has to be noted that we defined a sub-goal, which is located one meter away from the inner corner on a line connecting the vertices of the inner and outer corner. Thus, pedestrians do not steer directly to the vertex of the inner corner. Figure 3.11 shows the estimated probability density function of the walking times from all simulation runs.

The resulting average and extreme values of the walking times from the 10 simulation runs are shown in Table 3.8. These results show that the three tested models simulate significantly different walking times in this test case. The average walking times are more than 1.3 times as large for the ORCA model than for the OSM^A approach. Pedestrians simulated with the OSM^A can move smoothly around the corner which results in the fastest average walking times. The SF^B model simulated this test case also without any exceedingly strong pedestrian interaction, thus, on average taking only 3.2 seconds longer for all pedestrians to reach their destination than with the OSM^A approach. In contrast, the ORCA model creates congestions in the area of the corner (see Figure 3.10b) which significantly slowed down the pedestrian flow.

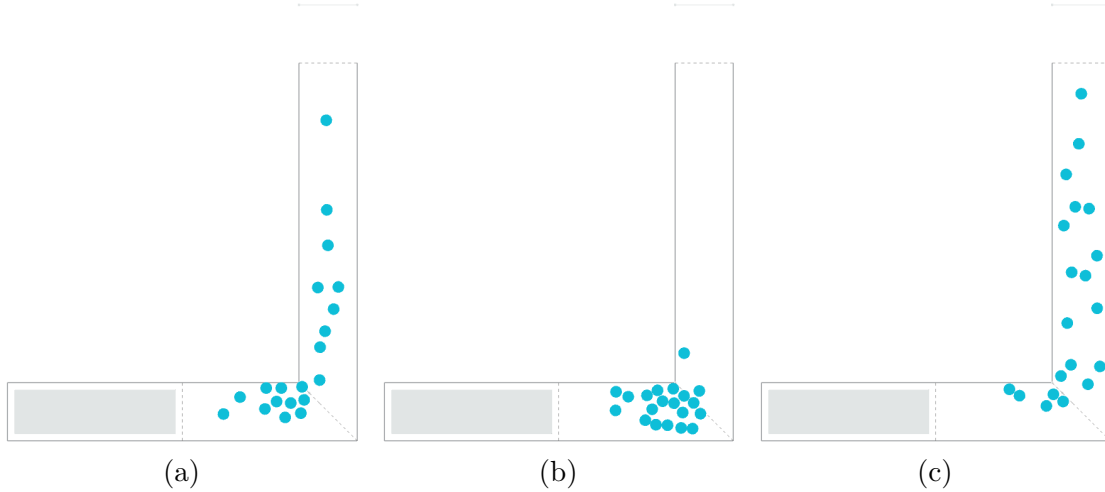


Figure 3.10: Simulation results from (a) SF^B model, (b) ORCA model and (c) OSM^A at time $t = 10s$ for Test Case 6.

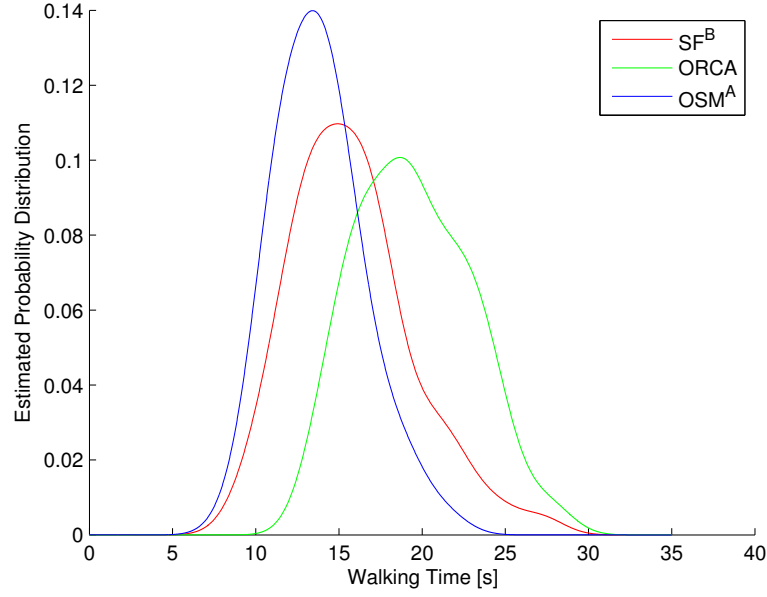


Figure 3.11: Estimated probability density function of walking times from Test Case 6.

Results for Test Case 12

We have performed 10 simulation runs for each model in this test case. Again, we have defined a sub-goal at the center of the entrance to the bottleneck in Room 1. The qualitative results shown in Figure 3.12 reveal the differences in the pedestrian behavior in conjunction with bottlenecks: the Social Force model SF^B creates congestions in front of the bottleneck in Room 1 which forms a half circle. At the beginning there is almost no congestion in front of the bottleneck in Room 2, but over time the density increases too. In contrast, pedestrians are much dispersed in front of the bottleneck in Room 1 in the OSM^A . The model generates two walking lanes inside the corridor most of the time. As a consequence, the throughput is significantly higher than in the two other models. The ORCA model creates strong turbulences in the movement of pedestrians in front of the bottleneck in Room 1. This hinders pedestrians from walking into the corridor and creates unrealistic high waiting times in front of the bottleneck in Room 1.

These qualitative observations are also confirmed by the estimated probability density function of the walking times shown in Figure 3.13. It can be seen that the walking times for the OSM^A are smaller and that the distribution for the SF^B and the ORCA model is significantly broader.

Figure 3.14 illustrates the densities which were measured for the three tested models in the two areas of both rooms. As expected, all models reveal higher densities in Room 1 for Area A. For Area B in Room 1, the SF^B and the ORCA model both reach densities of over 4 persons/m² while the OSM^A stays below this value. In Room 2, only the SF^B model shows higher densities in Area A which is directly in front of the bottleneck. In the surrounding area, that is Area B, the SF^B approach produces higher densities for

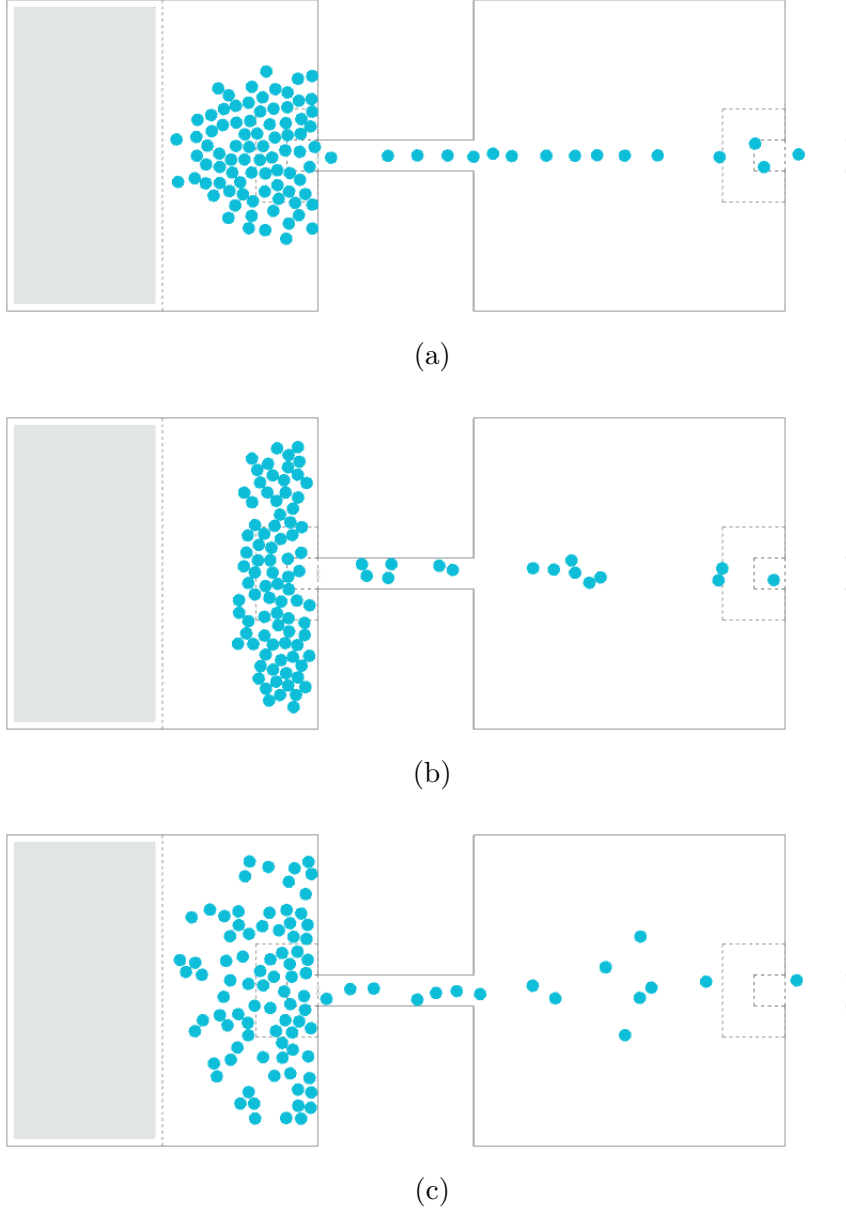


Figure 3.12: Simulation results from (a) SF^B model, (b) ORCA model and (c) OSM^A at time $t = 15s$ for Test Case 12.

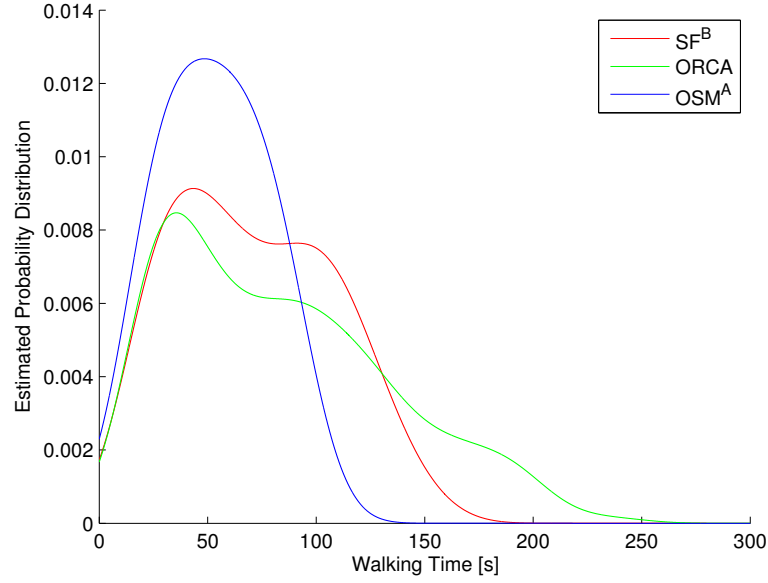


Figure 3.13: Estimated probability density function of walking times from Test Case 12.

a short time while the other two models always stay below 2 persons/m². In contrast, the ORCA model and the OSM^A approach do not create any significant congestions in neither of the two areas within Room 2. It can be seen that this is a result of the inflow restrictions into the bottleneck of Room 1. Hence, the original hypothesis of Test Case 12, namely, that congestion only appears at the exit of the first room and not at the exit of the second room is satisfied by the ORCA model and the OSM^A.

The resulting average and extreme values of the walking times from the 10 simulation runs are shown in Table 3.8. For the OSM^A and the Social Force model, the average walking times are relatively close whereas the values for the ORCA model are twice as large as for the other two tested models.

	Average Maximum Walking Times (min,max) [s]	
	Test Case 6	Test Case 12
SF ^B	22.6 (20.0,27.6)	129.7 (109.3,161.9)
ORCA	25.3 (22.5,28.4)	202.9 (160.8,241.2)
OSM ^A	19.4 (16.2,21.8)	95.0 (85.5,100.2)

Table 3.8: Maximum walking times based on 10 simulation runs for Test Case 6 and Test Case 12.

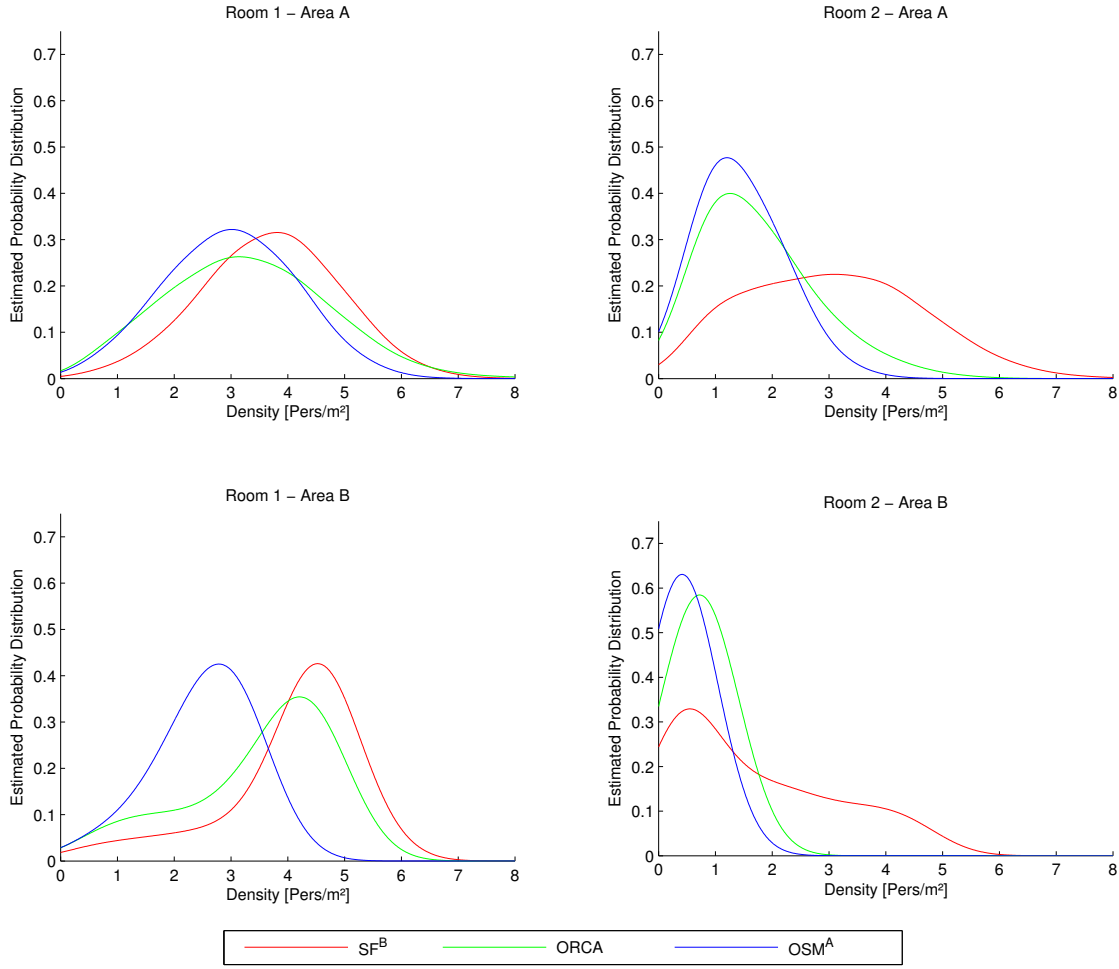


Figure 3.14: Densities measured for the three tested models from Test Case 12.

3.2.3 Discussion of Results

Based on the comparison of the three modeling approaches in Section 3.2 it is hard to infer systematic behavior for each individual model. For instance, the ORCA model revealed the highest flow rates in the Fundamental Diagram in Test Case 4. However, in Test Case 6 and 12, it had the longest average walking times among the tested models. A possible explanation for this behavior is the strong turbulences in the pedestrian flow in front of bottlenecks which occurred in the implementation of the ORCA model (see also Berseth et al. (2014)). Furthermore, wall effects in Test Case 12 keep the pedestrians in the SF^B model mainly in single lanes walking along the corridor whereas in the OSM^A and in the ORCA model pedestrians often walk in double lanes (see Figure 3.12).

From our results of the test cases we cannot disprove any of the three tested models. In fact, the encoded criteria to successfully fulfill the applied test cases are not strict (with the exceptions that pedestrians must reach their goal and must not walk through walls) and lack of quantifiable measures, such as minimum and maximum boundaries for average walking times in Test Case 6 and 12.

Beside the Fundamental Diagram from Weidmann (1993), empirical data from experimental or real-world observations are currently not included in the RiMEA test cases. Since the effects described in the test cases are therefore rather based on assumptions or human observations, there is a strong need for empirical underpinning of these effects. This goes along with an extension of quantitative evaluation metrics for pedestrian movement characteristics beyond, for instance, the Fundamental Diagram.

3.3 Summary

In this chapter we have described the microscopic modeling approaches which will be used in the remainder of this dissertation. These approaches allow simulating pedestrian movement behavior on the operational level based on different modeling principles: accelerations through social forces, transition probabilities for moving between cells, optimal velocities by reciprocal collision avoidance and natural stepwise movement.

In a first attempt to verify and validate microscopic modeling approaches, we have simulated three test cases of the RiMEA-Guideline. Although, the results from these test cases did not allow to thoroughly investigate pedestrian simulation models, they provide the capability to reveal possible implementation faults and basic behavior patterns of individual approaches.

In Chapter 4 we will introduce a flexible simulation framework that facilitates to switch pedestrian models in a simple way and thus constitutes an optimal basis for a structured evaluation of different approaches.

Pedestrian Simulation Framework

In the case of a detailed human interaction analysis one might be interested in when and how individuals avoid collisions or evade from obstacles. A practical application for this is, for instance, how interior train layouts affect the boarding and alighting processes of passengers (e.g. Kogler et al. (2014)). On the other hand, for the evacuation of a whole transit station (e.g. Shi et al. (2012)) the time until all passengers have left a certain area is of vital importance while the detailed interaction of the people might not be the main focus (although of interest in other applications). Moreover, a given application can comprise different spatial areas with varying requirements for human interaction analysis. Only in certain areas high level of detail in terms of interaction between people might be of interest (such as areas of intersecting streams of pedestrians) and not in others (such as corridors with predominantly unidirectional movement).

Currently available simulation application programs typically allow modeling pedestrian movement with one pre-specified simulation model and a single level of detail only (on each of the three levels of decision making, i.e. strategic, tactical and operational, according to Hoogendoorn and Bovy (2004)). However, the simulation of a complex system, such as a public transportation network, with a single model requires a trade-off between the conflicting goals of including sufficient detail to obtain the relevant information and computational tractability.

The above examples show that in order to provide satisfying answers to different questions, one would need to include the complete range of human behavior into a single simulation model. To the best of our knowledge, a single model that covers all these aspects does not exist to date. Hence, the development of different modeling approaches where each of them is tailored to provide a particular set of answers is well-justified. This provides a motivation for the multitude of different models available in the literature. Also, simply combining existing programs to simulate a public transportation network is not feasible due to the involved complexity (with respect to data exchange), inefficiency (with respect to computational performance) and high costs (several, expensive simulation programs are needed).

Recently, the scientific community has drawn more attention to the combination of models with different granularity in a single simulation which has been termed hybrid modeling. For instance, Chooramun et al. (2012) present a novel approach to represent physical space of an environment using three spatial representations within a single integrated software tool, that is a coarse network, a fine network and a continuous representation of the environment. They show that using a mixture of the three spatial representations delivers results of similar accuracy to that produced by the "all continuous" approach while improving the computational efficiency. In Lämmel et al. (2014) a microscopic and a macroscopic pedestrian simulation model are coupled in a way such that essential dynamic properties like flow, density and speed are conserved across model boundaries.

A major goal of this work is to support the trend of hybrid modeling by introducing a simulation framework which allows to combine several different simulation models and to compute them simultaneously based on a highly scalable system architecture¹. This flexibility is achieved by a modular system architecture and a loose coupling of the models. Single simulation models can be switched easily and modelers can select the right model for each spatial area and hence balance the computation load. The simulation framework allows to use and thus combine different models for each level of decision making along the definition of Hoogendoorn and Bovy (2004).

Since the simulation framework supports the switchover of various simulation models, it also facilitates the process of model calibration and validation. By implementing and applying different models within the same framework, a systematic analysis of the strengths and weaknesses of the various approaches can be carried out which will be presented in Chapter 6.

In this chapter, we explain the overall concept, architectural software design and implementation of the flexible simulation framework. Furthermore, the features of switching and combining different models in the framework are demonstrated in two real world case studies: The first case study deals with the problem of designers of urban transit vehicles who need to assess and compare their design choices by predicting the passenger flows in typical situations, i.e. boarding and alighting. We show how three different microscopic models which represent the movement on the operational level can be used to simulate passenger boarding and alighting behavior and evaluate their individual strengths and weaknesses based on several criteria such as the impact on boarding and alighting times. In the second case study, we simulate a subway station next to the main soccer stadium in Vienna where large crowds occur after major events such as sporting competitions or pop concerts. Here, pedestrian simulations can be used to quantify the capacity of key elements (e.g. doors or staircases) and evaluate the infrastructure design and processes of crowd management in combination with large numbers of passengers. We elaborate the differences between applying a microscopic or a macroscopic model on the same scenario based on the simulation results and the computational performance.

¹The work in this chapter is based on contributions by S. Seer, T. Matyus, M. Stubenschrott, C. Kogler and D. Bauer which is gratefully acknowledged.

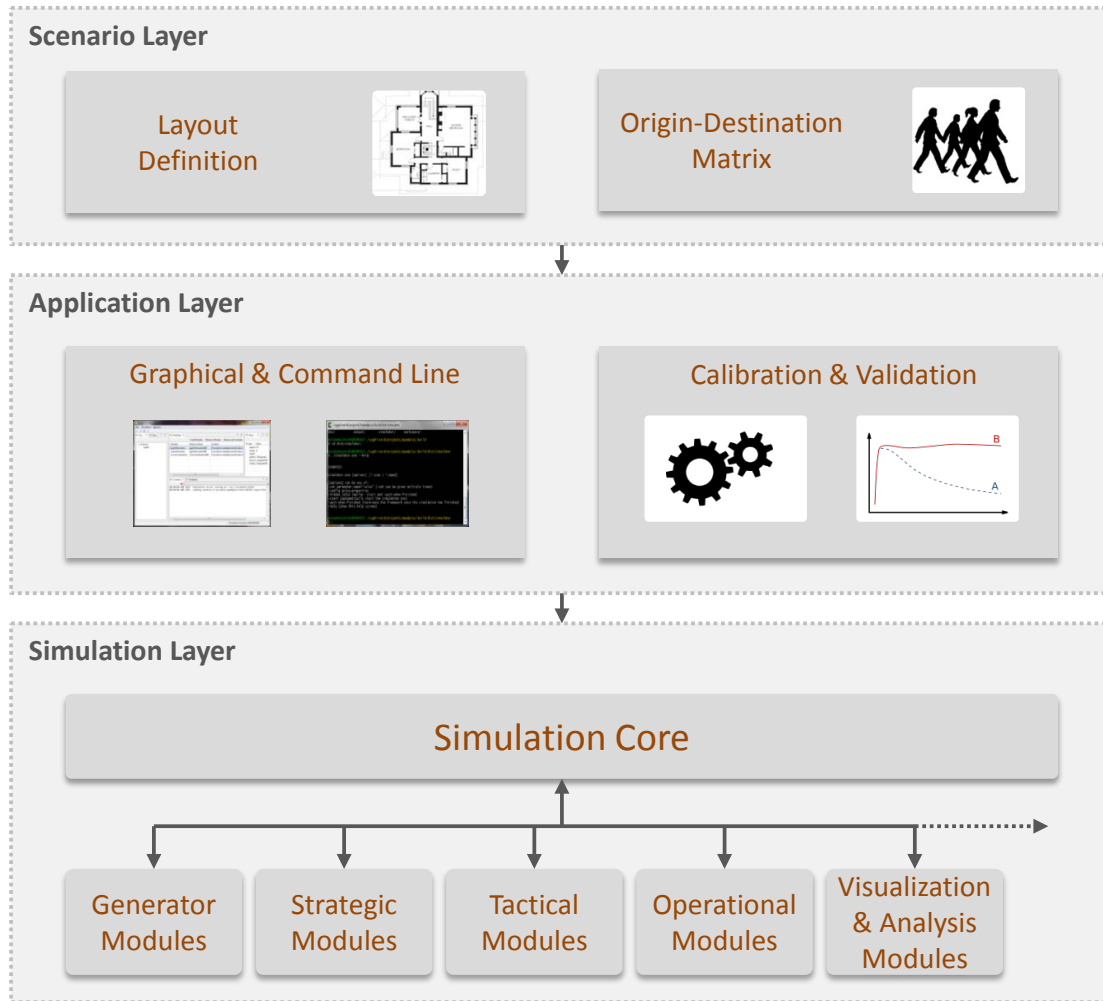


Figure 4.1: System architecture of the simulation framework.

4.1 Concept of the Simulation Framework

The design of the simulation framework relies on a scalable and flexible system architecture in which different functional modules can be easily integrated. Figure 4.1 provides an overview of the system architecture of the simulation framework which can be structured into three layers:

- **Scenario Layer:** Running a simulation requires the upfront specification of information by the user such as infrastructure layout, composition of the simulated crowd and representation of traffic demand specified as *Origin-Destination* (OD) matrices. On this layer, these different specifications are aggregated into the *Scenario Definition*.

- **Application Layer:** This layer represents the link between the scenario definition and the simulation layer. It provides the possibility to configure simulation related parameters, for instance, the simulation duration, the models to be used and the output to be written. It also allows a user to start a simulation run either using a *Graphical User Interface* (GUI) or the command line. In addition, a strategy for *Calibration & Validation* is defined which automatically initiates the necessary simulation runs and performs specific procedures for estimating model parameters or evaluating a model's performance. The methodologies for model calibration and evaluation as well as the results from applying them will be presented in Chapter 6.
- **Simulation Layer:** This layer performs the actual simulation run and includes various functional modules. For flexibility reasons we use a modular architecture including a simulation core as central control component that communicates with several modules: pedestrian movement simulation models are implemented as *Strategic*, *Tactical* and *Operational Modules* along the categorization of Hoogendoorn and Bovy (2004), *Generator Modules* process the simulation input and *Visualization & Analysis Modules* provide the simulation output in various formats.

4.1.1 Scenario Layer

The scenario definition is the main input for each simulation run and consists of the following three fundamental properties:

1. The *infrastructure* describes the layout which can be drawn from scratch with a specifically designed scenario definition tool from Imber (2011) or semi-automatically imported from Computer-Aided Design (CAD) drawings. The infrastructure contains one or more *sections* to model interactions in free walking space (e.g. on different floors of a building) where for each section different modules can be used. Inside these sections obstacles (e.g. walls) can be specified as geometric data, such as polylines, polygons and rectangles. One specific type of section is a *facility* which is used to model doors, stairs, escalators or elevators. These facilities can also be used to connect two sections (e.g. the staircase between two consecutive floors).
2. A *pedestrian* can possess several characteristics such as body size, desired velocity, movement restrictions (e.g. to simulate wheelchair users), which might be chosen randomly from a certain distribution.
3. One or more *OD-matrices* can be used to define the pedestrian flows between each defined entry and exit and hence to assign pedestrians to the infrastructure. For more complex scenarios also the creation time and maximum number of pedestrians in the simulation can be defined.

The output of the scenario definition is stored in an Extensible Markup Language (XML) file, using a format which is a human-readable description of the scenario.

4.1.2 Application Layer

The application layer combines the scenario definition from the input layer with additional user defined configurations for a simulation run (e.g. size of the time steps, maximum duration of a simulation, selection of simulation models) and provides this information to the simulation layer. For loading of scenario definitions and defining configurations, the simulation framework includes a *Graphical User Interface* (GUI), as illustrated in Figure 4.1. Furthermore, modules can be assigned either to specific sections or to all sections of a certain scenario. For instance, it is possible to assign different operational models to different sections. Modules have optionally user-definable parameters which can also be changed using the GUI. The configuration includes scenario-specific settings such as the maximum simulation time or the format of the simulation output (e.g. visualization, storing in files). As setting up a complex scenario can involve to include multiple modules and maybe requires to change certain parameters, one can also save the current configuration to disk and load it afterwards. The configuration process can also be automated via the *Command Line* to facilitate batch processing of many different scenarios.

Once all modules and parameters have been setup for the scenario, the user can run the simulation. For the purpose of model calibration, a *Calibration Strategy* can be defined which includes all necessary configurations and performs multiple simulation runs without any need for user interaction.

4.1.3 Simulation Layer

The simulation layer of the simulation framework is based on a modular architecture which provides several important advantages for the simulation of crowd flows. Since human behavior can be described on three levels (i.e. strategic, tactical and operational), each level can be represented as an individual module within the simulation framework. Thus, certain behavioral aspects such as route-choice can be separated from others and thus form a logical encapsulation. The main advantage, however, is the high degree of flexibility in terms of switching and combining different behavioral models. For instance, given a well-defined interface exists, one can easily change the operational model from a Social Force model to a Cellular Automaton while using the identical routing model on the tactical level.

An advantage of this loose coupling is that the modeler can define to which extent a functionality is split into separate modules. It is possible to perform a complete simulation run with a single module or with multiple different (smaller) modules. Several factors such as communication overhead, requirements for specific projects and personal preference influence the decision on how to encode functions in different modules. The simulation framework includes the *Simulation Core* which provides default implementations for each of the three described levels (i.e. strategic, tactical and operational). The simulation core also acts as a centralized interface, thus connecting dynamically to other loaded modules which can provide certain complementary or additional functionalities (see Figure 4.1).

All *Modules* are separate processes which can be run independently and connect themselves to the simulation core. This has multiple advantages over loading modules as shared libraries:

- Today’s computers are multi-processor machines that can be better utilized by multiple processes without the explicit need to use multi-threading which has its own set of synchronization problems (see Gramoli (2015)).
- Modules can even be run on different machines for enhanced performance given that the network speed is not the bottleneck.
- The development of modules is simplified as they are completely encapsulated and can be started dynamically and linked to the running simulation framework on-the-fly.

In order to compute pedestrian simulations with a broad variety of models on different behavioral levels an efficient and simple communication between modules is of vital importance. In our approach, modules do not communicate directly with each other, they rather use the simulation core as a centralized message broker interface to exchange data as messages (see Figure 4.2). Modules can register to receive certain messages and can also send out own messages. This enables a loose coupling of modules where individual modules may not even have to physically executed on the same machine.

The open source messaging server ActiveMQ (The Apache Software Foundation (2014)) was chosen for efficient and reliable communication between the simulation core and the connected modules. This technique does not put any restrictions on the type and content of messages. ActiveMQ (like any other messaging middleware) has certain performance implications for sending messages. In our tests, the upper limit of messages which could be delivered was roughly 1500 per second, whereas the size of the individual message had only little impact on the throughput. Therefore, we defined our messages such that most modules only need to send a single message per simulation time step.

The following five messages can be classified as *life-cycle messages* which are initialized by the simulation core and represent the main simulation loop in the framework:

- *SET_PARAMETERS* is used to define specific model or simulation parameters. This is the very first message that is sent before the start of a simulation run to initialize the simulation with the required parameter values. In addition, this message can be sent during runtime in order to handle dynamic behavior such as opening and closing doors.
- *INIT* is followed immediately after the *SET_PARAMETERS* message. This message enables each module to setup the internal data structures and serves as a notification that the simulation is about to begin.
- *NEXT_STEP* is sent in each time step of the simulation. The simulation core can send this message either with a constant or adaptive (with respect to the computational demand) interval.

- *SHUTDOWN* is sent when the simulation is stopped. After receiving this message, a module should write pending buffers to disk or can trigger post-simulation analysis.
- *KILL* is the last message which every module receives. It notifies modules that they should immediately terminate upon receiving the message. Otherwise, a module would be forcefully terminated by the simulation core after a certain timeout.

All life-cycle messages are synchronized, that is each module has to explicitly acknowledge that it has finished its calculations within a simulation time step. Only after all modules have sent their confirmation, the following *NEXT_STEP* message is sent out.

In addition to the life-cycle messages, modules can define individual messages in order to facilitate their functionalities. Currently, the following messages are defined for the purpose of pedestrian simulations:

- *ADD_AGENTS* is used to add one or more pedestrians to the simulation. Each pedestrian can have different properties such as specific radius and desired speed.
- *UPDATE_AGENTS* can alter all properties of any pedestrian. The most commonly changed property is the current position.
- *REMOVE_AGENTS* removes one or more pedestrians from the simulation.
- *PERFORM_TASK* is processed by tactical modules to determine the path to the next destination as part of a task. Once a pedestrian has fulfilled the task, the tactical module sends a *PERFORM_TASK_RESULT* message.
- *GOTO_POSITION* is processed by operational modules to move pedestrians to the next intermediate destination of a path. Once a pedestrian has reached his (intermediate) destination, the operational module sends a *GOTO_POSITION_RESULT* message.
- *UPDATE_INFRASTRUCTURE* can be used to update the infrastructure dynamically which allows, for instance, to create new obstacles during the runtime of the simulation.

An important design goal of the simulation framework was the support of different programming languages. Development of human behavioral models goes through different stages from quick prototyping to deployment. In each of these stages the usage of a specific programming language is justified. For instance C++ is a good choice for 3D visualization modules since they often require specialized toolkit support for programming graphics cards. MATLAB is powerful for the rapid implementation of algorithms and plotting of functions and data, thus in particular useful when developing new mathematical models. Java, on the other hand, has large support in the scientific community and also provides good performance and extensive enterprise tools, like refactoring, which is essential in writing complex modules with many different classes and developers. The open source messaging server ActiveMQ (The Apache Software Foundation (2014)) supports many different languages and is very actively maintained and therefore well tested.

In order to support the development of new modules, the simulation core provides a *Communication API* which implements the communication of the modules via ActiveMQ in individual libraries for each supported programming language (see Figure 4.2). Hence, all modules use functionality of the communication middleware and do not need to implement the connection to ActiveMQ message broker by themselves. This avoids redundancy in software code development and keeps the functional design of the modules simple. As illustrated in Figure 4.2, this Communication API supports implementations of modules in C++, Java and MATLAB. Note that it can be extended to any of the supported ActiveMQ client languages (see The Apache Software Foundation (2014)).

In addition, the simulation core shares a collection of implemented functions, such as geometric functions, as part of the *Common Libraries* for reuse by multiple modules.

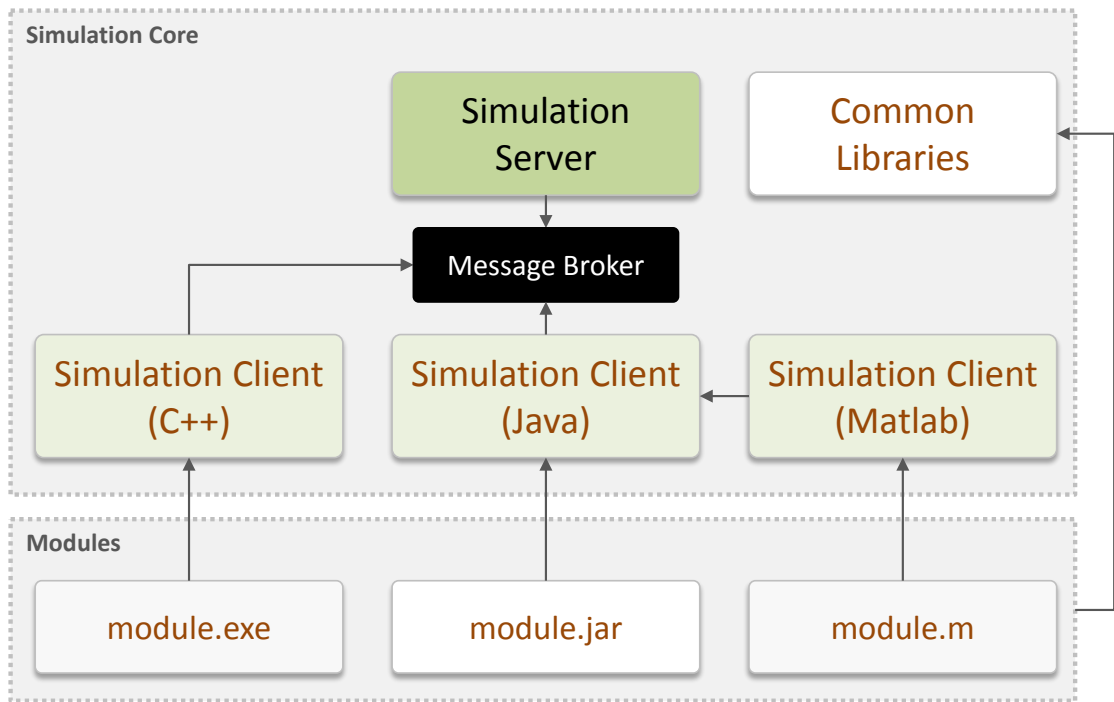


Figure 4.2: Simulation layer implementing cross-language communication with client modules.

4.2 Framework Modules

For a simulation run, modules on all three different behavioral levels - that is *Strategic*, *Tactical* and *Operational Modules* - are used as illustrated in Figure 4.3. Furthermore, *Generator Modules* process the simulation input which, for instance, defines the agents used in the simulation. The simulation output is provided in various formats by *Visualization & Analysis Modules*. Figure 4.3 shows the structured flow of information with the interdependencies of module classes in the simulation framework. In the remainder of this section we will describe the functionality of the required modules for the simulation. Furthermore, we explain the specific model extensions which are required for the simulation of the two case studies in Section 4.3.

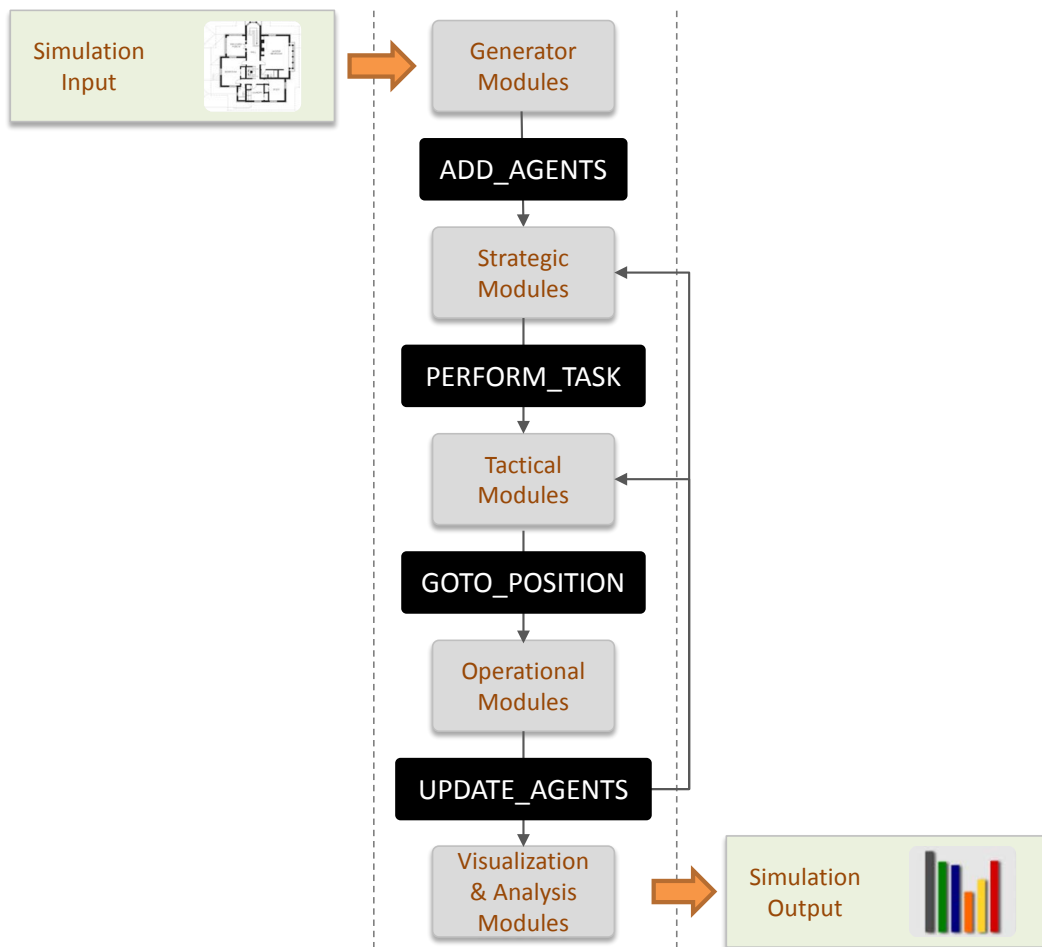


Figure 4.3: Structured flow of information within a single simulation step following the concept of three levels of decision making by Hoogendoorn and Bovy (2004).

4.2.1 Generator Modules

Instead of predefining and generating instances of all pedestrians at startup, *Generator Modules* create individual pedestrians with specific attributes (e.g. desired walking speed and destination) based on Origin-Destination (OD) matrices during simulation runtime. Consequently, all other modules are provided with this information and need to react accordingly when new pedestrians are generated. Typically, the OD-matrices are stored as part of the scenario description.

4.2.2 Strategic Modules

The main function of *Strategic Modules* is to model the strategic plan of an individual such as the choice of desired activities. In most simple applications, this strategic behavior is modeled exogenously, i.e. defined before-hand by the user in form of a pre-trip decision. However, in certain applications it makes sense to use an endogenous modeling approach where strategic behavior is influenced by information generated on the operational or tactical level. This might be crucial, for instance, when the choice to accomplish a specific activity depends on the available time which in turn is influenced by the degree of congestion by other individuals. As for the demonstrations in the case studies in Section 4.3 the strategic decisions are a rather straightforward predefined set of possible activities for all individuals.

4.2.3 Tactical Modules

In complex environments, pedestrians can often choose among alternative routes to reach their destination. The route-choice behavior can be crucial for the spatial and temporal distribution of pedestrian and is therefore represented by *Tactical Modules* in the simulation framework. The decision on the walking path including intermediate destination(s) is typically based on the individual's estimation of the path length with respect to distance or duration. This estimation depends on the location of static and dynamic obstacles as well as on macroscopic features of the environment such as pedestrian densities or flow rates. For instance, when a staircase and an escalator are located next to each other, pedestrians usually prefer to use the escalator. However, based on various factors such as distance, congestion level and personal preferences, some individuals might switch to the staircase (see Zeiler et al. (2011)).

In order to model the route-choice behavior for the case studies in Section 4.3, we implemented the algorithm presented in Stubenschrott et al. (2014) as a tactical module. This routing approach is based on a graph representation of the spatial layout of the environment. In the simulation framework, the infrastructure is represented by sections to model interactions in free walking space. Sections are connected by facilities, such as doors and stairs. We assign two nodes – one at the entrance and one at the exit – to each facility. Each pair of nodes that has a walkable path in between is connected with an edge. This results in a high level graph $G = (V, E)$, with V denoting the M nodes, and E_{ij} the edges of the graph connecting nodes V_i and V_j where $(i \neq j, 0 \leq i < M, 0 \leq j < M)$.

The generation of the high level graph can be achieved automatically, for instance by building a visibility graph as described in Kneidl et al. (2012).

Within a section, all walkable paths between nodes are found by building up a regular grid and applying the Theta* algorithm as described in Daniel et al. (2010). This extension of the A* algorithm (Hart et al. (1968)) is a path planning method that propagates information along grid edges without constraining the paths to the edges. Thus, it finds shorter and more realistic looking paths than A* without losing its computational time efficiency.

Our case study in Section 4.3.2 uses an incomplete graph, which has been created manually, as in real life only a certain subset of edges are utilized by pedestrians. The tactical route choice model calculates pedestrians' decisions on routes dynamically in a two stage process: At the start of the simulation, an initial route from start node V_0 to destination node V_N is derived for each pedestrian using the shortest path algorithm from Dijkstra (1959). During the simulation, the model continuously updates the routes for each pedestrian based on their observations within the environment as the local densities evolve over time.

4.2.4 Operational Modules

The main purpose of an operational model is to perform the locomotion of a pedestrian towards a certain destination while avoiding collisions with dynamic and static obstacles, such as other pedestrians and walls, respectively. For the simulation with our framework, this behavior is encoded in modules that we classify as *Operational Modules*.

We differentiate between two types of operational models with respect to our definition of the infrastructure: the first type are models for simulating interactions in free walking space within *sections*. Therefore, all modeling approaches described in Section 3.1 have been implemented in the simulation framework as individual modules. The second type is represented by models which are embedded in *facilities* such as doors, stairs, escalators and elevators. These models are concerned with the transition of pedestrians between sections and thus provide highly specialized functionalities depending on the particular type of facility.

Operational Modules for Sections

For the case studies in Section 4.3, we use a subset of the modeling approaches described in Section 3.1, i.e. the Social Force models SF^A and SF^B , and the ORCA model. In order to model human movement behavior for the case studies in this chapter more realistically, we have 1) extended the Social Force approaches and 2) implemented a macroscopic model for comparisons with the microscopic models.

Modeling dense waiting crowds, e.g. in front of bottlenecks, staircases or on train platforms, with the Social Force approach typically results in movement behavior where pedestrians "vibrate" back and forth as soon as they are nearby their destination. We extended the Social Force approaches such that pedestrians can switch from an active mode, where they actively strive toward a destination, to a passive mode, where the

attractive force (cf. (3.1)) is set to zero and they are passively exposed to the repulsive forces. In other words, pedestrians are allowed to be "pushed" by other pedestrians while they are waiting. Note that the velocity of a pedestrian in passive mode is set to zero after each step in order to keep the pedestrian close to the current position. The computation of all pedestrians and obstacles within a particular section has a complexity of $O(n^2)$. To increase the computational performance of the Social Force implementations, a pedestrian only takes into account other pedestrians and obstacles which are within a certain radius (e.g. 3 m). Therefore, we generate a regular grid of 1 x 1 m in which the positions of all pedestrians and obstacles are stored. The information in this grid is updated in each time step.

Furthermore, we also need to model the operational behavior in a section with a macroscopic modeling approach for the second case study in this chapter (see Section 4.3). By definition, macroscopic models are not concerned with the modeling of detailed human interaction (see e.g. Predtetschenski and Milinski (1971) and Fruin (1971)). The movement of pedestrians in macroscopic models is depending on aggregated values, such as flow, density and speed. For this purpose, we model the walkable space as a three-dimensional non-planar directed multi-graph that can contain multiple edges to incorporate different walking directions. Since each edge has an assigned area (represented by a polygon) the edge's density is determined by the number of pedestrians currently walking on the edge. Based on Weidmann (1993)'s Fundamental Diagram, the current pedestrian velocity is determined as a function of the density and the corresponding travel time for the considered edge is calculated. At the transition between two edges, it has to be ensured that a) the total capacity of the edge will not be exceeded by inserting an additional person and b) that the local density in the transition area does not exceed the given maximum value. The total capacity of an individual section or facility is determined by its spatial dimension of the walkable area. Note that facilities can include further technical restrictions (e.g. maximum capacity of an elevator) which impacts the available capacity. The transition area is defined by a one meter wide zone along the whole length of the contact line (i.e. the common line of the two polygons) between two edges. This simple concept of a transition area with maximum density is used at the transition from macroscopic to microscopic model region and vice versa. Furthermore, a pedestrian is handed over to the next model, only if the density in the transition area is below a certain maximum value. In the case of transition from a macroscopic to a microscopic model the exact entry position is calculated by extending the trajectory linearly neglecting whether this position is already occupied by another individual. It is left for future research to implement more sophisticated methods which identify free spots, e.g. as described in Lämmel et al. (2014).

Operational Modules for Facilities

Facilities in the simulation framework are representations of physical objects like stairs, escalators or elevators where each yield a different behavior of pedestrians. Based on its type, a facility provides a highly specialized behavioral model. In this work, all facilities are represented by macroscopic models. Hence, the transitions between a facility and the

surrounding walkable area of a section are modeled accordingly. The following list gives an overview of currently supported facilities:

- *Doors* limit the maximum specific pedestrian flow rate to 1.3 pedestrians per meter and second (see Gwynne et al. (2009)). Note that modeling a door by using a facility is purely a choice of the modeler and can alternatively be modeled by a wall opening using obstacles within a section.
- *Elevators* enable pedestrians to move between different floors (i.e. sections within a defined scenario) and have a certain maximum capacity. User-definable parameters for an elevator allow to control the door dwell time and speed.
- *Entrance Controls* limit the pedestrian flow to a user-defined maximum value and can hence be used for turnstiles or meanders which have a certain throughput (e.g. 50.96 pedestrians/minute for a single lane meander according to Seer et al. (2008)).
- *Escalators* model pedestrian movement according to a fixed predefined speed, whereas the inflow rate of the facility is the same as for *Doors*.
- *Stairs* model pedestrian movement according to the Fundamental Diagram defined by Burghardt et al. (2013) using the inflow rate as defined for *Doors*.
- *Transit* facilities model buses or trains arriving at public transport stations according to a given timetable. When a vehicle enters a transit station, pedestrians inside the vehicle are given way to alight first, only then pedestrians waiting on the platform can board the vehicle until the maximum capacity is reached. The actual boarding and alighting rates are again influenced by the vehicle door widths using the same flow rate as for *Door* facilities.

4.2.5 Visualization & Analysis Modules

In order to make the simulation results easily accessible for various users, different *Visualization & Analysis* modules can be included into the framework. Figure 4.4 illustrates our implementation of a 2-dimensional visualization module. This 2D-visualization displays the environment and the location of all individuals within the simulation. Furthermore, it can also be used to analyze crowd behavior based on visualizations of macroscopic indicators such as density plots. As an extension, we implemented a user-friendly 3-dimensional visualization² of the simulation results as shown in Figure 4.5. By selecting a specific visualization from multiple options, professional transport planners can easily and fast analyze effects on crowd flows while the results can also be interpreted by higher level management and policy makers.

²The 3D visualization was developed as part of a research cooperation with Fraunhofer Austria - Visual Computing.

The simulation framework also includes modules which enable to store resulting simulation data in a structured format (e.g. Comma-Separated Values (CSV)). For instance, the simulation output from microscopic models is typically in the form of individual trajectories for each pedestrian including a unique identifier, time step and position as well as the transitions between a section and a facility (and vice versa). Furthermore, the simulation output can include macroscopic information such as density estimations, flow rates or the entering time of a certain facility. Writing raw trajectories in each time step for large amounts of pedestrians can easily result in outputs of several gigabytes, therefore the flexibility to use custom output writer modules for specific applications is important.

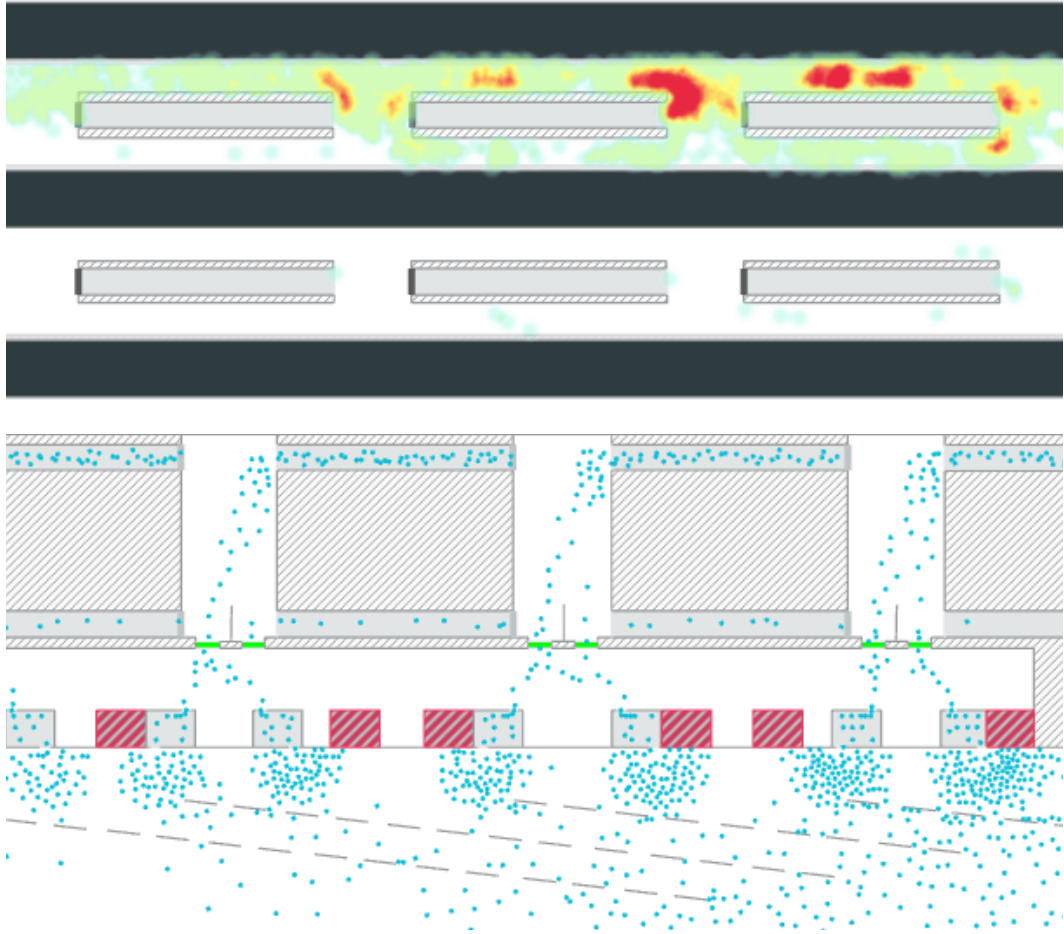


Figure 4.4: 2D Visualization showing the pedestrian density estimation (top) and individual pedestrian positions (bottom) as a result of the simulation.

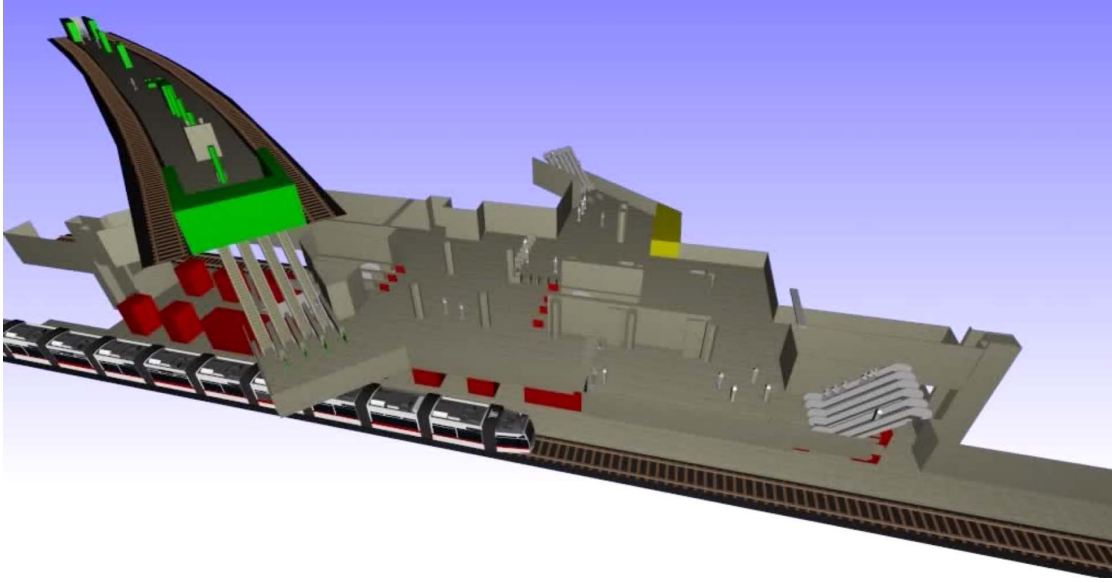


Figure 4.5: 3D Visualization of the pedestrian simulation in the Viennese subway station "Schwedenplatz".

4.3 Case Studies

In this section we demonstrate the flexibility of the framework in terms of switching and coupling different simulation models based on two real world case studies. First we simulate the processes of boarding and alighting of a light vehicle train with three different operational models. The second case study focuses on the simulation of a complex subway station where we discuss the differences in the simulation results when applying two operational models with varying granularity in each simulation run. Information for several key indicators such as computational performance related to number of agents, travel times and flow rates are used for elaborating the differences between simulation approaches.

All simulation runs were performed using a PC with a 2.6 GHz Intel® Xeon® CPU E5-2630 v2, 64 GB DDR3 RAM @ 1600 MHz, and a NVIDIA Quadro K2000 video card running Windows 7 64bit. Furthermore, in all scenarios for both case studies the free walking speed of a person is defined according to Weidmann (1993) by a normal distribution with mean value $\mu = 1.34$ m/s and a standard deviation $\sigma = 0.26$.

4.3.1 Boarding and Alighting at Light Vehicle Trains

The design of urban transit vehicles is a key component which determines the overall capacity of a line in public transportation. Hence, optimizing the process of boarding and alighting as well as passenger flows inside a vehicle is of vital importance. Vehicle designers need to assess and compare their design choices by predicting passenger flows in typical situations. Since field tests involving real or mock-up vehicles are expensive in terms of costs and time, microscopic simulation of passenger flows have proven to be a valuable tool.

In this case study we demonstrate the ability of our simulation framework to investigate passenger flows in designs of urban transit vehicles (see also Kogler et al. (2014)). Together with Bombardier Transportation Light Rail Vehicles (LRV), we applied our simulation methods on a vehicle layout using three different operational models along the description in Section 3.1: the implementations of the Social Force approach SF^B and SF^C as well as the ORCA model. The simulation results of each microscopic model will be compared with pedestrian flow measurements from real world observations. Furthermore, we will evaluate the models by comparing their simulation results against each other.

For this study, we use the vehicle layout as illustrated in Figure 4.6 which has a total length of 42 m and includes 7 equally sized double sliding doors. The area which is reserved for mobility restricted passengers can be used by any passenger. Note that we do not model mobility restricted passengers in this case study. Since we focus on the interactions between passengers and the vehicle design, the platform is modeled as a wide, open and empty area without any waiting passengers or obstacle during alighting simulations. Further, the vehicle is empty before the begin of the boarding process.

In our simulation, passenger movement for boarding and alighting processes is modeled on the operational, tactical and strategic level using the presented simulation framework. We extended the routing model on the tactical level described in Section 4.2.3 in order to represent the task of passengers boarding and alighting vehicles. Complexity arises from modeling the occupation of available seats and standing places realistically. During boarding, a passenger approaching the vehicle will first head towards the nearest door. After entering the vehicle, the passenger has to decide between sitting and standing by searching the vicinity for free seats. The vicinity is vehicle dependent and in our case roughly 5 to 7 m depending on the exact door. If the passenger finds more than one vacant seat, the passenger's final destination is given by the location of the nearest available seat.

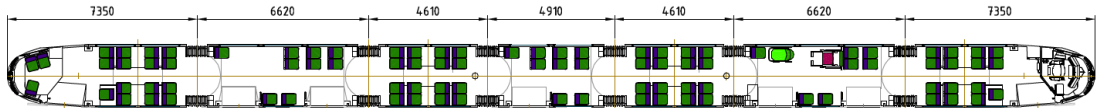


Figure 4.6: Layout of the light rail vehicle used in the first case study. (© Bombardier Transportation)

If there is no free seat available, the location of the final standing spot is defined depending on:

- (a) *Distance to the door*: the same vicinity as previously defined is used, but a passenger prefers standing spots further away from the door in order to provide room for passengers behind to enter the vehicle.
- (b) *Density distribution within the vehicle*: passengers prefer regions which are less occupied than others.
- (c) *Distance to walls, seats and obstacles*: passengers prefer spacious regions to stand instead of narrow passages between seats.

The alighting is somehow simpler, since passengers only move from their seating or standing spot to the nearest door and then onto the platform. For obstacles inside a vehicle such as walls which hinder passengers to move to their final destination on a direct way, we use the routing module described in Section 4.2.3 based on the Theta* algorithm.

On the operational level in order to reach their assigned (intermediate) destination, passengers interact with each other as well as with walls, boundaries and obstacles. The movements and interactions of passengers on the operational level are represented using the extensions from the SF approach SF^B and SF^C as well as the ORCA model. The calibration of the first Social Force implementation SF^B was performed according to Kogler et al. (2014) and of the second Social Force implementation SF^C according to Rudloff et al. (2011b).

Simulation Scenarios

For the simulation, six different scenarios have been defined which vary in passenger load, distribution of passengers on the platform and the process of boarding or alighting (see Table 4.1). We defined two passenger loads according to Bugaricic et al. (1992) and two passenger distributions on the platform:

- *Low Load*: occupation of all available seats plus standing area filled with 2 persons/m².
- *High Load*: occupation of all available seats plus standing area with 6.67 persons/m².
- *Uniform distribution*: all passengers are uniformly distributed on the platform.
- *Non-uniform distribution*: two groups of passengers are placed at the front and rear third of the vehicle leaving the area outside the middle door empty (see Figure 4.6).

The simulation yields trajectories for each individual passenger. Note that all results shown here represent averages of ten simulation runs for statistical analysis. We show the results of our analysis with respect to boarding and alighting times as well as flow rates per percentile. In the following analysis we used the time when 95% of all passengers have boarded or alighted the vehicle by passing the doorsteps, to have stable and comparable values of all operational models investigated.

Passenger Distribution				
Uniform			Non-uniform	
Boarding	Low Load	High Load	Low Load	High Load
Alighting	Low Load	High Load	-	-

Table 4.1: Defined simulation scenarios for boarding and alighting processes.

Model Verification

In order to validate the simulation results of the models used within this case study, we compare them with crowd flow measurements from observations during multiple experiments (Rudloff et al. (2011a)), scientific literature (Harris and Anderson (2007)), where boarding and alighting processes of 30 subway lines worldwide have been investigated, and from real world video data at a public transport station in Vienna. The results in Harris and Anderson (2007) show specific passenger flow rates in a range of 0.18 to 1.77 passengers/m/s for alighting processes, and from 0.37 to 1.58 passengers/m/s for boarding processes. The upper end flow rates occurred in situations where trains have been completely emptied onto a vacant platform and vice versa.

The measured average passenger flow rates, amongst other factors, strongly depend on passenger densities (Rastogi et al. (2013)). Densities during the beginning and end of the boarding, respectively alighting processes are significantly lower than in between. Thus, we considered only the period between 25% and 75% of all passengers have entered, respectively left the vehicle, leaving us with stable flow rates and sufficient densities.

The normalized flow rates in Figure 4.7 demonstrate how well the applied operational models can reproduce the reference data Ref_E from experiments by Rudloff et al. (2011a) and Ref_R from real world observations. Figure 4.7 also shows that a simple linear model with constant flow rates does not sufficiently explain the investigated boarding and alighting processes. For low and high load during alighting the normalized flow rates of all tested approaches are well in line with the reference data.

This is also confirmed by the RMSE as shown in Table 4.2. Except for the low load in SF^C , the deviations between simulation and experimental data, as well as between simulation and real world data are smaller than the deviation between experimental and real world data. As for the boarding scenarios the picture is somehow different: using the low load the RMSE for all tested approaches compared to Ref_E and Ref_R are smaller than the deviation between Ref_E and Ref_R . However, in the high load scenario only SF^B demonstrates that the difference between simulation and observations is within the range of the deviation between experimental and real world data.

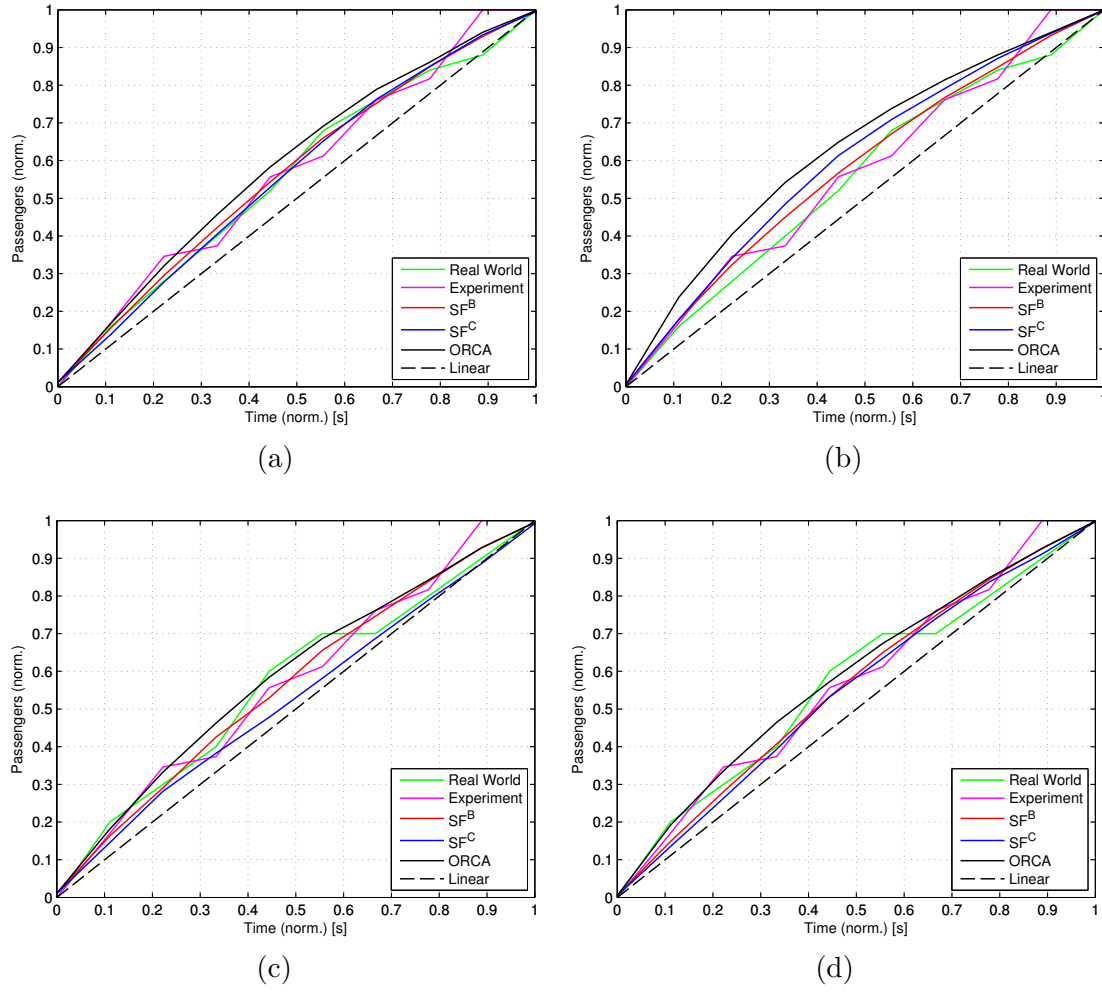


Figure 4.7: Comparison of normalized flow rates between experimental data Ref_E , real world data Ref_R and simulation data from SF^B , SF^C and ORCA during boarding with (a) low load, (b) high load and alighting with (c) low load, (d) high load in the 25% - 75% interval.

Simulation Results

The simulation results for the boarding process are illustrated in Figure 4.8 where the cumulative number of passengers inside the train over time can be seen. Furthermore, the time until 95% of all passengers have entered the train including the variation from 10 simulation runs is shown. While for the low load scenarios (see Figure 4.8a and Figure 4.8c) the time difference until 95% of all passengers are inside the train is within a couple of seconds, there are more significant effects at the high load scenarios (see Figure 4.8b and Figure 4.8d). The ORCA model is not able to move all passengers into the train when simulating the high load scenario. One reason for this is that in areas

	SF ^B		SF ^C		ORCA		Ref _E
	Ref _R	Ref _E	Ref _R	Ref _E	Ref _R	Ref _E	Ref _R
Boarding							
Low Load	0.0209	0.0372	0.0211	0.0381	0.0376	0.0457	0.0510
High Load	0.0315	0.0394	0.0510	0.0571	0.0835	0.0843	0.0510
Alighting							
Low Load	0.0369	0.0380	0.0575	0.0561	0.0350	0.0454	0.0523
High Load	0.0388	0.0376	0.0419	0.0429	0.0367	0.0440	0.0523

Table 4.2: Root-Mean-Square Error (RMSE) for comparing the normalized flow rates between experimental data Ref_E, real world data Ref_R and simulation data from SF^B, SF^C and ORCA. Bold values indicate larger deviation between simulation and experimental/real world data than between experimental and real world data.

behind the doors the ORCA model generates high congestions which as a consequence prohibit other passengers from entering the train.

Figure 4.9 shows the simulation results of the alighting scenarios where the differences are less significant than for the boarding process. Here, mainly the variation in the flow rates as discussed in Section 4.3.1 are reflected again. This results in a bandwidth of a couple of seconds for the time until 95% of all passengers have alighted the train.

In order to investigate temporal aspects of the boarding and alighting processes, the total flows have been split up into 10% intervals (i.e. percentile flows). From the illustration in Figure 4.10 it can be seen that for boarding the results of the SF^C model have the highest percentile flows compared to the other two models. An explanation for this is that the repulsive forces were calibrated according to Rudloff et al. (2011b) where only scenarios with lower densities than in this case study have been considered. The percentile flow rates of the ORCA model during boarding are relatively high at the beginning with a stronger drop in the second half over time. This effect is even more significant for the high load scenarios (Figure 4.10b and Figure 4.10d) where again high congestions at the door areas due to mutual blocking are causing this behavior.

Figure 4.10e shows that the SF^B model has the highest flow rates for alighting with low load and uniform passenger distribution. However, for alighting with high load the ORCA model has the highest flow rate at the beginning while after 40% the flow rates of all models are relatively close (see Figure 4.10f).

This case study demonstrated the importance of the calibration process itself as well as the choice of the operational model for the simulation. While the flow rates for boarding and alighting are similar for all three investigated models, there were significant differences in terms of overall passenger exchange times. The ORCA model showed severe problems to complete the boarding process in scenarios with high passenger load. A reason for this is that the ORCA model cannot compress passenger sizes, which leads to the question if the ORCA model is suitable for such investigations. The framework was shown to be able of discovering weaknesses of the investigated models that would hardly be visible from a mere comparison of some parameters of prediction performance.

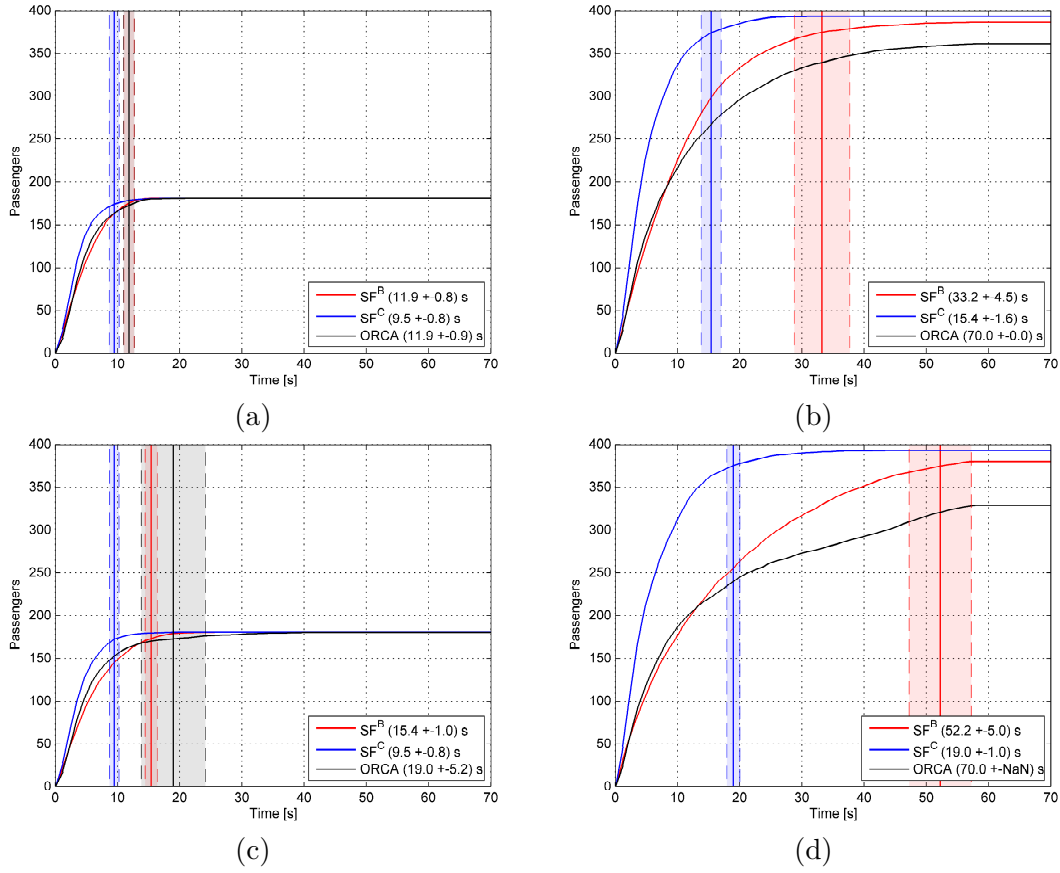


Figure 4.8: Boarding times for 95% of all passengers with (a) low load, uniform distribution, (b) high load, uniform distribution, (c) low load, non-uniform distribution, (c) high load, non-uniform distribution.

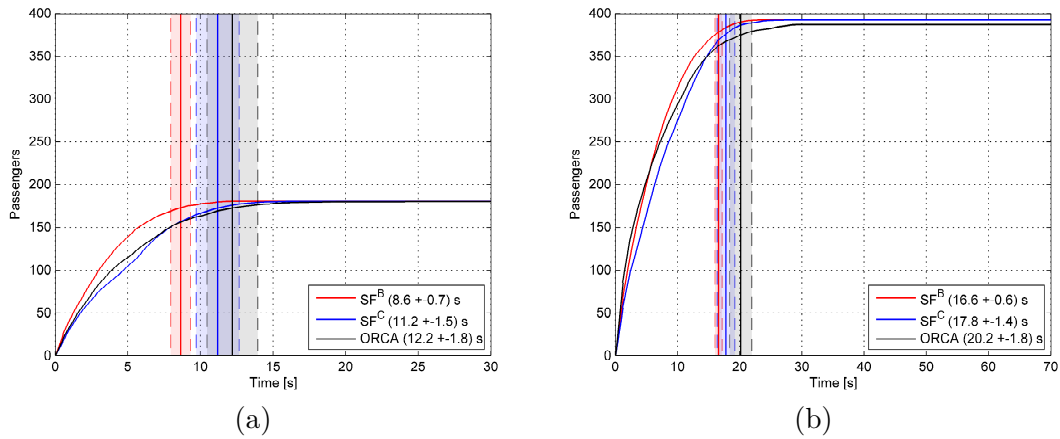


Figure 4.9: Alighting times for 95% of all passengers with (a) low and (b) high load.

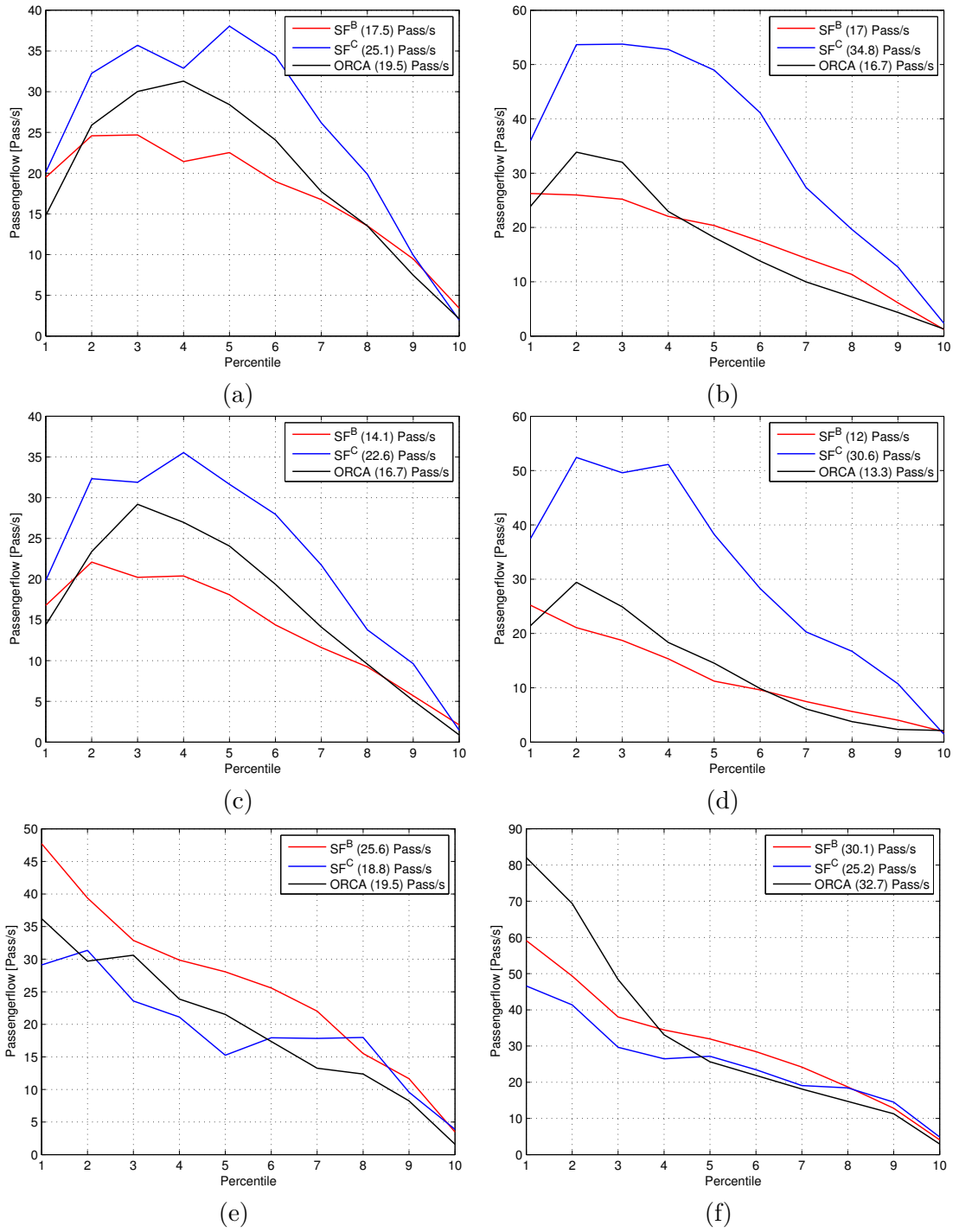


Figure 4.10: Flow rates per percentile during boarding with (a) low load, uniform distribution, (b) high load, uniform distribution, (c) low load, non-uniform distribution, (d) high load, non-uniform distribution and alighting with (e) low load, uniform distribution, (f) high load, uniform distribution.

4.3.2 Passenger Flows in a Complex Subway Station

For the second case study, we used the presented simulation framework to simulate the subway station "Stadion" on the subway line U2 which is located adjacent to the Ernst-Happel Stadium in Vienna (see Figure 4.11). The Ernst-Happel Stadium is the largest football stadium in Austria and can hold up to 50000 visitors with additional 19000 on the pitch for concerts. As illustrated in Figure 4.12, the subway station consists of a lower level that features special event entrances leading to four corridors to enter the station and an upper level which has two platforms with three tracks. After events in the Ernst-Happel Stadium up to 25000 passengers use the specially designed entrance system that also involves an automatic passenger flow control system (see Seer et al. (2008) for details). The automatic passenger flow control system was not used for our case study in this work as it would have impact the generated data.

The main goal of using a simulation within this scenario is to investigate passenger flows on the platform with respect to transport efficiency and safety of the passengers. Key indicators are for instance the total time to transport all passengers, the distribution of passengers to the different corridors, travel times of passengers when moving inside the environment and the number of passengers being on the platform at the same time.

To investigate detailed passenger interactions, we use a microscopic model for simulating the passenger movement on the upper level. In advance it is not obvious which granularity for modeling the lower level is necessary in order to accurately examine the described indicators on the upper level. Since the basic scenario already involves 25000 passengers and we have to simulate multiple scenarios with varying demand, computational performance is crucial. Thus, it seems reasonable to use a macroscopic model on the lower level which can calculate simulation results faster but with lower granularity.

We use our simulation framework to compare the output of the described scenarios which are derived when applying a microscopic or a macroscopic model on the lower level. In both cases the microscopic modeling approach is used on the upper level. For the microscopic model we use the SF^B approach in our simulation framework as described



Figure 4.11: Viennese subway station "Stadion" (a) with the Ernst-Happel Stadium in the back and (b) crowd in front of the entrances after an event. (© Wiener Linien)

in Chapter 3. The calibration of the implemented SF^B model was performed according to Rudloff et al. (2014). In the case of applying the macroscopic model on the lower level, we use the implementation of the macroscopic model as shown in Section 4.2.4. On the tactical level we use the dynamic routing model described in Section 4.2.3. For the macroscopic model, however, the dynamic routing is restricted since pedestrians can only decide at each node point of the graph for a certain route. In addition to the *Operational module*, we use a *Generator Module*, a *Tactical Module*, and a *Visualization & Analysis Module* in order to derive the simulation results for this case study.

Simulation Scenarios

In this case study we simulate a scenario when after events in the Ernst-Happel Stadium nearby, one platform is active for transporting passengers towards the city center with alternating trains on the tracks at both sides of this platform (see Figure 4.12a). The other platform is used by passengers heading outbound where only one track is frequented by trains. Furthermore, arriving passengers alighting the trains are not included within the simulation.

The concept of the passenger flow control system builds up on a special architectural design of the station which comprises four corridors as illustrated in Figure 4.12b. Each of them provides access to the platforms on the upper level via a staircase. The entrance to each corridor are two sliding doors, with an adjustable width. Note that in this work we keep all sliding doors at a constant width of 1.80 m during all simulations, thus not using the automatic passenger flow control feature of the station. Between the sliding doors and the open space outside the station are in total 15 meanders with each of them having a width of one walking lane (i.e. 60 cm). To restrict the maximum pedestrian inflow only eight meanders are open (two meanders per assigned corridor).

The environment of this scenario consists of two sections, i.e. the lower and upper level, whereas all pedestrians have their starting location (where they are created by the generator module) along a virtual line in the lower right of the ground floor (see blue line in Figure 4.12b). The simulation is performed with 12500 and 25000 pedestrians which are generated within one hour. Generation is not uniform during this time but has the highest rates between minute 10 and 50 to accommodate when the main bulk of people is arriving from the nearby stadium. 80% of passengers are heading towards the city center and the remaining 20% traveling out of town. Pedestrians move to the platform according to their individually assigned destination where they eventually board a train and will then be removed from the simulation (see Figure 4.12a). The trains to the city center arrive with an interval of 150 s and for the outbound direction with 180 s. Each train arrives empty and provides a capacity of 800 persons. While moving onto the platform pedestrians have to pass certain facilities (for a detailed description see Section 4.2.4), which in this scenario are meanders, doors, staircases and trains.

For the results on the computational performance in Section 4.3.2 we use a basic scenario with 25000 pedestrians and deviating scenarios with increasing and decreasing number of pedestrians. Note that we keep the ratio of passenger flows moving towards the city center and outbound unchanged.

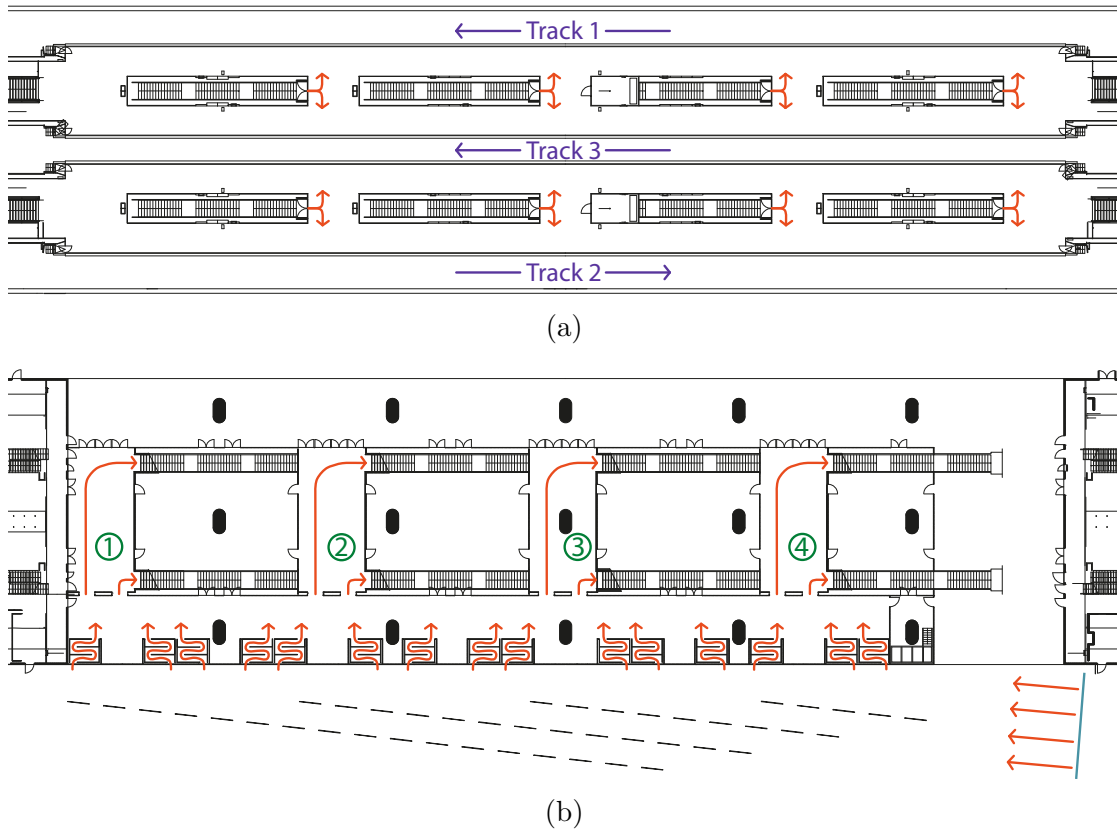


Figure 4.12: CAD drawing of the subway station "Stadion" showing (a) the two platforms and three tracks (driving direction of trains shown in purple) on the upper level and (b) the entrances with four corridors (corridor numbers shown in green) on the lower level. The two levels are connected via staircases (four at each platform). Pedestrians are generated in the simulation at the blue line and orange arrows denote the possible walking paths.

Simulation Results

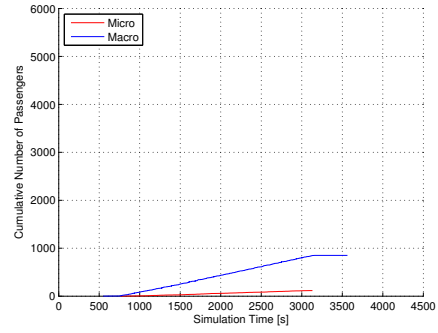
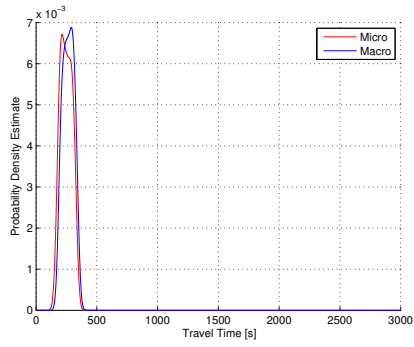
The simulation includes passenger movement from outside of the subway station onto the platforms where passengers either board a train towards the city center or in the outbound direction. In the following analysis we only discuss the simulation results of passengers moving on the platform where trains depart towards the city center (see Figure 4.12a).

One of the indicators for evaluating the differences between using a microscopic or macroscopic simulation model in the given case study is the total time to transport all passengers. Hence, such travel times can be investigated per corridor and as their total sum. For the scenario with 12500 passengers, the distribution of travel times per corridor is illustrated in the left column of Figure 4.13. The results do not indicate any significant

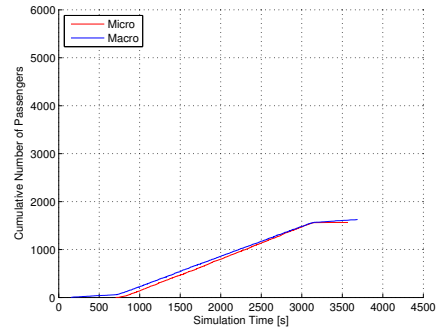
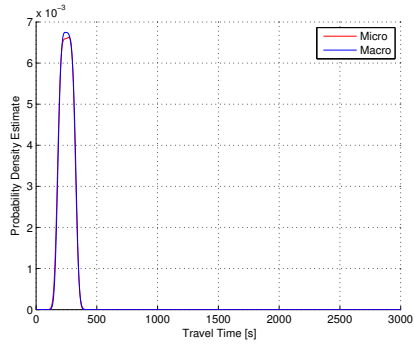
difference between the two operational models. A similar behavior is evident in the total sum of all corridors shown in Figure 4.15. For the scenario with 25000 passengers the distribution of travel times per corridor is considerably different when comparing the microscopic and macroscopic simulation. As illustrated in the left column of Figure 4.14 the microscopic model has a higher concentration in the range between 250 and 500 s. For corridor 4 the distribution is broader which might be due to some passengers can bypass from the side and hence overtake already waiting persons in front of a meander. When applying the macroscopic model the travel times are more equally distributed with no passengers taking over 1200 s to reach their destination. This effect occurs for all corridors and can also be seen in the total sum of all corridors in Figure 4.15. Furthermore, two modes can be found in the distribution which become more dominant for the corridors closer to the starting position of the persons, i.e. corridor 3 and 4. The left mode appears to originate from periods with smaller rates of passenger flow to the station (e.g. the first minutes after starting the simulation) while the right one seems to be a result of passenger movement during saturation (i.e. times when passengers are waiting in front of all meanders). For corridors 1 and 2 the left mode in the walking time distribution is less apparent which could be explained by passengers selecting these corridors at a later time when flow rates from pedestrian generation are increased.

Another aspect is the cumulative number of pedestrians per corridor and as their total sum. The right columns of Figure 4.13 and Figure 4.14 show the results for the scenario with 12500 and 25000 passengers, respectively. The cumulative number of pedestrians varies for each corridor and between the two operational models. Due to the longer walking path to corridor 1, the increase in passenger numbers for this corridor starts significantly later. While passenger demand within the macroscopic model is higher for corridor 1 and 2 compared to the microscopic model, this is the other way around for corridor 4. This could be explained by the different routing methods applied to the microscopic and macroscopic model. However, as shown in Figure 4.15 the cumulative number of passengers as a sum over all corridors for both scenarios does not reveal any significant differences between the simulation results of the microscopic and the macroscopic model.

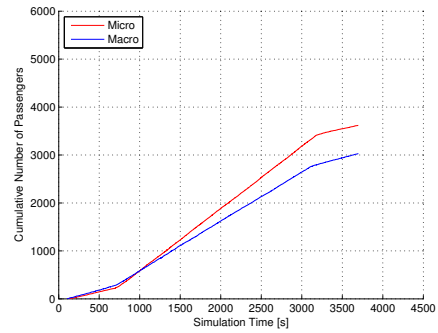
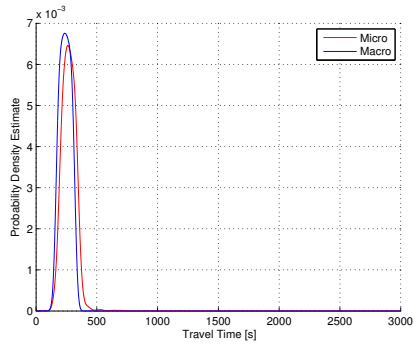
The evaluation for the number of passengers being on the platform at the same time can be derived from the results shown in Figure 4.16. In both simulation runs the peak characteristics are primarily set by the train interval. Although the amplitude of the peaks differs between the two approaches no further significant effects such as overcrowding on the platform can be observed.



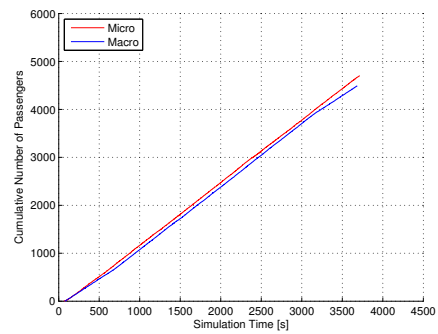
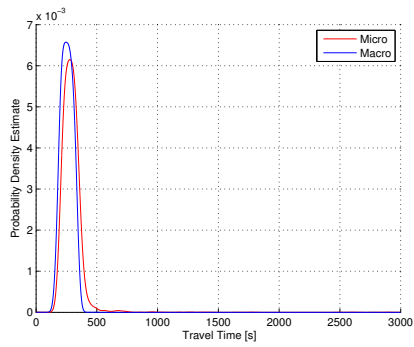
Corridor 1



Corridor 2

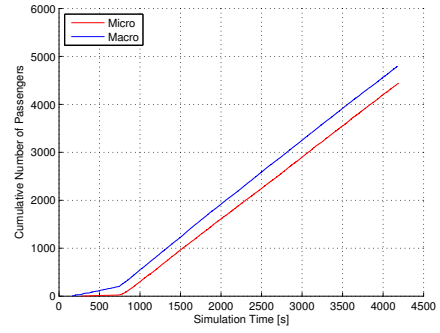
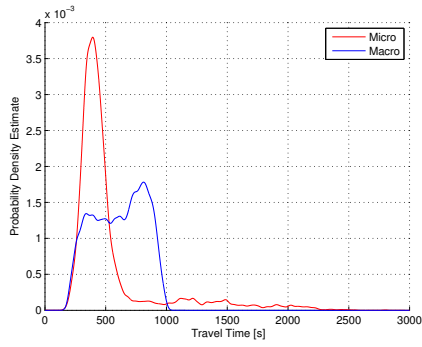


Corridor 3

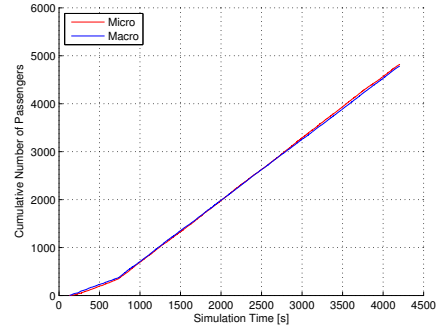
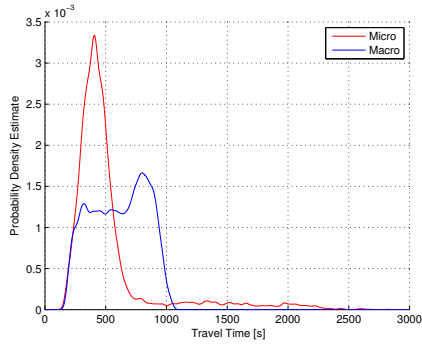


Corridor 4

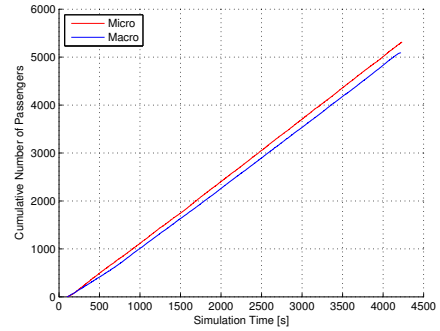
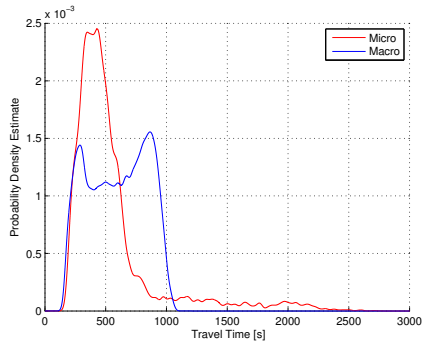
Figure 4.13: Estimated probability distribution function of travel times (left) and the cumulative number of passengers (right) per corridor with 12500 passengers.



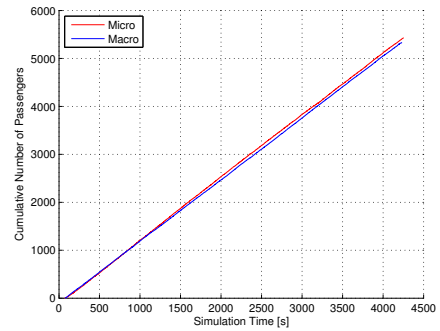
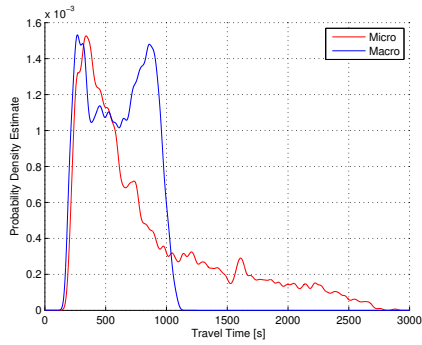
Corridor 1



Corridor 2



Corridor 3



Corridor 4

Figure 4.14: Estimated probability distribution function of travel times (left) and the cumulative number of passengers (right) per corridor with 25000 passengers.

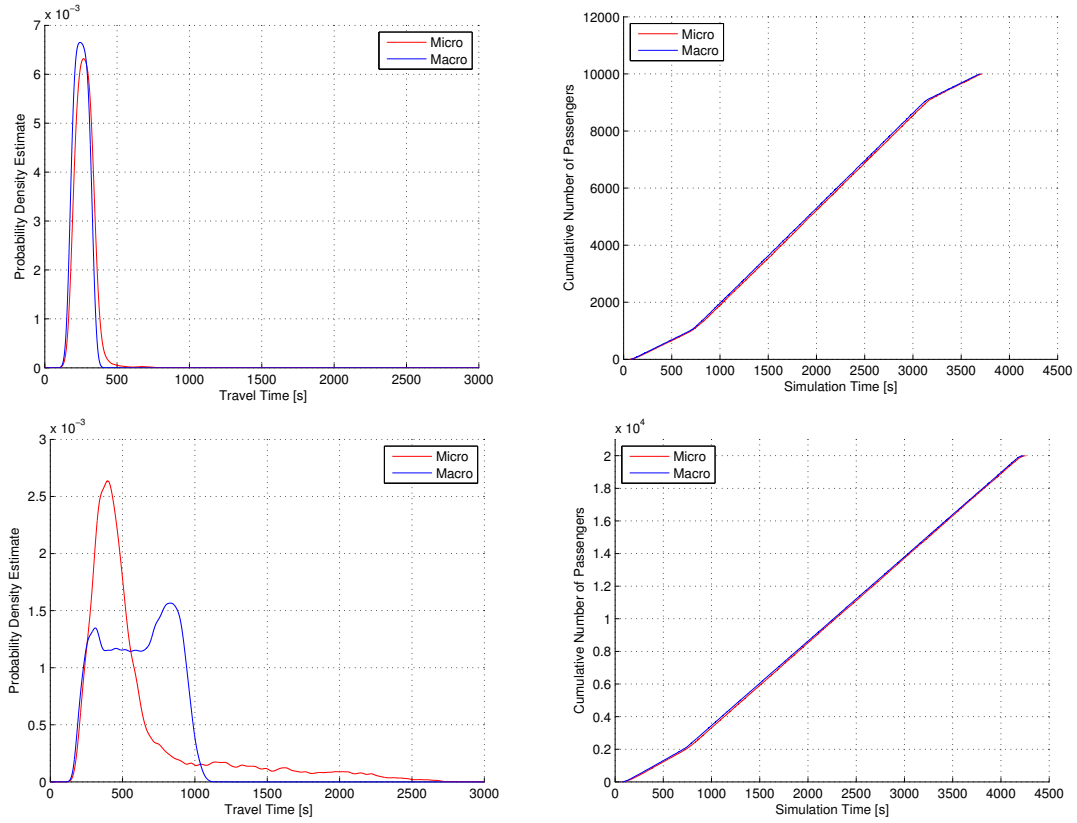


Figure 4.15: Estimated probability distribution function of travel times (left) and the cumulative number of passengers (right) per corridor with 12500 passengers (top row) and 25000 passengers (bottom row).

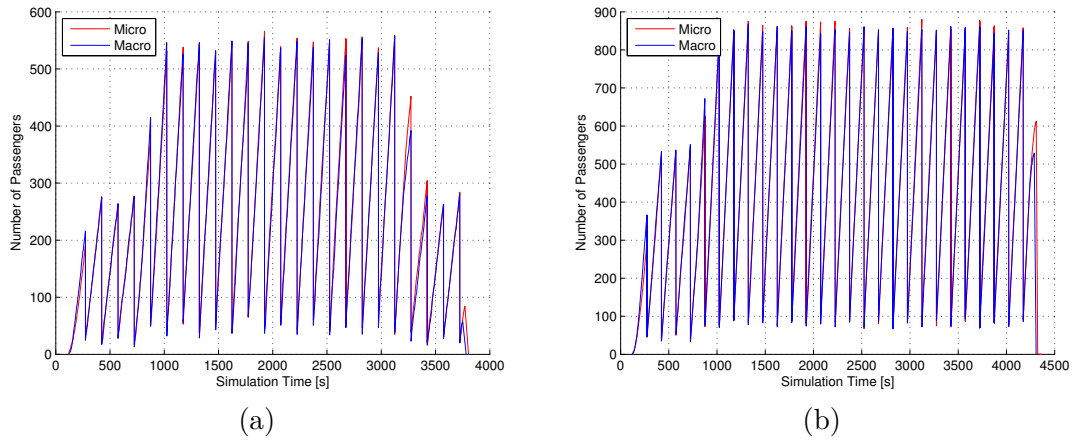


Figure 4.16: Number of simulated passengers being simultaneously on the platform with (a) 12500 passengers and (b) 25000 passengers.

The results for the computational performance, in particular the scalability for a growing amount of pedestrians in the simulation, can be seen in Figure 4.17. As expected, the total execution time grows with the number of pedestrians. Figure 4.17a and c show the total simulation time, which is relatively similar for both applied simulation approaches. This confirms the findings discussed before (see Figure 4.15) also for different numbers of passengers within the simulation. The execution time of the microscopic model has a much stronger increase over the number of passengers (see Figure 4.17a) compared to the execution time of the macroscopic model (see Figure 4.17c). Furthermore, the total execution time when applying the macroscopic model is always lower than the simulation time within the simulated range of pedestrian amount. This shows that in this setting the simulation can be calculated faster than real time. The microscopic model reveals a more rapid increase of the total execution time and after 20000 passengers the simulation performs slower than in real time. Figure 4.17b and c provide more details on the individual execution time for each used model.

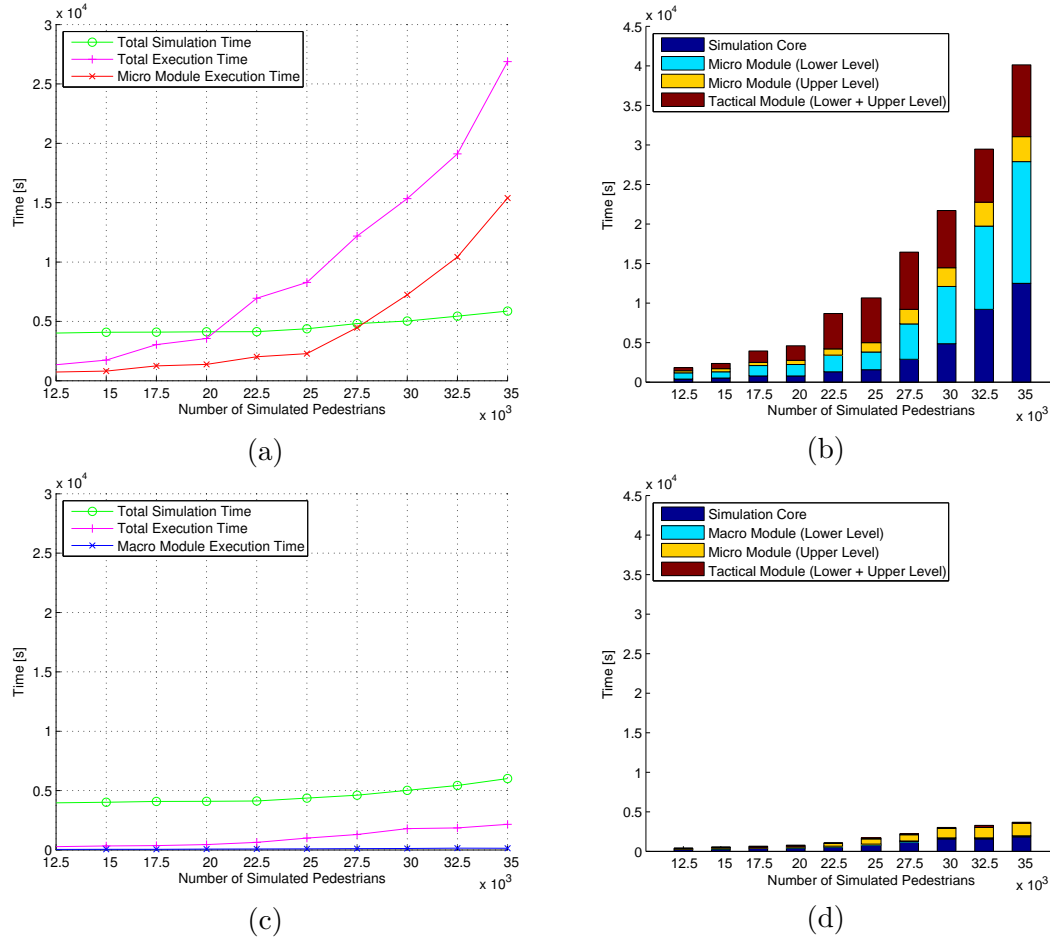


Figure 4.17: Computational performance for including the microscopic model (a) in total and (b) per module and the macroscopic model (c) in total and (d) per module.

4.4 Summary

In this chapter we have presented our framework for pedestrian simulations. Our goal was to design a framework that can integrate various simulation models on the three levels of decision making, i.e. strategic, tactical and operational, and provides the possibility of easily switching or combining different models. The flexibility of the framework was demonstrated in two real world case studies.

In the first case study, passenger flows were simulated during boarding and alighting of a light vehicle train using three different operational models, i.e. the Social Force approaches SF^B and SF^C , and the ORCA model. Simulating the same scenario with different models revealed that the derived overall passenger exchange times varied significantly between the models.

In the second case study, two operational models with varying granularity, that is microscopic (using the SF^B model) and macroscopic (using a graph-based approach), were used for simulating passenger flows in a complex subway station. The results showed that the computational time can be reduced to one third when using the macroscopic instead of the microscopic model. At the same time, examining certain parameters such as the cumulative number of persons transported away or the maximal number of persons on the platform provided almost identical results with the macroscopic model. However, for other parameters, such as route-choice, the choice of the model for simulation has significant impact on the results.

All model approaches described in Chapter 3 are implemented and integrated into the simulation framework. Our simulation framework is the optimal basis for structured investigations on strengths and weaknesses of various microscopic pedestrian movement simulation models, which will be pursued in the remainder of this thesis. In Chapter 5 we will present different calibration and validation strategies for Social Force based modeling approaches. We will then extend these procedures by defining a generalized calibration and validation strategy in Chapter 6 in order to evaluate all modeling approaches that are part of this study.

Calibration Procedures for Social-Force Models

In order to develop a model that is able to represent realistic movement behavior one has to perform model calibration and a validation of the results. Therefore, observations of real pedestrians are needed which can be obtained from (controlled) experiments (Daamen and Hoogendoorn (2012)) or from real-world measurements. Quantitative data from human movement observations can comprise, for instance, travel times, flow rates, speed-density fundamental relation or even trajectories of individual pedestrians. The process of collecting individual trajectories to calibrate microscopic models is cumbersome since robust (including all individuals being in a scene at the same time), accurate (within a few centimeters) and comprehensive (minimum of several 100 individuals) trajectories from various scenarios (e.g. different pedestrian densities) are needed. To meet these high standards, we use trajectories which were collected from our approach based on the Microsoft Kinect as described in Section 2.3.

Several calibration procedures for microscopic pedestrian simulation models based on individual trajectory data were suggested in the literature, where in particular two distinct approaches are predominant: the first is *model estimation by nonlinear least square methods* (e.g. Hoogendoorn et al. (2007) or Ko et al. (2013)). However, as shown in Rudloff et al. (2011b) this method has several drawbacks due to the large measurement errors from data collection using pure video data. For instance, using the acceleration instead of the spatial position introduces significant noise due to the second derivative. Furthermore, this might lead to error-in-variables problems and parameter estimates possibly result in a bias towards zero. The second approach involves the *comparison of real and simulated trajectories* (e.g. Moussaïd et al. (2009), Rudloff et al. (2011b)) and hence is time consuming as a complete simulation run is needed during each optimization step. Both calibration approaches have been applied in this work and their individual methodologies and results for the SF^A , SF^B and SF^C model are presented in the following subsections.

5.1 Model Parameter Estimation with Non-linear Regression

Since the quality of the trajectories from the tracking approach developed in this work is significantly higher compared with those automatically extracted from video footage (see Section 2.2), it needs to be determined if the added data quality makes a nonlinear least square estimation feasible. Many of the available force-based models are calibrated on observed human movement data (e.g. Campanella et al. (2014)). However, validation for investigating the model characteristics, e.g. variance in parameter values, is still sparse. It needs to be determined if the estimated parameters can explain the diverse behavior of pedestrians or if parameters need to be more flexible and differ for different pedestrians. This would suggest that a Social Force model with a single parameter set might not be able to explain pedestrian behavior in different situations for example with respect to different densities.

We present a methodology for validating Social Force based models by investigating the reproducibility of human movement behavior on the individual trajectory level for different settings with real-world movement data (Seer et al. (2014b))¹. Our approach estimates model parameter values and their distribution with non-linear regression on observed trajectory data, where the resulting variances of the parameter values represent the model's validity. This approach is demonstrated on a comprehensive (235 pedestrians) and highly accurate (within a few centimeters) set of human movement trajectories obtained from real-world pedestrian traffic with bidirectional flow as shown in Section 2.3. We validate the Social Force model SF^A , SF^B and SF^C which are described in Chapter 3. For reducing the complexity of calibration, the repulsive force from static obstacles $\mathbf{f}_{\alpha i}$ is modeled by using the functional form as given by SF^B for all models in this section.

5.1.1 Measures for Human Movement

For model calibration and validation, we use a set of N resampled trajectories

$$\mathcal{T} = \left\{ [t_\alpha \ x_\alpha \ y_\alpha]^T \right\}_{\alpha \in N} \quad (5.1)$$

as defined in (2.5). As described in Chapter 2, the trajectory of a pedestrian α is composed of a vector of timestamps t_α and 2D positions $\mathbf{x}_\alpha = [x_\alpha \ y_\alpha]^T$. The data points of the resampled trajectory are at a regular time interval $\Delta t = 0.1$ seconds. The corresponding x_α and y_α at regular time intervals t_α are results from the cubic spline approximation (see De Boor (2001)) with a smoothing parameter $p = 0.98$.

Figure 5.1a illustrates the automatically obtained trajectories from a walking experiment with a single centralized obstacle in the scene. This walking experiment was performed under real world conditions, meaning that the individuals traversing MIT's Infinite Corridor had no information about being observed. The red and blue trajectories

¹The work in this section was published by S. Seer, C. Rudloff, T. Matyus and N. Brändle, "Validating Social Force Based Models with Comprehensive Real World Motion Data", In: Transportation Research Procedia, Volume 2, pp. 724-732, ISSN 2352-1465, 2014.

in Figure 5.1a represent the two walking lanes in opposite directions which people form most of the time. Figure 5.1b shows the trajectory density map using a kernel density estimation with a normal kernel function and a bandwidth of 0.1 m. This reveals the main paths located on both sides of the corridor which pedestrians use to evade from the centralized obstacle.

From the trajectories one can directly extract the acceleration $\tilde{\mathbf{f}}_\alpha(t)$ for each individual α at each time instance t from the collected trajectories according to

$$\begin{aligned}\tilde{\mathbf{f}}_\alpha(t) &:= [\tilde{f}_\alpha^x(t), \tilde{f}_\alpha^y(t)] \\ &= \left[\frac{(x_\alpha(t+1) - x_\alpha(t)) - (x_\alpha(t) - x_\alpha(t-1))}{\Delta t^2}, \frac{(y_\alpha(t+1) - y_\alpha(t)) - (y_\alpha(t) - y_\alpha(t-1))}{\Delta t^2} \right].\end{aligned}\quad (5.2)$$

Figure 5.1c shows the time averaged accelerations inside the scanning area. As expected the accelerations are higher the nearer pedestrians pass the central obstacle. Besides, in the lower right and in the upper left part of the figure, the areas where people start to deviate can be identified. We derive the position and the desired goal for a pedestrian α from the first point at time t_α^{in} and the last point at t_α^{out} of the associated observed trajectory \mathcal{T}_α . The desired velocity v_α^0 of pedestrian α is defined as the 95th percentile of the observed velocities. The magnitude of the current velocity vector \mathbf{v}_α is set equal to v_α^0 , and it directs towards the pedestrian's desired goal. Furthermore, we set for each simulated pedestrian $\tau = 0.5$.

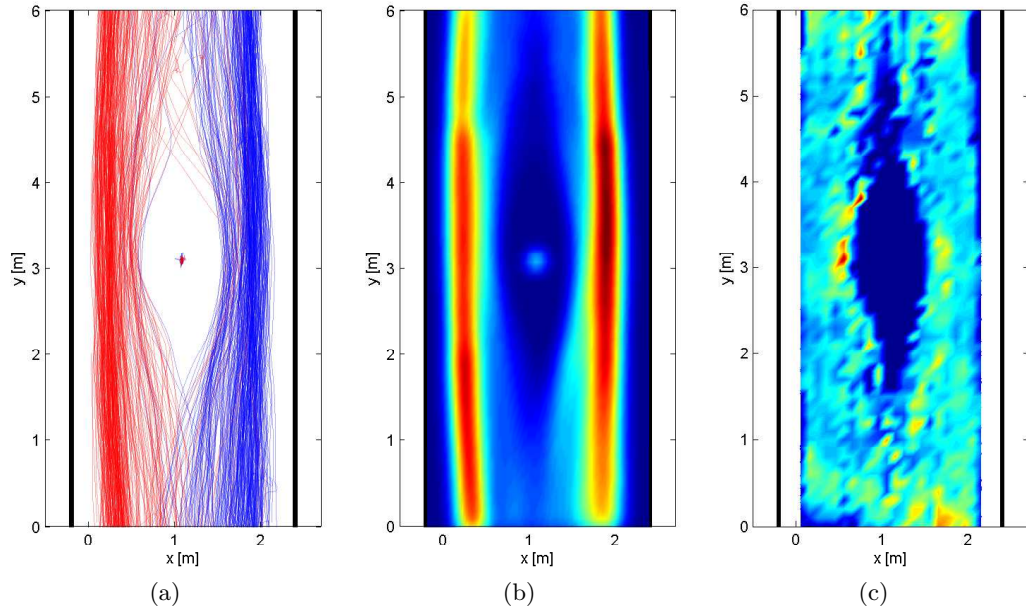


Figure 5.1: Observed (a) trajectories with walking directions encoded in red and blue, (b) density map and (c) acceleration map based on real-world observations in a corridor with a single centralized obstacle.

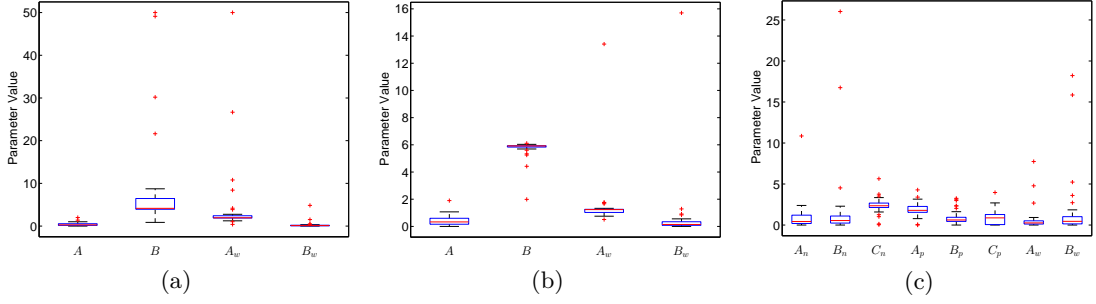


Figure 5.2: Boxplots with estimated parameter values from personalized calibration for (a) SF^A, (b) SF^B and (c) SF^C.

Since only a section of the corridor was observed, it has to be guaranteed that all individuals influencing each others' movements (i.e. persons closer than 2 m in front or 1 m behind) are present in the scene. We selected a subset of trajectories \mathcal{T}^S corresponding to a set of pedestrians M , where M is a subset of N , that fulfills two constraints: 1) they are long enough, i.e. start below $y = 1$ m and end above $y = 4$ m and vice versa without stops, and 2) all other individuals who are present or appear during the time span of the relevant trajectory have to be present for the whole time span or until they leave the scene. For the subsequent calibration, we only use segments of trajectories in \mathcal{T}^S , which in upward direction are between $y = 1$ m and $y = 4$ m and between $y = 5$ m and $y = 2$ m for the downward direction (see Figure 5.1). Hence, we denote the start and end time of the segments by t_α^{start} and t_α^{end} .

5.1.2 Model Estimation and Validation Results

As a first step, we examine the validity of estimating the parameters of the investigated Social Force models using non-linear least square estimation. In the estimation procedure we use the objective function

$$f_{obj}(\theta) = \sum_{\alpha \in M} \sum_{t=t_\alpha^{start}}^{t_\alpha^{end}} \left(\left(\tilde{f}_\alpha^x(t) - f_\alpha^x(t, \theta) \right)^2 + \left(\tilde{f}_\alpha^y(t) - f_\alpha^y(t, \theta) \right)^2 \right), \quad (5.3)$$

where $\mathbf{f}_\alpha(t, \theta) = [f_\alpha^x(t, \theta), f_\alpha^y(t, \theta)]$ is the acceleration at time t given a parameter set θ . The optimization uses the gradient based method `fmincon` in MATLAB. This method also allows to extract the Hessian matrix H_f of f_{obj} at the estimated optimal parameter set $\hat{\theta}$, which in turn gives an estimate of the covariance matrix of the parameters as $Cov(\hat{\theta}) = H_f^{-1}$. Using $f_{obj}(\theta)$ the three Social Force models are calibrated in two ways: by estimating the parameters for all pedestrians at once (*general calibration*) and by estimating them for the first 33 pedestrians (*personalized calibration*) in order to examine if the models transfer well to single pedestrians. The results of the parameter estimation for all three models can be seen in Table 5.1.

The results show that the objective function is best for SF^C and that SF^A with the original circular formulation outperforms SF^B with the elliptical form. Despite the large

number of data points (7799 from 235 trajectories) the parameters estimated in the general calibration are not all significant, which suggests either that the information contained in the data is not sufficient or that there is a strong variation in behavior between different pedestrians. It can be seen from Table 5.1 that the parameters of the personalized calibration are higher on average than the parameters of the general calibration and their standard deviations are rather large. Figure 5.2 shows that all these parameters lie in a relatively small band and that there are only a few outliers. This, together with the plots in Figure 5.3, suggest that some pedestrians react much stronger than others to obstacles. Furthermore, the accelerations from the parameter set estimated by the general calibration do not suffice to model this strong reaction.

In order to test if the results from the non-linear least square estimation in a model reproduce good reaction to other pedestrians, it is important to investigate the collision avoidance behavior of the model. As an example, we show in Figure 5.4 the accelerations in x and y directions resulting from the three models with parameters from general calibration. In this setting a pedestrian is walking with a velocity of $[0, 1]$ towards a goal upwards in y -direction while another pedestrian stands at position $[1.1, 3]$. The accelerations resulting from the model are calculated for all positions in a 2D regular grid with grid size 0.1 m. One can see that all models show collision avoidance behavior. Due to model restrictions SF^A and SF^B do not show much acceleration to the side when a pedestrian is walking towards an obstacle straight ahead, but rather just decelerates the pedestrian. In comparison SF^C does show avoidance behavior in that case. Overall, the models show a promising behavior, however, a calibration should be performed on denser scenarios to ensure that the collision avoidance works in those cases as well.

Table 5.1: Estimated parameter values for the three models with standard deviations of the parameters in brackets. Parameters significantly different from zero are in bold letters.

Model	Value of f_{obj} General Calibration	Avg. value of f_{obj} and (std) Personalized Calibration	Parameter	Parameter Value and (std) General Calibration	Avg. Parameter Value and (std) Personalized Calibration
SF^A	2189.4	7.0374 (5.1200)	a_p	0.1634 (0.0104)	0.4500 (0.4050)
			b_p	4.1554 (0.6535)	13.4651 (18.3852)
			a_o	1.9534 (1.2244)	8.8260 (15.4703)
			b_o	0.1090 (0.0231)	0.2882 (0.7676)
SF^B	2244.4	7.9460 (5.7311)	a_p	0.1845 (0.0205)	0.4213 (0.3941)
			b_p	5.9334 (1.6812)	5.7032 (0.7336)
			a_o	1.9534 (0.6035)	1.5540 (2.1782)
			b_o	0.1366 (0.0248)	0.7415 (2.7448)
SF^C	1925.2	6.1492, (3.8987)	a_d	0.2615 (0.0551)	1.0310 (1.9060)
			b_d	0.4026 (0.1238)	2.0385 (5.2833)
			c_d	2.1614 (0.3728)	2.3522 (0.9944)
			a_e	1.5375 (0.3084)	1.8980 (0.8775)
			b_e	0.4938 (0.1041)	0.9656 (0.9226)
			c_e	0.5710 (0.1409)	0.9190 (0.8823)
			a_o	0.3280 (0.1481)	0.7450 (1.5747)
			b_o	0.1871 (0.0563)	1.8044 (4.1646)

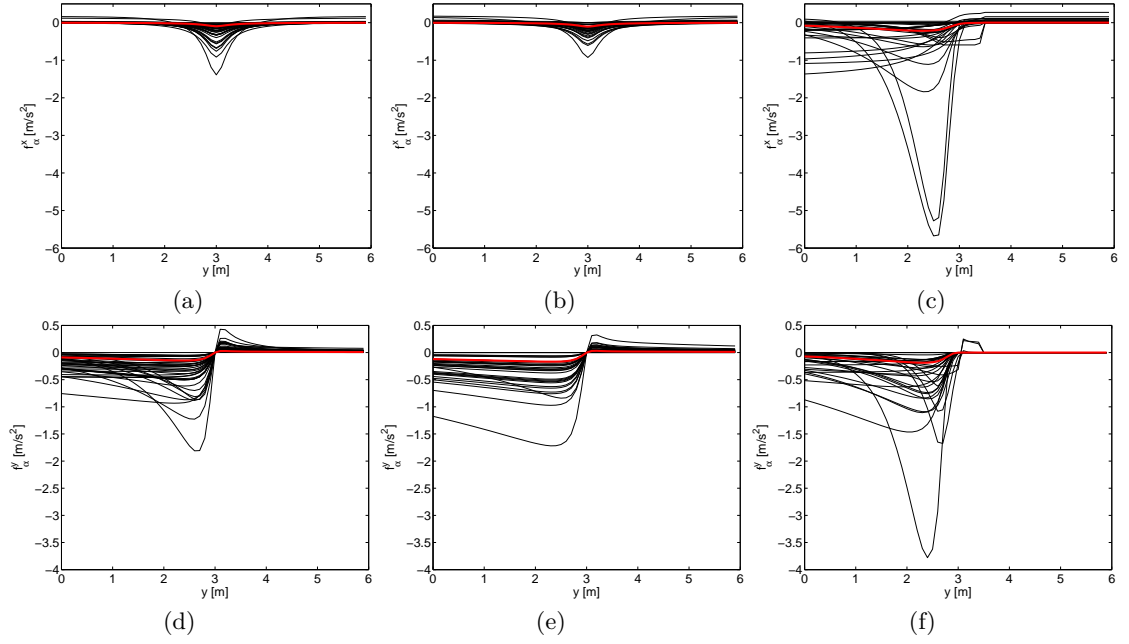


Figure 5.3: Accelerations calculated with SF^A (left), SF^B (middle) and SF^C (right) in x -direction (a, b and c) and y -direction (d, e and f) for parameters from personalized (black lines) and general calibration (bold red line).

It was noted in Rudloff et al. (2014) that Social Force models have relatively large parameter areas where they behave very similarly with respect to closeness of trajectories. However, the validation results in Figure 5.3 show that the different parameter sets from personalized calibration (see Figure 5.2) produce significant variations in the behavior of accelerations in x and y -directions. In particular there are some outliers in the acceleration behavior which result from the fact that for some pedestrians the parameters from personalized calibration are much larger than for the general calibration using the points from all trajectories.

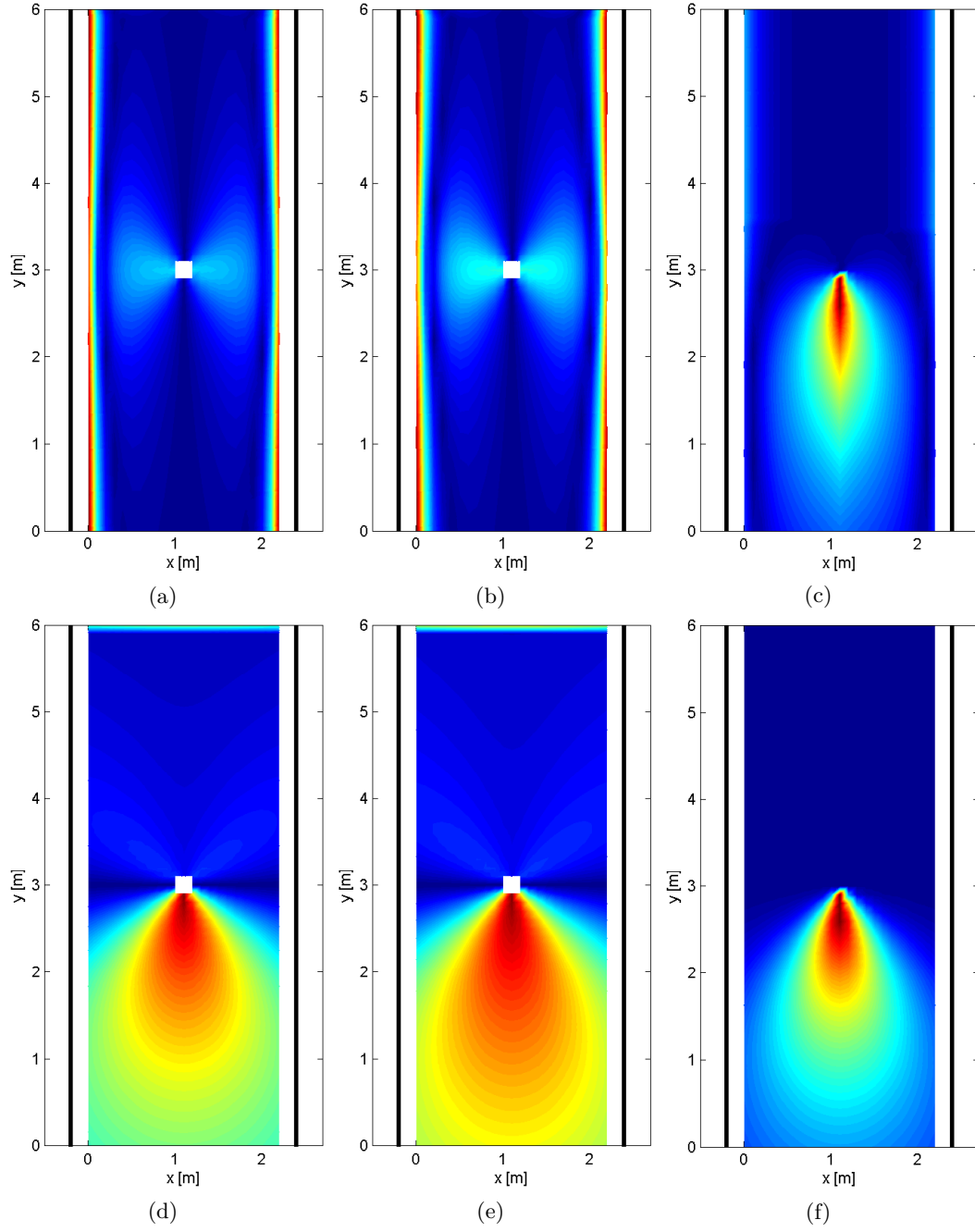


Figure 5.4: Accelerations in x-direction (a, b and c) and y-direction (d, e and f) calculated using SF^A (left), SF^B (middle) and SF^C (right) with parameters from general calibration.

5.2 Simulation-based Model Parameter Estimation

The process of model calibration involves the identification of parameter values which reproduce observed pedestrian behavior in the simulation results. We estimated values for the different parameters in the three model approaches SF^A , SF^B and SF^C based on our empirical data set from the walking experiments (Seer et al. (2014a))².

	Number of trajectories	
	Experiment 1	Experiment 2
Calibration Set	516	1346
Validation Set	169	643
Total	685	1989

Table 5.2: Partitioning of the trajectory data set for model calibration and validation.

5.2.1 Calibration Procedure

In this section we use a technique for calibrating microscopic simulation models which is based on a simulation approach inspired by Johansson et al. (2007), where each pedestrian is simulated separately while keeping the remaining pedestrians on their observed trajectory. Each simulation run is performed according to the following procedure: the position and the desired goal for a simulated pedestrian α are extracted from the start point at time t_α^{in} and the end point at t_α^{out} of the associated observed trajectory \mathcal{T}_α . The desired velocity v_α^0 of pedestrian α is defined as the 90th percentile of the observed velocities. The magnitude of the current velocity vector \mathbf{v}_α is set equal to v_α^0 , and it directs towards the pedestrian's desired goal. Pedestrian α is simulated for $M_\alpha = |\mathcal{T}_\alpha|$ timesteps during time t , with $t_\alpha^{in} \leq t \leq t_\alpha^{out}$, where both bounds are again derived from the observed trajectory. Note that we set for each simulated pedestrian $r = 0.2$ and $\tau = 0.5$. It is left for future research to extract the actual radius of a pedestrian from the measured Kinect data.

After having simulated a set of N pedestrians from the calibration data set with the above procedure, the similarity measure s for testing the fit of our simulated trajectories is computed as

$$s = \frac{1}{N} \sum_{\alpha=1}^N \left(\frac{d(\alpha)}{t_\alpha^{out} - t_\alpha^{in}} + g(\alpha) \right). \quad (5.4)$$

²The work in this section was published by S. Seer, N. Brändle and C. Ratti, "Kinects and Human Kinetics: A New Approach for Studying Pedestrian Behavior", In: Transportation Research Part C: Emerging Technologies, DOI: 10.1016/j.trc.2014.08.012, pp. 212-228, 2014.

For a pedestrian α , the mean Euclidean distance

$$d(\alpha) = d(\mathcal{T}_\alpha, \mathcal{T}_\alpha^S) = \frac{1}{M_\alpha} \sum_{i=1}^{M_\alpha} \|\mathbf{x}_{\alpha_i} - \mathbf{x}_{\alpha_i}^S\| \quad (5.5)$$

provides the dissimilarity between positions $\mathbf{x}_{\alpha_i} = [t_{\alpha_i}, x_{\alpha_i}, y_{\alpha_i}]^T$ of the observed trajectory \mathcal{T}_α and positions $\mathbf{x}_{\alpha_i}^S = [t_{\alpha_i}^S, x_{\alpha_i}^S, y_{\alpha_i}^S]^T$ of the simulated trajectory \mathcal{T}_α^S . Furthermore, the length of trajectories is defined by $|\mathcal{T}_\alpha| = |\mathcal{T}_\alpha^S| = M_\alpha$. Since none of the used models explicitly restricts overlapping between pedestrians, an overlap penalty is added with

$$g(\alpha) = \frac{1}{N-1} \sum_{\beta \neq \alpha} \max_t \left(0, \frac{1}{\|\mathbf{d}_{\alpha\beta}(t)\|} - \frac{1}{r_\alpha + r_\beta} \right). \quad (5.6)$$

Model parameter values are estimated by applying an optimization algorithm to find the best possible fit by minimizing the objective function (5.4). We use a genetic algorithm which does not suffer from a starting value problem to find the neighborhood of the global minimum of (5.4). The estimated parameter values obtained by the genetic algorithm are then used as initial values for the Nelder-Mead algorithm (see Lagarias et al. (1998)) to refine the result. This hybrid approach allows finding the global minimum while being numerically efficient.

5.2.2 Validation Results

We validated the SF^A , SF^B and SF^C model in two different ways: first, by estimating the dissimilarity between observed and simulated trajectories, and second, by comparing the walking time distribution from the simulation with observations using a statistical test.

Validation Based On Trajectory Similarity

The results for the parameter fit of the individual models are provided in Table 5.3 as s_{cal} for the calibration data set and s_{val} for the validation data set. The best possible value for (5.4) is $s = 0$. For both experiments, the best fit of the objective function with the compared modeling approaches could be achieved using the repulsive formulation from SF^C defined in (3.5).

	Experiment 1			Experiment 2		
	SF^A	SF^B	SF^C	SF^A	SF^B	SF^C
s_{cal}	0.1256	0.1105	0.0843	0.1721	0.1717	0.1630
s_{val}	0.0963	0.0823	0.0671	0.0967	0.0912	0.0883

Table 5.3: Fit of the parameter values for three different Social Force formulations based on calibration and validation data set.

By applying the three Social Force models on only a small subset of our validation data set, their basic ability of representing pedestrian behavior can be evaluated in a qualitative manner. Figure 5.5 shows the results of a simulation run with 19 pedestrians in the setting of experiment 1: the simulation results of the circular force formulation from SF^A in Figure 5.5a indicate that simulated pedestrians evade relatively late with a strong deceleration caused by the static person in the center. In order to avoid running into the obstacle, some pedestrians even move slightly backward from the obstacle. This collision avoidance behavior differs significantly from the observed trajectories. As illustrated in Figure 5.5b, the walking behavior from the simulations with SF^B is less abrupt as a result of the included velocity dependence. However, pedestrian deceleration is again unrealistically strong when individuals directly approach the static obstacle. From a qualitative point of view, simulation results obtained by using SF^C exhibit the best results in our comparison (see Figure 5.5c). Separating the forces into a deceleration and an evasive component results in individual trajectories which match very well with the observations.

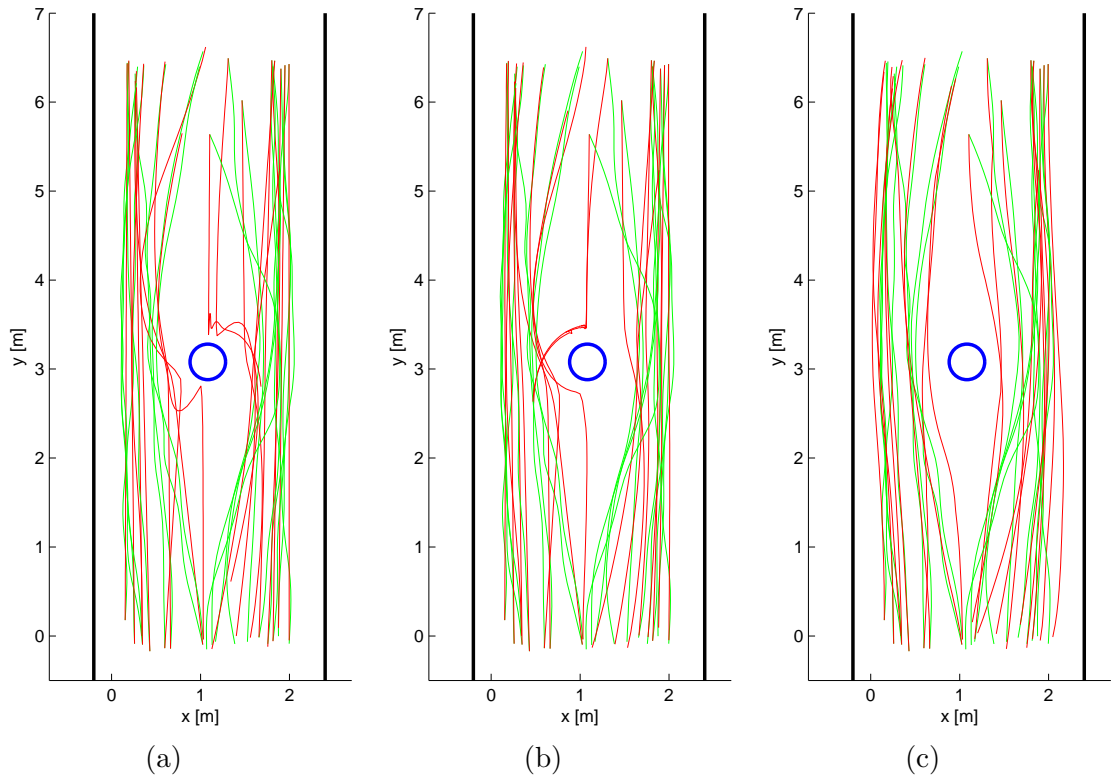


Figure 5.5: Validation results of different Social Force models showing observed (green) and simulated trajectories (red) using (a) SF^A , (b) SF^B and (c) SF^C as repulsive force.

Validation Based On Walking Time Distribution

For capacity estimations in infrastructures the walking times of pedestrians are of particular importance. Accordingly, pedestrian simulation models need to be able to reproduce realistic walking times even if they are not specifically calibrated for this purpose. Since the models in this work were calibrated using the similarity of trajectories as the objective function, we also want to evaluate their ability to correctly predict the walking time distribution based on our validation data set. Figure 5.6 shows the cumulative distribution functions F^M of walking times t_w derived from measured trajectories, and the cumulative distribution functions F^A , F^B , F^C of the simulated trajectories provided by SF^A , SF^B , SF^C respectively. The results for experiment 1 (see Figure 5.6a) demonstrate that the cumulative walking time distribution F^A for the circular formulation and F^B for the elliptical formulation for the repulsive force in the Social Force model significantly deviate from the measured walking time distribution F^M . The formulation SF^C provides a good replication of the measured walking time distribution F^M . In order to support this finding, we used a two-sample Kolmogorov-Smirnov test (see Massey (1951)) to compare each walking time distribution from the simulations with the measured distribution F^M . For a significance level of 0.05, we can reject the null hypothesis that F^A and F^M as well as F^B and F^M are from the same continuous distribution. However, the null hypothesis cannot be rejected when comparing F^C and F^M .

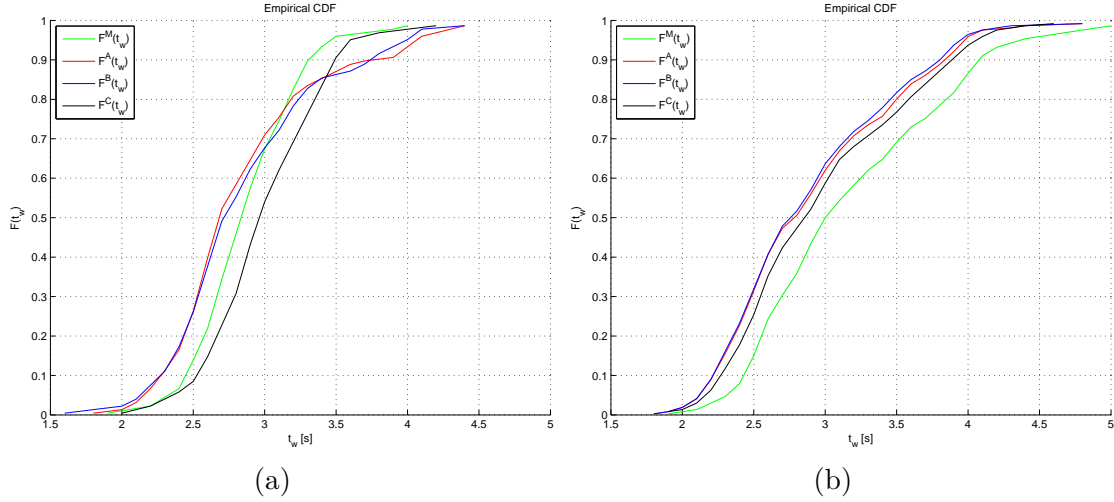


Figure 5.6: Measured and simulated walking time distributions from (a) experiment 1 and (b) experiment 2.

5.3 Summary

In this chapter we have investigated two different calibration procedures for microscopic pedestrian simulation models based on individual trajectory data, that is model estimation by nonlinear least square methods and by comparison of real and simulated trajectories. Both methods were applied to the Social Force approaches SF^A , SF^B and SF^C . Since the Social Force model describes the acceleration of an individual pedestrian, one can directly estimate the model parameters on the accelerations extracted from observed trajectory data. However, this calibration technique is not generalizable for other microscopic modeling approaches, such as the Cellular Automaton model.

A more suitable technique for calibrating and validating a broader range of different models is to estimate parameter values based on comparing the simulation results to various evaluation measures which can be measured from pedestrian movement in real world. As a first step in this respect, we have estimated the dissimilarity between observed and simulated trajectories in this chapter. Furthermore, we have used the comparison between the observed and simulated walking time distribution for model validation.

In Chapter 6 we go further by defining additional evaluation measures and use them for structured model calibration and investigating the individual strength and weaknesses of the modeling approaches described in Chapter 3 in greater detail.

Structured Evaluation of Pedestrian Modeling Approaches

The choice of modeling method can be difficult for the application at hand. One reason for this is that there is a lack of an objective evaluation and comparison of different pedestrian modeling approaches. Hence, we introduce a structured environment including a set of methodologies for the investigation of strengths and weaknesses of various microscopic pedestrian movement simulation models. The empirical baseline for this study is the benchmark data set on pedestrian movement measured under real life conditions which was presented in Chapter 2. We implemented a set of microscopic models, which were described in Chapter 3, within our simulation framework. As presented in Chapter 4, this simulation framework supports switching various simulation models and hence allows for consistent and efficient model calibration and validation.

In this chapter, we define a set of evaluation measures which enable assessing the capabilities of microscopic models for representing important aspects of human movement behavior. Furthermore, we describe and apply a generalized calibration procedure in our simulation framework to estimate the parameter values for the different types of modeling approaches from Chapter 3. After that, a comprehensive evaluation of all microscopic pedestrian simulation models for various scenarios is performed.

6.1 Evaluation Measures for Model Comparison

In microscopic modeling, validation is concerned with the comparison between data obtained from the simulation and empirical data. In order to assess the capabilities of different models to represent important aspects of human movement behavior (e.g. collision avoidance), evaluation measures based on quantities from real world observations can be used. In recent years, the scientific community has developed various measures (Daamen and Hoogendoorn (2003), Davidich and Köster (2013)).

Depending on the application at hand, modelers aim at various objectives which imply different evaluation measures for validation. These objectives can be aimed at revealing the validity of the model with respect to detailed movement and interaction behavior (e.g. on the individual trajectory level), similar "statistical signatures" (e.g. distribution of outcomes) or emerging patterns at the macroscopic level (e.g. aggregated measurements) as observed in the real world.

6.1.1 Microscopic Characteristics

On the microscopic level, a model can be evaluated by comparing the individual trajectory similarity between observed and simulated human movement. Measuring similarity between trajectories is of high relevance as it can be used by many data analysis tasks Wang et al. (2013). In the field of pedestrian simulation, comparison on the individuals' trajectory level are typically performed to evaluate detailed model behavior such as collision avoidance (see Moussaïd et al. (2011), Johansson et al. (2007)).

Since trajectories are essentially high dimensional data attached with both spatial and temporal attributes, the distance between trajectories needs to be carefully defined in order to reflect the true underlying similarity. Hence, a multitude of similarity measures for trajectories have been proposed in the literature. Wang et al. (2013) provide an overview on different trajectory similarity measures. One of the measures for trajectory similarity is the Euclidean distance. It calculates the length of a line that connects two sampling points of two trajectories that are compared. The advantage of applying the Euclidean distance is that it is easy to implement and parameter-free.

For a pedestrian α , the mean Euclidean distance of a measured trajectory \mathcal{T}_α and its corresponding simulated trajectory \mathcal{T}_α^S is given by

$$d(\alpha) = d(\mathcal{T}_\alpha, \mathcal{T}_\alpha^S) = \frac{1}{M_\alpha} \sum_{i=1}^{M_\alpha} \|\mathbf{x}_{\alpha_i} - \mathbf{x}_{\alpha_i}^S\|, \quad (6.1)$$

where the length of trajectories is defined by $|\mathcal{T}_\alpha| = |\mathcal{T}_\alpha^S| = M_\alpha$. As defined in (5.1), the trajectory of a pedestrian α is composed of a vector of timestamps t_α and 2D positions $\mathbf{x}_\alpha = [x_\alpha \ y_\alpha]^T$. A measure for the dissimilarity between a set of N trajectories obtained from measurements and from simulation, respectively, can then be defined as

$$s^{\text{TS}} = \frac{1}{N} \sum_{\alpha=1}^N d(\alpha). \quad (6.2)$$

A pedestrian α is simulated until $\|\mathbf{x}_{\alpha_i} - \mathbf{x}_{\alpha_i}^S\| < 0.5m$, which incorporates a spatial tolerance of pedestrians to reach their individual destination. The individual destination is again derived from the observed trajectory. Note that here we do not use the overlap penalty from Section 5.2.1, since we will now simulate all pedestrians at the same time thus allowing a higher degree of freedom to avoid overlapping as an endogenous function of the model. Hence, it is assumed that all pedestrians being present at the same time have a mutual responsibility to avoid collisions.

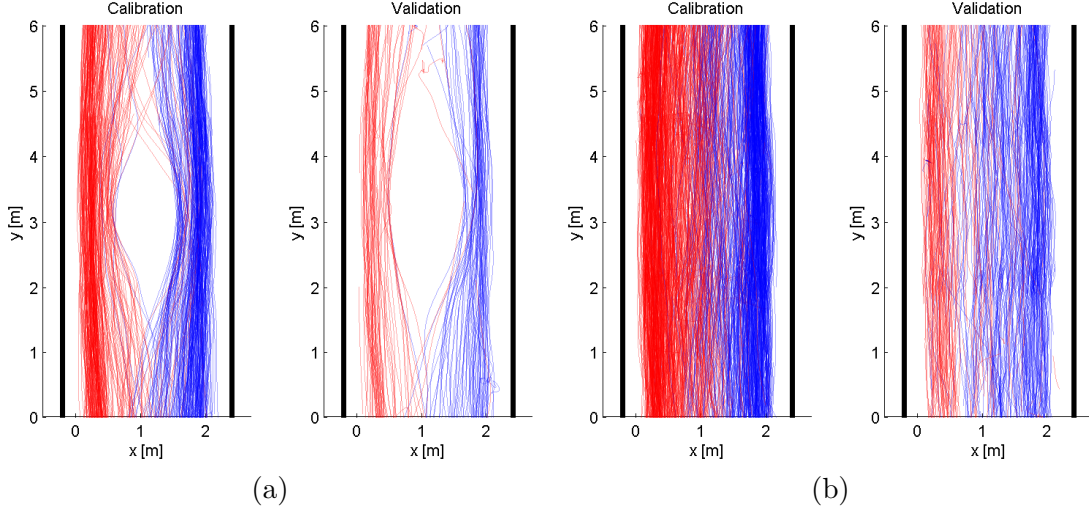


Figure 6.1: Measured trajectories from (a) experiment 1 and (b) experiment 2 with non-overlapping data sets for model calibration and validation.

The evaluations in this work are based on the data sets originating from the automatic tracking approach using the Microsoft Kinect as presented in Chapter 2. We have performed two walking experiments which allowed us to collect sets of trajectories for model calibration and validation. Figure 6.1 illustrates the non-overlapping trajectory data sets obtained from these two experiments (see also Section 5.2). Note that in experiment 1, the person acting as an obstacle in the center of the corridor is explicitly modeled as a static agent in the simulation and is thus not included in the trajectory data sets.

6.1.2 Macroscopic Characteristics

Another level to validate pedestrian simulation models is to evaluate their ability to correctly predict realistic statistics of observable criteria such as density (e.g. levels-of-service) and individual walking times. A realistic representation of walking time is important for estimating the capacity of an infrastructure and predicting the egress times of pedestrians in evacuation scenarios. The walking time can be affected by individual preferences such as the desired velocity. This is taken into account by estimating the desired velocity from the measured trajectories for each person. In addition, different traffic conditions (e.g. varying pedestrian flow rate, mean and standard deviation of speed, and pedestrian density) can also influence the walking time which should then be reflected by the internal mechanisms for collision avoidance of the particular operational pedestrian simulation model. A single average value for the walking times is not sufficient since the shape of the distribution changes with traffic states. Furthermore, walking time distributions can be wide and skewed by many "outliers". Hence, a realistic representation of the distribution of walking times is important.

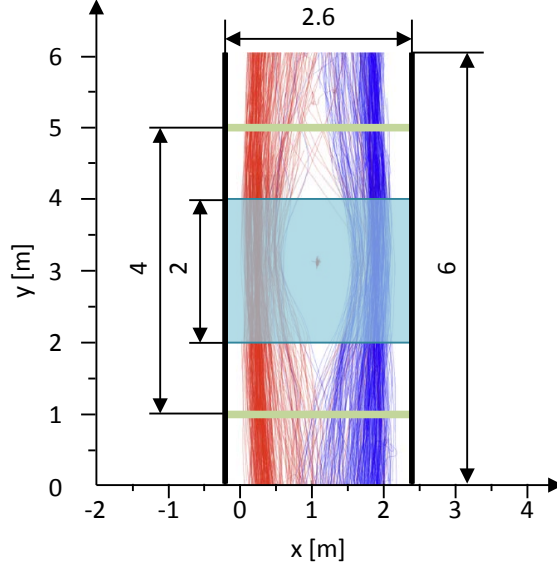


Figure 6.2: Corridor from walking experiments with virtual tripwires (green) for measuring walking times and observation area (marine) for measuring the density.

For the evaluation in this work, we calculate the walking time of a person α by measuring the time it takes for this person to walk a distance of 4 m along the corridor. The distance is defined by two "virtual" tripwires which are placed at certain positions in the corridor (see Figure 6.2). As a result, each walking time for the observed pedestrians is a sample drawn from an empirical distribution.

To compare a distribution from the simulation with the measured distribution, one can apply a two-sample Kolmogorov-Smirnov test (see Massey (1951)) as also described in Section 5.2.2. Since the Kolmogorov-Smirnov statistic quantifies the supremum (greatest) distance, it does not reveal the details for rejecting the null hypothesis that the samples are drawn from the same distribution. Hence, its usage as an evaluation measure in the context of model calibration and validation is rather limited.

Another non-parametric way to estimate the probability density function based on samples of walking times $t_1, t_2, t_3 \dots t_N$ is the Kernel Density Estimation (KDE) which is defined by

$$\hat{f}_h(t) = \frac{1}{Nh} \sum_{\alpha=1}^N K\left(\frac{t - t_\alpha}{h}\right), \quad (6.3)$$

with a kernel function $K(\cdot)$ and a bandwidth $h > 0$. On each of the data points t_α a normal distributed kernel function is placed and the weighted sum of all kernels provides the density estimate. The bandwidth defines the smoothness of the estimated probability density function. We use a bandwidth of 0.09, which was experimentally determined based on our dataset.

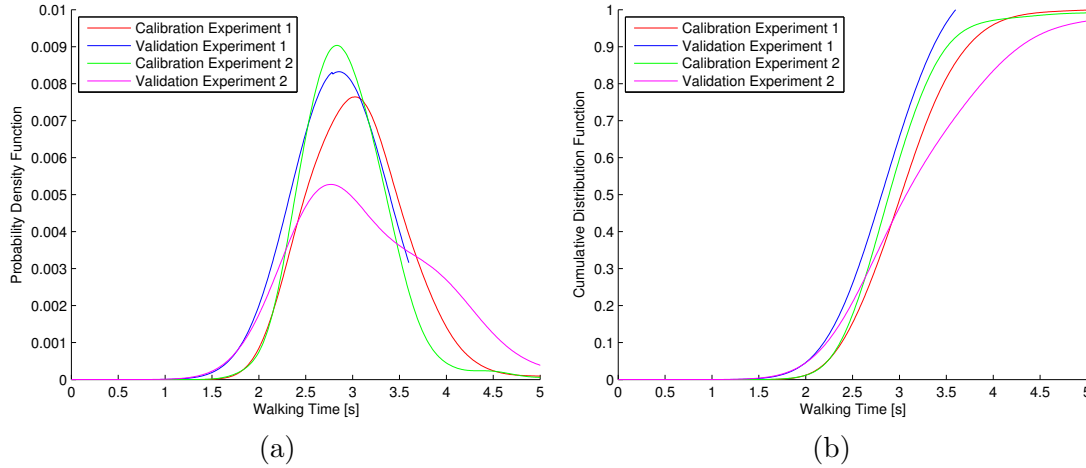


Figure 6.3: Measured walking time distributions represented as (a) probability density function and (b) cumulative distribution function from experiment 1 and experiment 2.

The estimated walking time distributions for our data set from the Infinite Corridor are illustrated in Figure 6.3. Note that in the illustration the estimated distribution is cut off for each data set at the maximal value of the empirical walking time.

A not well-calibrated model might produce results during simulation which deviate severely from the real world observations. For instance, heavy congestions in the simulation can increase the walking times or even prohibit individuals from returning a walking time at all within the simulation duration. In order to cope with individuals in the simulation which have unrealistically high or even no walking times (i.e. pedestrians get stuck), we include a censoring mechanism into our density estimation. According to Rodríguez (2007), censoring is concerned with the fact that for some individuals the event of interest, i.e. the crossing of the second virtual tripwire, has occurred and therefore we know the exact walking time, whereas for others it has not occurred, and all we know is that the walking time exceeds the observation time. The maximum observation time or censoring threshold T is defined as the largest observation in a walking time sample from our real-world measurements (see Figure 6.3). Each data point $t_i > T$ is treated as censored data and therefore set to T . We estimate the probability density function $\hat{f}^S(t)$ with (6.3) using both uncensored and censored data points.

In order to obtain a measure for the dissimilarity between an observed and a simulated walking time distribution, we compute the sum of absolute deviations which is given by

$$s^{\text{WT}} = \sum_{t=0}^T \left| \hat{f}(t) - \hat{f}^S(t) \right|, \quad (6.4)$$

with walking time $t = 0, 0.01, \dots, T$.

Another important aspect for describing the dynamics of pedestrian movement is the definition of flow, density, and speed. Edie (1965) provided their description for the analysis of two-dimensional traffic flows. Based on this definitions for traffic flows, three-dimensional formulations have been developed to apply these formulations to pedestrian movement data. Density and flow are defined as the flux of pedestrian trajectories through a plane specified for the considered volume in the three-dimensional space-time diagram.

The relationship between density, flow, and speed can be encoded in the so-called *Fundamental Diagram*. Many factors can influence the shape of the Fundamental Diagram, such as cultural differences Chattaraj et al. (2009), environmental settings, the trip purpose, the heterogeneity of the pedestrians and the measurement method Seyfried et al. (2010), Steffen and Seyfried (2010). Hence, the literature shows significant differences regarding the specifications of the Fundamental Diagram. As argued by Seyfried et al. (2010) it is crucial that for comparing Fundamental Diagrams one has to assure that they are based on the same measurement approach. This also applies for the calibration and validation of simulation models based on the Fundamental Diagram where model results are evaluated against empirical data.

In order to determine the Fundamental Diagram, different definitions of the density in an area can be used. Steffen and Seyfried (2010) present several concepts for measuring density on the basis of pedestrian trajectories. The definition of the density which is used in most experimental studies is given by

$$D = \frac{N}{|A|}, \quad (6.5)$$

where N is the number of pedestrians in the area A of size $|A|$. As stated by Steffen and Seyfried (2010), this definition has several drawbacks, for instance it suffers from large data scatter. To overcome this problem, Steffen and Seyfried (2010) propose to assign personal space to every pedestrian using a Voronoi diagram which provides cells A_α for each person α (see Figure 6.4). In this work we use the formulation from Steffen and Seyfried (2010) for the density in the measurement area given by

$$D_v = \frac{N}{\sum_{\alpha=1}^N |A_\alpha|}. \quad (6.6)$$

Here, the Voronoi cells are calculated for all persons present in the scene, but only the sizes of the Voronoi cells for the persons inside area A are used to derive the density D_v .

Following Steffen and Seyfried (2010), the velocity from a person α can be derived from its trajectory for a time interval Δt with

$$\mathbf{v}_{\Delta t, \alpha}(t) = \frac{\mathbf{x}_\alpha(t + \Delta t/2) - \mathbf{x}_\alpha(t - \Delta t/2)}{\Delta t}. \quad (6.7)$$

The average velocity for a number of persons N in an observation area A at time t is then given by

$$\bar{v}(t) = \frac{1}{N} \sum_{\mathbf{x}_\alpha(t) \in A} \|\mathbf{v}_{\Delta t, \alpha}(t)\|. \quad (6.8)$$

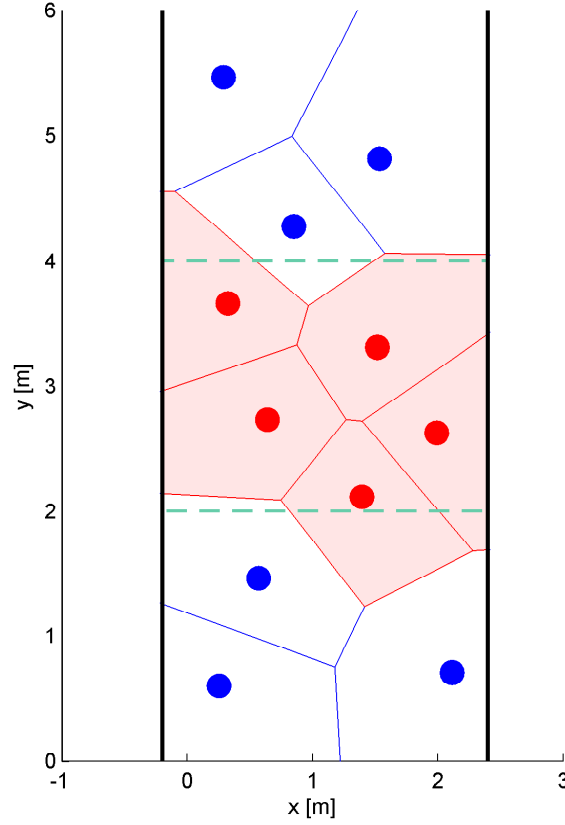


Figure 6.4: Voronoi cells for measuring pedestrian density D_v in an measurement area A (green dashed line) according to (6.6).

The flow Q can be measured by counting the number of persons passing across a line within a time interval or, as used in this work, computed from the average velocity and the density with

$$Q(t) = \bar{v}(t)D_v(t). \quad (6.9)$$

Based on the observed and simulated trajectories, the values for density and flow are computed in area A (see Figure 6.2) for each time step as follows: first, the density is derived using Voronoi cells as defined by (6.6). Then the velocity from each person in the observation area A is calculated according to (6.7) with time interval $\Delta t = 1s$ and the averaged velocity is computed with (6.8). We can estimate the function of the respective Fundamental Diagram by fitting a locally weighted linear regression Hastie et al. (2001). Locally weighted regression solves a separate weighted least squares problem at each target point with a bandwidth h . A straight line is fitted locally and the estimation is then evaluated at M points x_i between $x_0 = 0$ and $x_M = \max(D)$ which are equally spaced with $\Delta x = 0.05$. We have experimentally determined the bandwidth $h = 0.1$.

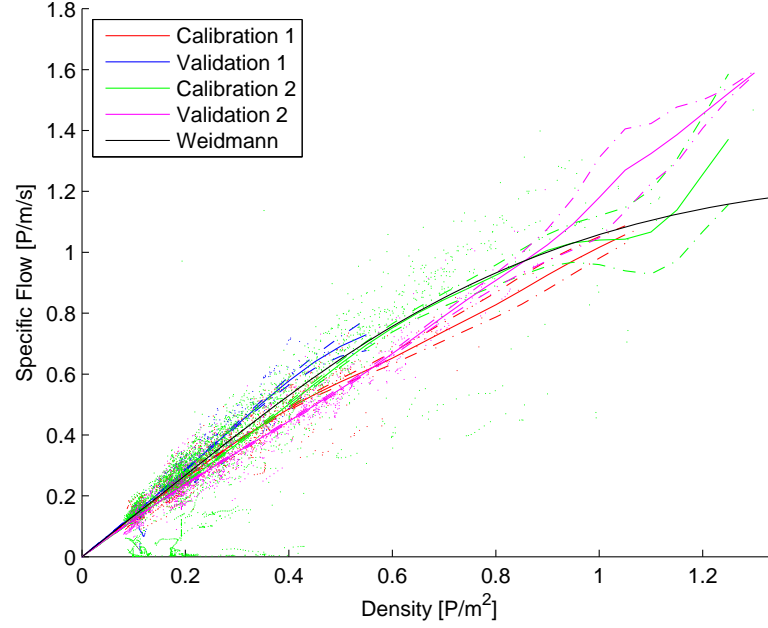


Figure 6.5: Fundamental Diagram derived from the calibration and validation sets from experiment 1 and experiment 2. For comparison the black curve shows the Fundamental Diagram according to Weidmann (1993).

The resulting Fundamental Diagrams for our calibration and validation data set from both experiments are illustrated in Figure 6.5. For the sake of comparison, the Fundamental Diagram from Weidmann (1993) is visualized. It can be seen that within the density range of our data sets a good match with the data from Weidmann (1993) is achieved.

In order to determine the dissimilarity between observation and simulation based on the Fundamental Diagram, we derive the Sum of Squared Error (SSE) which is defined by

$$s^{\text{FD}} = \sum_{i=1}^n \left(\hat{f}(x_i) - \hat{f}^S(x_i) \right)^2, \quad (6.10)$$

where $\hat{f}(x_i)$ and $\hat{f}^S(x_i)$ are the functions of the Fundamental Diagram at point x_i from the observation and the simulation, respectively.

6.2 Generalized Calibration Procedure

As described in Chapter 5 different strategies for calibrating microscopic pedestrian simulations can be applied. For some approaches, such as the Social Force model, it is possible to estimate values for the model parameters directly from the observed data using non-linear regression (see Section 5.1). However, for many modeling approaches their parameters cannot be linked to a meaningful and observable physical representation, such as the accelerations in the Social Force approaches.

Thus, we apply a simulation-based approach for model parameter estimation inspired by Johansson et al. (2007) which allows to determine parameter values for all investigated models in this work. Rudloff et al. (2014) found that it does not pay to simulate all pedestrians separately while keeping remaining pedestrians on their original trajectories during the calibration process. Due to the large number of simulation runs in each step (one for each pedestrian) the overall calibration time will be significantly higher than using a simulation of all pedestrians at once. Additionally, the fit for the individual simulation was worse compared to the simulation of all pedestrians at once in the study of Rudloff et al. (2014).

We address this issue in our work and simulate in the calibration procedure all pedestrians at the same time. This also makes the calibration of multiple simulation models computationally more feasible. Model parameter values are estimated by applying an optimization algorithm to find the best possible fit by minimizing the objective function from the selected evaluation measure, i.e. *Trajectory Similarity*, *Walking Time Distribution* and *Fundamental Diagram* (see Section 6.1). We use the Nelder-Mead algorithm (see Lagarias et al. (1998)) to estimate the parameter values whereas the starting values for the optimization are set according to the description of the individual model in the scientific literature.

The procedure for each simulation run in the calibration with the optimization algorithm is as follows:

1. **Estimating Input Parameters from the Observed Trajectories.** The position and the desired goal for a simulated pedestrian α are extracted from the start point at time t_{α}^{in} and the end point at t_{α}^{out} of the associated observed trajectory \mathcal{T}_{α} . The desired velocity v_{α}^0 of pedestrian α is defined as the 90th percentile of the observed velocities. The magnitude of the current velocity vector \mathbf{v}_{α} is set equal to v_{α}^0 , and it directs towards the pedestrian's desired goal.
2. **Simulating all Pedestrians at the same Time.** Pedestrian α is simulated for $M_{\alpha} = |\mathcal{T}_{\alpha}|$ timesteps until reaching its individual desired goal which was derived from the observed trajectory. Note that we set for each simulated pedestrian $r = 0.2$.
3. **Computing the Fit based on the selected Objective Function.** After having simulated a set of N pedestrians from the calibration data set with the above procedure, the similarity measure s for testing the fit of our simulated trajectories is computed.

6.3 Evaluation and Comparison Results

The model evaluations are based on the benchmarking data set of two scenarios from our walking experiments in the MIT’s Infinite Corridor (see Section 2.3). In summary, we use the following two separated data sets for model calibration and validation from the following scenarios:

- **Experiment 1:** Trajectory data with a single obstacle in the center of the corridor.
- **Experiment 2:** Trajectory data with no obstacle.

Furthermore, as described in Section 6.1, we use our evaluation measures: the Trajectory Similarity (TS) as the fit based on the Euclidean distance, the Walking Time (WT) as the fit between distributions, and the fit of the Fundamental Diagram (FD).

As a basic evaluation, we simulated both experiments using the default parameter values for each model. The default parameter values of the Social Force approaches SF^A and SF^B are based on Rudloff et al. (2014), with slight adaption to match better with the scenario in this study. In Rudloff et al. (2011b) the SF^C model was calibrated with data from observations. For comparability with the other Social Force approaches in our study, we have set $\tau = 0.9$ to be within the defined range. The description of the CA model in Kirchner and Schadschneider (2002) includes an analysis of the parameter sensitivity. However, they do not provide a parameter set of default values for their model. Hence, we defined the default parameter values from visual inspections of the results. For the ORCA model, we used the values from the RVO2 C++ library¹ as default parameter values. However, we set the maximum speed to 1.6 m/s in order to match better with our observations from the experiments. In Seitz and Köster (2012) the OSM^A model was calibrated from careful visual validation to reproduce natural behavior and validated against a Fundamental Diagram. We used the results of their estimations as default parameter values in our study. For the OSM^B model, Seitz and Köster (2014) calibrated the parameters for the interaction between pedestrians to match a Fundamental Diagram and the parameters for obstacles were directly extracted from observations. Following the calibration approach from Seitz and Köster (2014), we adapted the parameters for the interaction with obstacles to match better with our scenario.

Figure 6.6 shows the evaluation results with default parameter values for each model based on the data sets from experiment 1 and 2. We found that the variation in the Fundamental Diagram between the different models is higher for experiment 1 (see FDs from Row 1 and fits from Row 4 in Figure 6.6). Furthermore, the CA and the SF^C model seem to have problems representing the observed walking time distributions from experiment 1 with their default parameter sets. The calibration data set from experiment 1 includes a static person in the corridor center and it appears that these models have stronger reactions to other pedestrians or walls which might cause congestions. The different interaction behavior is also evident in the visualization of the trajectory from a single person in Figure 6.6.

¹RVO2 Library C++ v2.0.1 (released October 26, 2010), see <http://gamma.cs.unc.edu/RVO2/>

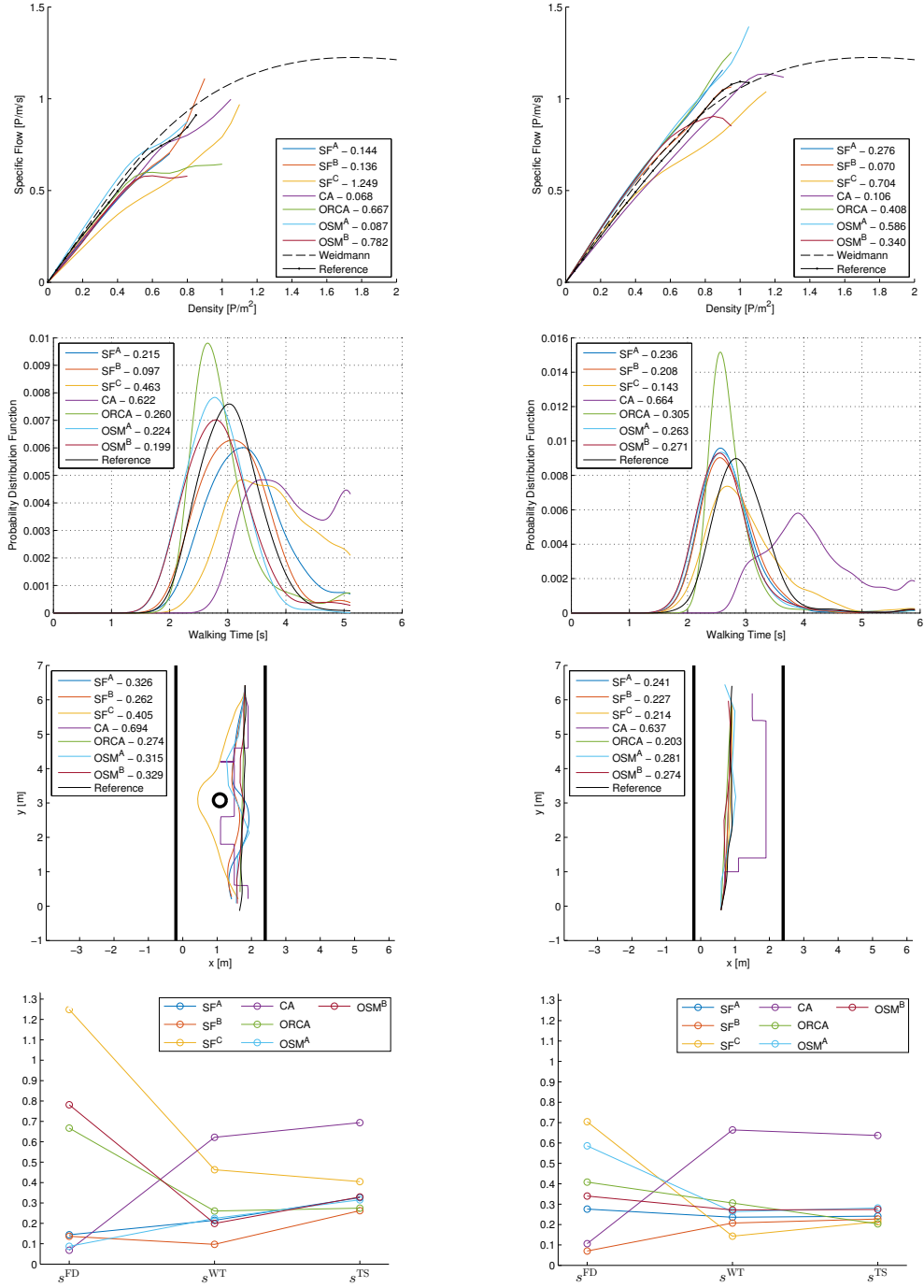


Figure 6.6: Validation results for (left) experiment 1 and (right) experiment 2 with default parameter values. Row 1: Fundamental Diagram. Row 2: Probability density functions of the walking times. Row 3: Trajectory of a single person. Row 4: Fits using the three evaluation measures.

We calibrated each of the seven microscopic models from Chapter 3 using the calibration data set from experiment 1 and 2 with the three defined evaluation measures, i.e. *Trajectory Similarity* (TS), *Walking Time* (WT) and *Fundamental Diagram* (FD). The resulting fit of our calibration is shown in Table 6.1. With the exception of the fit for Fundamental Diagram and Walking Time in experiment 1, the SF^C model performs best after calibration. This might not be surprising, considering that it has the largest number of parameters and hence might be easier to adjust according to the calibration data.

	SF^A	SF^B	SF^C	CA	ORCA	OSM^A	OSM^B
Experiment 1 - FD	0.0436	0.0096	0.0099	0.0403	0.0119	0.1765	0.0586
Experiment 1 - WT	0.0417	0.0796	0.0592	0.2584	0.2441	0.2209	0.2095
Experiment 1 - TS	0.2296	0.2279	0.1938	0.2974	0.2447	0.3004	0.2893
Experiment 2 - FD	0.0723	0.1146	0.0399	0.0304	0.4035	0.1822	0.2701
Experiment 2 - WT	0.1641	0.1438	0.1142	0.3463	0.3018	0.2599	0.2531
Experiment 2 - TS	0.2006	0.1927	0.1856	0.2915	0.1974	0.2736	0.2617

Table 6.1: Fit resulting from our model calibration.

Tables 6.2 to 6.8 show the estimated parameter values resulting from model calibration with different evaluation measures. We also list the default parameter values which were used as starting values in the optimization algorithm for the parameter estimation.

We find that in the SF^A and SF^B model the parameter values for the relaxation time τ are highest when using trajectory similarity as the evaluation measure (see Tables 6.2 and 6.3). In the SF^A model, the parameters controlling the repulsive strength a_p and repulsive range b_p are significantly lower than in the calibration with the other two measures. This effect can also be seen in the SF^B model for the repulsive range b_p in experiment 1. Furthermore, we can observe this behavior also for the parameters with respect to the obstacle interactions, i.e. a_o and b_o . This indicates that when calibrating on individual trajectories, those two models try to match the trajectories and tend to disregard the interactions. However, in the SF^B model the repulsive strength a_p is increased which could somehow mitigate this behavior. When applying the Fundamental Diagram or the walking time as the evaluation measure, the parameter values of the SF^A and SF^B model are in a similar range for both experiments.

	τ	a_p	b_p	a_o	b_o
Default	0.500	1.500	0.500	1.000	0.500
Experiment 1 - FD	0.512	1.240	0.389	0.775	0.417
Experiment 1 - WT	0.300	1.374	0.539	1.104	0.584
Experiment 1 - TS	0.918	0.886	0.098	0.257	0.156
Experiment 2 - FD	0.881	1.797	0.513	0.982	0.518
Experiment 2 - WT	0.892	1.793	0.544	0.917	0.462
Experiment 2 - TS	0.994	1.030	0.166	0.221	0.097

Table 6.2: Parameter values for the SF^A resulting from our model calibration.

	τ	a_p	b_p	a_o	b_o	λ_p	λ_o
Default	0.500	1.500	0.500	1.000	0.500	0.400	0.700
Experiment 1 - FD	0.433	1.240	0.426	0.808	0.400	0.066	0.304
Experiment 1 - WT	0.406	1.259	0.400	0.820	0.413	0.140	0.573
Experiment 1 - TS	0.889	1.461	0.251	0.426	0.149	0.008	0.502
Experiment 2 - FD	0.883	1.665	0.446	0.873	0.481	0.767	0.743
Experiment 2 - WT	0.981	1.676	0.398	0.756	0.411	0.159	0.278
Experiment 2 - TS	0.997	1.526	0.261	0.446	0.115	0.000	0.000

Table 6.3: Parameter values for the SF^B resulting from our model calibration.

In contrast, the SF^C model does not reveal this pattern in the results (see Table 6.4). Only the parameter value for the strength of the evasion force a_e is slightly lower after calibration with the trajectory similarity compared to the other two evaluation measures.

	τ	a_d	b_d	c_d	a_e	b_e	c_e
Default	0.900	0.152	0.196	0.149	1.352	0.258	1.030
Experiment 1 - FD	0.515	0.103	0.197	0.189	1.126	0.286	1.185
Experiment 1 - WT	0.478	0.092	0.231	0.237	1.107	0.331	1.375
Experiment 1 - TS	0.537	0.097	0.152	0.185	0.832	0.220	1.300
Experiment 2 - FD	0.723	0.106	0.159	0.173	0.884	0.237	1.205
Experiment 2 - WT	0.917	0.119	0.204	0.201	0.899	0.341	1.285
Experiment 2 - TS	0.867	0.107	0.166	0.211	0.865	0.358	1.354

Table 6.4: Parameter values for the SF^C resulting from our model calibration.

The CA model has also significantly higher values for all parameters when calibrating with trajectory similarity (see Table 6.5). The weights of the static floor field k_S and the dynamic floor field k_D are both larger than in the calibration with the other two measures. Further, the values for the diffusion γ and decay δ parameters are set both to 1, i.e. the maximum value in the allowed range. An explanation is that the CA model is based on a discrete spatial grid and matching the trajectories from our dataset is best achieved when keeping the pedestrians moving on a straight line along the corridor.

	γ	δ	k_S	k_D
Default	0.300	0.300	10.000	3.000
Experiment 1 - FD	0.886	0.545	12.287	3.304
Experiment 1 - WT	0.935	0.325	20.234	5.200
Experiment 1 - TS	1.000	1.000	118.132	15.622
Experiment 2 - FD	0.771	0.770	12.211	2.993
Experiment 2 - WT	0.965	0.957	22.336	5.041
Experiment 2 - TS	1.000	1.000	641.120	16.975

Table 6.5: Parameter values for the CA resulting from our model calibration.

The calibration results for the ORCA model in Table 6.6 show that the estimated parameters are the same for both experiments when using the trajectory similarity as the evaluation measure. The values of the time horizon with respect to obstacles τ_o is noticeably smaller, indicating that obstacles have less influence on the pedestrians. The calibration with trajectory similarity as the evaluation measure resulted in the same parameter values for experiment 1 and 2. In this case the amount of time τ_o for which a person will respond to the presence of obstacles is very small, thus, giving persons more freedom to choose their velocities.

	τ_p	τ_o
Default	10.000	5.000
Experiment 1 - FD	10.991	5.296
Experiment 1 - WT	8.086	3.613
Experiment 1 - TS	9.394	0.477
Experiment 2 - FD	14.550	5.256
Experiment 2 - WT	12.214	6.107
Experiment 2 - TS	9.394	0.477

Table 6.6: Parameter values for the ORCA resulting from our model calibration.

For the OSM^A (see Table 6.7) and the OSM^B (see Table 6.8) we can observe that the resulting parameter values are significantly decreased when calibrating with trajectory similarity as the evaluation measure. Again, this might be an indicator that the trajectory match is put in favor of the interactions with other pedestrians and obstacles. For the calibration of the OSM^B with walking time distribution based on the data set of experiment 1, the best fit was found with the default parameter values of the model.

	h_p	a_p	b_p	w_p	h_o	a_o	b_o	w_o
Default	0.400	1.000	0.200	1.000	0.200	3.000	2.000	6.000
Experiment 1 - FD	0.431	0.957	0.203	1.033	0.233	3.063	1.827	6.140
Experiment 1 - WT	0.435	1.017	0.199	0.966	0.190	2.705	1.712	5.774
Experiment 1 - TS	0.412	0.693	0.109	0.474	0.070	0.981	0.715	3.543
Experiment 2 - FD	0.462	1.094	0.229	1.079	0.200	2.843	1.793	6.341
Experiment 2 - WT	0.465	1.105	0.210	1.000	0.190	2.715	1.721	6.308
Experiment 2 - TS	0.394	0.817	0.140	0.649	0.116	1.657	1.122	5.422

Table 6.7: Parameter values for the OSM^A resulting from our model calibration.

	w_p	h_p	w_o	h_o
Default	0.330	1.050	0.400	1.500
Experiment 1 - FD	0.590	0.786	0.956	2.267
Experiment 1 - WT	0.330	1.050	0.400	1.500
Experiment 1 - TS	0.266	0.560	0.195	0.848
Experiment 2 - FD	0.400	1.263	0.441	1.494
Experiment 2 - WT	0.444	1.360	0.559	1.748
Experiment 2 - TS	0.238	0.538	0.123	0.711

Table 6.8: Parameter values for the OSM^B resulting from our model calibration.

As for a more detailed analysis of the capabilities of the different models, Figure 6.7 illustrates the calibration results with parameter estimations based on the calibration data set from experiment 1. Generally, we found that all models were able to improve their fit to the observed data set after calibration. Using trajectory similarity as the evaluation measure provides rich information for estimating the parameter values. Hence, the other two evaluation measures, i.e. Fundamental Diagram and walking time distribution, have also a reasonably good fit. However, when calibrating with aggregated information from the Fundamental Diagram, still a good model fit can be achieved. Even only using the information from the walking time distribution seems to be sufficient to get a good fit for most of the examined models.

Figure 6.8 shows the results of the calibration with the data set from experiment 2. The main findings are similar to those from the calibration based on experiment 1. However, the variation in the results for the evaluation with the Fundamental Diagram is higher. Furthermore, the fits for the calibration with the FD are slightly worse for experiment 2. Similarly, the fits when calibrating on the walking time distributions are worse for most cases. This suggests the following: although, the trajectories can be fitted well with the data from experiment 2, it is clear that it includes less pedestrian interaction compared to experiment 1. Hence, it appears that the available information about the pedestrian behavior is not sufficient to fully calibrate the models.

The results for the model fits based on the evaluation with the calibration data sets are shown in Tables A.1 to A.7 in Appendix A. We can see the fit for each model after calibration with the respective evaluation measure as bold values in the tables. Furthermore, the sub-matrix with nine values in the upper left and lower right indicate the fit for different evaluation measures using the data set from the same experiment for calibration and validation. The cross-validation, i.e. calibration with data from experiment 1 and validation with data from experiment 2, is shown in the sub-matrix in the upper right of the table. Similarly, the cross-validation where calibration was performed with data from experiment 2 and validation with data from experiment 1 can be found in the sub-matrix in the lower left of the table. For instance, in Table A.1 some fits in the lower left sub-matrix are significantly worse (i.e. for calibration with WT and FD) compared to the remaining fits in this table. An explanation for this observation is that the absence of a static person in the data set from experiment 2

used for calibration leads to parameter values for the SF^A model which, when applied to the setting in experiment 1, cannot fully explain the required interaction behavior. The SF^C model performs better on the more complex data set from experiment 1 when calibrated on less complex data set from experiment 2 in comparison with the SF^B model. In turn, when calibrating on the data set from experiment 1, the fits on the data set from experiment 2 are comparable. It appears that the ORCA model and the CA model perform similarly for all data sets which suggests that the calibration has only slight influence on the resulting pedestrian behavior. Hence, there might be not enough or relevant parameters that can be calibrated.

We then performed a cross-validation in which we used the parameter sets from a calibration run with a specific evaluation measure (e.g. trajectory similarity) and validated the model against an independent data set representing another evaluation measure (e.g. Fundamental Diagram). The results of this cross-validation are provided in Tables A.8 to A.14 in Appendix A. It can be observed that the main findings from the validation data set are comparable to the previous results from using the calibration data set. For the validation data set, however, the fit of the CA model has noticeably decreased in the comparisons with the Fundamental Diagram in experiment 2. Since the examination of model transferability gives varying results, future work should focus on extending these tests with additional empirical data sets from scenes with different pedestrian interactions, such as denser pedestrian traffic or changing numbers of static obstacles.

6.4 Summary

In this chapter we have evaluated seven different microscopic modeling approaches, that is the Social Force (SF) models SF^A , SF^B and SF^C , the Cellular Automaton (CA) model, the Optimal Reciprocal Collision Avoidance (ORCA) model, and the Optimal Steps Model (OSM) approaches OSM^A and OSM^B (for details on the models see Chapter 3). By first calibrating all models on the same data set, we have created a baseline that allows objectively assessing and comparing these models. Therefore, we used certain evaluation measures, i.e. Trajectory Similarity, Walking Time and Fundamental Diagram, within the objective functions in a simulation-based calibration procedure which compares the simulation results to various characteristics that can be measured from pedestrian movement in real world.

Our investigations are based on the calibration data set and a separate validation data set from our benchmarking data set. These include trajectory data with a single obstacle in the center of the corridor (i.e. experiment 1) and with no obstacle (i.e. experiment 2). The results indicate that our calibration has improved the fit to the observed data set in all models. However, the grade to which individual models can be influenced by the calibration varies. The models also reveal different capabilities with respect to transferability to another data set than the one used for calibration.

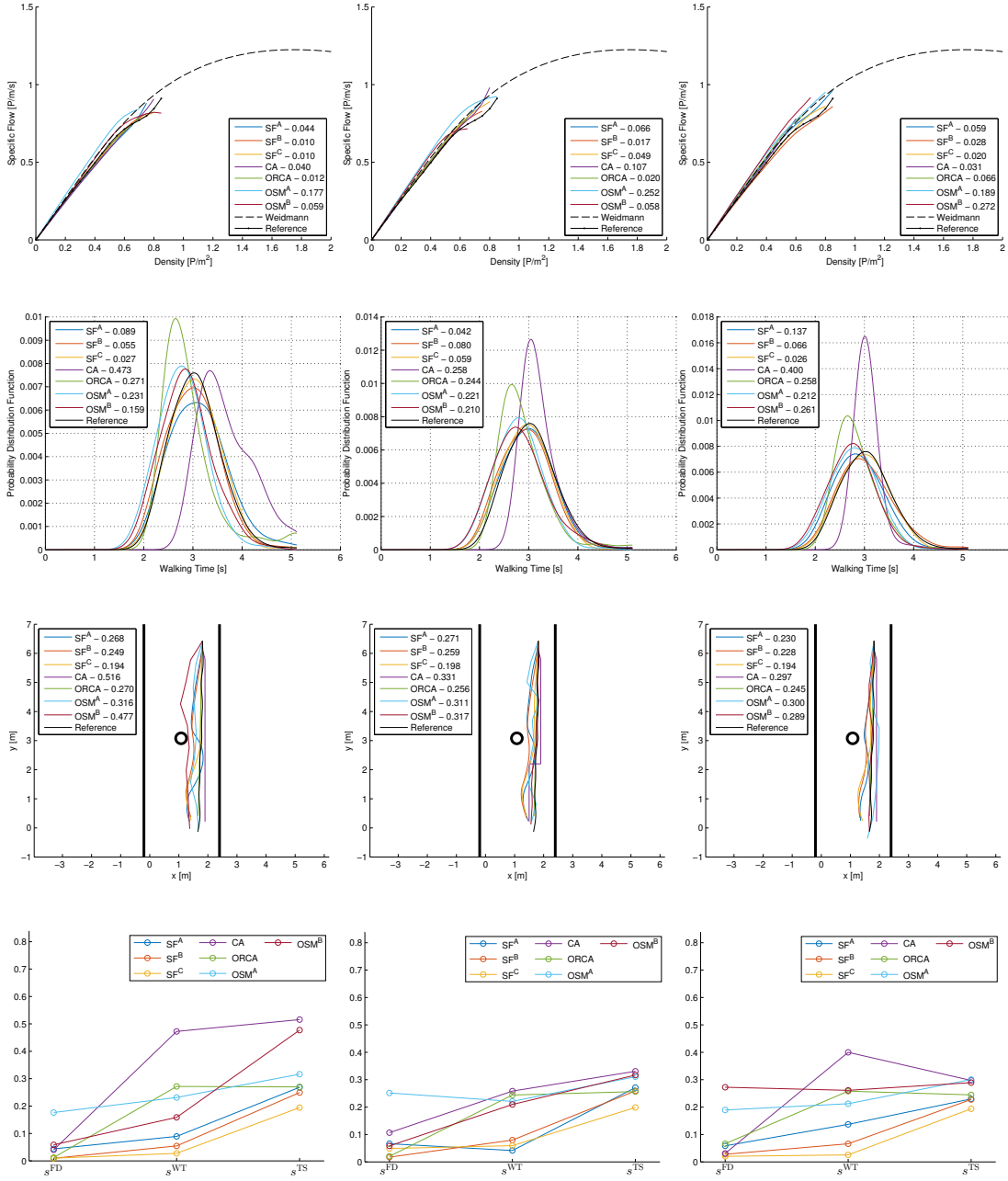


Figure 6.7: Calibration results for experiment 1 with (left) Fundamental Diagram (FD), (middle) Walking Time (WT) and (right) Trajectory Similarity (TS) as evaluation measures. Row 1: Fundamental Diagrams. Row 2: Probability density functions of the walking times. Row 3: Trajectory of a single person. Row 4: Fits using the three evaluation measures.

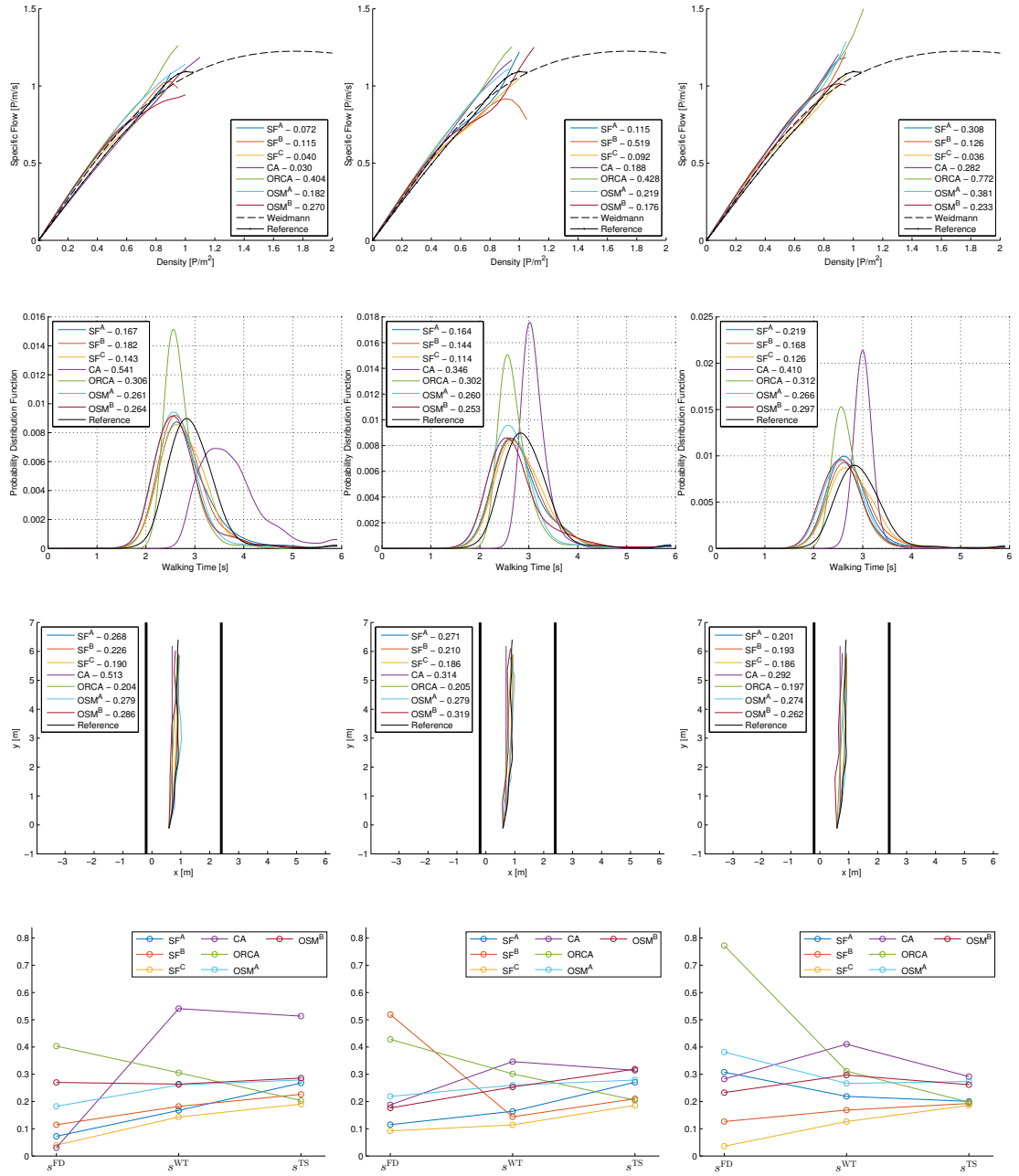


Figure 6.8: Calibration results for experiment 2 with (left) Fundamental Diagram (FD), (middle) Walking Time (WT) and (right) Trajectory Similarity (TS) as evaluation measures. Row 1: Fundamental Diagrams. Row 2: Probability density functions of the walking times. Row 3: Trajectory of a single person. Row 4: Fits using the three evaluation measures.

Conclusion and Future Research

The research in this thesis has focused on the development of a unified framework for evaluating microscopic pedestrian simulation models. First we have introduced algorithms to use the Microsoft Kinect – basically a camera that also records 3-dimensional information in the form of a depth image – for automatic data collection of pedestrian movement from an elevated view. Further, we developed a flexible simulation framework which allows to easily switch and combine pedestrian simulation models based on a highly scalable system architecture. This allowed us to build an optimal basis for structured learning on strengths and weaknesses of various pedestrian movement simulation models. Finally, we investigated seven microscopic pedestrian simulation models by calibrating them with our real-world benchmarking data set and validating them with different evaluation measures. In the remainder of this chapter, we conclude this thesis by discussing the presented contributions and providing an outlook of possible research directions.

7.1 Discussion

We have shown that the use of the Kinect allows the automated capture of human motion trajectories with high accuracy and without privacy issues. We applied our tracking algorithm to collect an extensive data set in the MIT's Infinite Corridor for calibrating and comparing microscopic pedestrian simulation models. Our approach groups depth information from a single Kinect in the world coordinate system into individual pedestrians based on hierarchical clustering. These detections are tracked over time throughout the sensing areas of multiple Kinects to obtain individual trajectories in larger space. Evaluating the detection performance with two manually annotated ground truth data sets shows a Pedestrian Detection Rate of 94% and 96%, respectively. The position error for all correctly tracked objects is quantified as Multiple Object Tracking Precision and reveals relatively small values of around 4 cm. By applying our tracking

approach in two walking experiments performed under real world conditions in the MIT's Infinite Corridor, we gathered a total of 2674 trajectories which were subsequently used for our model calibration and validation.

The modular system architecture of the presented simulation framework allows to easily switch and combine different behavioral models. The modules can be kept simple and focused on a well-defined set of functionalities which we have structured according to the different levels of decision making, that is strategic, tactical and operational (see Hoogendoorn and Bovy (2004)). The loose coupling is achieved by using the messaging server ActiveMQ (The Apache Software Foundation (2014)) for efficient and reliable communication between the simulation core and the connected modules. Hence, all modules are separate processes which can be run independently and even be implemented in different programming languages. The simulation framework facilitates the comparison of different models for the same scenario disclosing the respective strengths and weaknesses. Moreover, it allows combining different models for exploiting the best possible model for any particular scenario. These functionalities have been demonstrated in two real world case studies making two different points: the first case study documented the comparison of different operational models for the same scenario of passenger flows during boarding and alighting a train. The investigated scenario hereby was no academic example but arising in a real world application of designing public transport vehicles. The same scenario has been simulated using different models to examine the best suited model for the application. The case study clearly showed that the framework is capable of discovering weaknesses of models that would not be visible from a mere comparison of some parameters of prediction performance. The second case study examined a stylized fact in the crowd simulation community which is the claim that macroscopic simulations are superior to microscopic ones in terms of computation times but less accurate due to reduced detail. In the application, two levels of a subway station have been simulated. While a microscopic model simulated passenger movement on the upper level of the station, for the entry level alternately a micro- and a macroscopic model have been used. The results show that it depends on the parameter investigated whether the claim holds true or not. If one is only interested in the cumulative number of persons transported or the maximal number of persons on the platform investigated, both models provide almost identical results with the macroscopic model consuming approximately only one tenth of computation time in the most crowded setting. If, however, also route-choice is of interest, both models perform significantly different and hence the choice of the model for simulation has a big impact on the results achieved. Thus, this case study demonstrated that the framework can be used to investigate the relative merits between two models in depth – not only with respect to accuracy but also with respect to the accuracy versus computation time trade-off.

We compared implementations of the Social Force model (SF^B) Helbing and Johansson (2009), the Optimal Reciprocal Collision Avoidance (ORCA) model van den Berg et al. (2011) and the Optimal Steps Model (OSM^A) Seitz and Köster (2012) based on selected test cases from the RiMEA-Guideline. This comparison showed differing results for the three modeling approaches in all three test cases but did not provide identifiability

of systematic behavior for each individual model. We found that these test cases lack of quantifiable measures based on empirical data from experimental or real-world observations. Moreover, an evaluation using only the test cases from the RiMEA-Guideline, did not allow for thoroughly investigating the capabilities of different modeling approaches. Hence, we compared three variations of the Social Force model by calibrating them with our trajectory data using two different strategies: first, we estimated the model parameter values and their distribution based on non-linear least square parameter estimation. Due to the high quality of the trajectory data originated from this work, the problem of errors in variables in the calibration was reduced. This lead to parameter values for the investigated models which reveal good collision avoidance behavior, despite the relatively simple scenario with low pedestrian densities. Secondly, we used a simulation-based calibration approach where each pedestrian was simulated separately while keeping the remaining pedestrians on their observed trajectory. The validation results revealed that collision avoidance behavior in the Social Force model can be improved by including the relative velocity between individuals. Furthermore, dividing the repulsive force into a deceleration and an evasion part delivered the best quantitative and qualitative results out of the investigated models. However, dividing the repulsive force leads to a larger number of parameters, which makes the calibration process itself more complex and computationally expensive.

We went further in the investigation of the individual strengths and weaknesses of the modeling approaches by defining additional evaluation measures and used them for model calibration and validation. These evaluation measures include microscopic characteristics, i.e. trajectory similarity, and macroscopic characteristics, i.e. walking time and Fundamental Diagram, which were extracted from our benchmarking data set. In order to set a common baseline for all models, we first calibrated them with pedestrian trajectories from two experiments, that is pedestrian movement in the MIT’s Infinite Corridor with a single obstacle in the center of the corridor and with no obstacle. A simulation-based calibration procedure was applied which estimates the model parameter values by optimizing the fit of an objective function represented by the individual evaluation measure. This fit indicates how well a model can represent an observable characteristic of pedestrian movement described by a certain evaluation measure and hence was also used for quantifying the performance of each model. We found that after calibration the fit to the observed data set has improved in all models. However, the grade to which individual models can be influenced by the calibration varies. The investigated models also revealed diverse capabilities concerning transferability to an independent data set. Since the models in this study were calibrated and validated for rather low density situations measured in the corridor with bidirectional flow, it has to be examined whether these modeling approaches are capable of simulating high density crowd movement.

7.2 Outlook

Our tracking approach is capable of delivering trajectories with an accuracy which we consider sufficient for calibrating microscopic pedestrian simulation models. In the future our approach could be extended to estimate the orientation of body parts, i.e. head and shoulder pose. This would allow to gain more data on how humans perceive and interact with their environment which is particularly useful for evaluating visual information systems, such as guidance systems or lights. For future work we will increase our data set by obtaining trajectories under additional settings. Hence, other movement phenomena (e.g. crossing, uni-directional movements, turning of corners, etc.) can be observed which will allow for validating microscopic pedestrian simulation models on the operational level completely. This will also allow us to further investigate the transferability of different models to different scenarios. We also intend to automate the sensor calibration process. For example, the accuracy of an approach performing registration on robust 3D point sets such as described in Mavrinac et al. (2010) could be compared to the manual setup. Furthermore, including Kalman filters for pedestrian tracking might be useful for real-time applications performing more complex object detection algorithms which would not allow processing at the full Kinect framerate. Going forward we believe that the adoption of the Kinect could be extremely useful for the development and calibration of pedestrian models – but also as a tool to better understand human crowd behavior and hence provide invaluable input to the design of all those spaces that need to respond to it.

The simulation framework provides a solid basis for obtaining more information on the relative merits of the multitude of models suggested in the literature to date. But it offers much more potential which needs to be developed further in the future: the framework also allows the combination of different models in different sections of the infrastructure. Currently there is not much research available on how to model the transitions of pedestrians from one section of the infrastructure to another. As pedestrians currently are modeled section by section, pedestrians in adjacent sections do not influence each other which causes problems. Preliminary ideas to solve this problems are contained in Lämmel et al. (2014) but more work is needed.

The presented evaluation of different models with the proposed simulation framework produced valuable insights into the investigated models. Our technique can easily be applied to a wide range of different pedestrian modeling approaches by including them as separate, additional modules in our simulation framework. Hence, we encourage that assessing the performance characteristics should be applied to a variety of models with our structured way for model calibration and validation. For future studies this will support the understanding of individual model characteristics and the comparison of novel modeling approaches to existing ones. Furthermore, this could eventually lead to a scientifically accepted standardized procedure based on benchmarking datasets and evaluation measures which allow an objective assessments and comparisons of microscopic pedestrian simulation models.

Detailed Calibration And Validation Results

This appendix presents the detailed results of the model fit resulting from the comparison with the calibration data set and the validation data set (see Figure 6.1) based on the work from Chapter 6.

A.1 Model Fit based on the Calibration Data Set

Tables A.1 to A.7 provide details on the fit after model calibration with the data sets from experiment 1 and 2. The presented values for the fit were calculated with the calibration data set from the respective experiments. Bold values in the tables denote the fit derived from model calibration for the individual evaluation measure.

Validation Calibration	Experiment 1			Experiment 2		
	FD	WT	TS	FD	WT	TS
Experiment 1 - FD	0.0436	0.0893	0.2685	0.3123	0.2529	0.2345
Experiment 1 - WT	0.0665	0.0417	0.2710	0.3425	0.2713	0.2522
Experiment 1 - TS	0.0586	0.1369	0.2296	0.3801	0.2332	0.2070
Experiment 2 - FD	9.4189	0.8623	1.3171	0.0723	0.1672	0.2677
Experiment 2 - WT	9.4352	0.8470	1.3562	0.1150	0.1641	0.2706
Experiment 2 - TS	0.0869	0.1040	0.2305	0.3077	0.2188	0.2006

Table A.1: Fit for the SF^A model based on the calibration data set.

Validation Calibration	Experiment 1			Experiment 2		
	FD	WT	TS	FD	WT	TS
Experiment 1 - FD	0.0096	0.0546	0.2493	0.0915	0.2156	0.2254
Experiment 1 - WT	0.0172	0.0796	0.2588	0.3527	0.2311	0.2322
Experiment 1 - TS	0.0278	0.0659	0.2279	0.2490	0.1883	0.1971
Experiment 2 - FD	0.4831	0.2357	0.3202	0.1146	0.1820	0.2263
Experiment 2 - WT	0.9182	0.2655	0.3005	0.5192	0.1438	0.2102
Experiment 2 - TS	0.0880	0.0664	0.2300	0.1264	0.1684	0.1927

Table A.2: Fit for the SF^B model based on the calibration data set.

Validation Calibration	Experiment 1			Experiment 2		
	FD	WT	TS	FD	WT	TS
Experiment 1 - FD	0.0099	0.0274	0.1944	0.0645	0.1874	0.2048
Experiment 1 - WT	0.0490	0.0592	0.1984	0.1414	0.2133	0.2136
Experiment 1 - TS	0.0202	0.0256	0.1938	0.0809	0.1889	0.2038
Experiment 2 - FD	0.0862	0.1364	0.2094	0.0399	0.1430	0.1904
Experiment 2 - WT	0.2329	0.2606	0.2483	0.0919	0.1142	0.1858
Experiment 2 - TS	0.1125	0.1804	0.2194	0.0361	0.1265	0.1856

Table A.3: Fit for the SF^C model based on the calibration data set.

Validation Calibration	Experiment 1			Experiment 2		
	FD	WT	TS	FD	WT	TS
Experiment 1 - FD	0.0403	0.4726	0.5155	0.1549	0.5301	0.5118
Experiment 1 - WT	0.1066	0.2584	0.3305	0.0447	0.3350	0.3392
Experiment 1 - TS	0.0310	0.3999	0.2974	0.2824	0.4056	0.2931
Experiment 2 - FD	0.0241	0.4531	0.4966	0.0304	0.5410	0.5133
Experiment 2 - WT	0.0364	0.3146	0.3184	0.1877	0.3463	0.3142
Experiment 2 - TS	0.0696	0.4167	0.3042	0.2824	0.4103	0.2915

Table A.4: Fit for the CA model based on the calibration data set.

Validation Calibration	Experiment 1			Experiment 2		
	FD	WT	TS	FD	WT	TS
Experiment 1 - FD	0.0119	0.2715	0.2700	0.4234	0.3050	0.2043
Experiment 1 - WT	0.0203	0.2441	0.2563	0.4289	0.3097	0.2017
Experiment 1 - TS	0.0664	0.2581	0.2447	0.7721	0.3116	0.1974
Experiment 2 - FD	0.0273	0.2705	0.2670	0.4035	0.3055	0.2036
Experiment 2 - WT	0.0179	0.2843	0.2774	0.4280	0.3018	0.2047
Experiment 2 - TS	0.0664	0.2581	0.2447	0.7721	0.3116	0.1974

Table A.5: Fit for the ORCA model based on the calibration data set.

Validation Calibration	Experiment 1			Experiment 2		
	FD	WT	TS	FD	WT	TS
Experiment 1 - FD	0.1765	0.2313	0.3163	0.5229	0.2517	0.2789
Experiment 1 - WT	0.2515	0.2209	0.3109	0.3335	0.2610	0.2774
Experiment 1 - TS	0.1894	0.2124	0.3004	0.2996	0.2690	0.2719
Experiment 2 - FD	0.2504	0.2268	0.3123	0.1822	0.2606	0.2790
Experiment 2 - WT	0.2478	0.2198	0.3136	0.2185	0.2599	0.2789
Experiment 2 - TS	0.1832	0.2340	0.2987	0.3814	0.2664	0.2736

Table A.6: Fit for the OSM^A model based on the calibration data set.

Validation Calibration	Experiment 1			Experiment 2		
	FD	WT	TS	FD	WT	TS
Experiment 1 - FD	0.0586	0.1588	0.4773	0.2120	0.2250	0.4034
Experiment 1 - WT	0.0583	0.2095	0.3168	0.2816	0.2770	0.2779
Experiment 1 - TS	0.2725	0.2610	0.2893	0.7657	0.2923	0.2639
Experiment 2 - FD	3.7688	0.1963	0.3533	0.2701	0.2640	0.2860
Experiment 2 - WT	0.3064	0.1852	0.3738	0.1760	0.2531	0.3188
Experiment 2 - TS	0.4728	0.2549	0.2904	0.2327	0.2969	0.2617

Table A.7: Fit for the OSM^B model based on the calibration data set.

A.2 Model Fit based on the Validation Data Set

Tables A.8 to A.14 provide details on the fit after model calibration with the data sets from experiment 1 and 2. The presented values for the fit were calculated with the validation data set from the respective experiments.

Validation Calibration	Experiment 1			Experiment 2		
	FD	WT	TS	FD	WT	TS
Experiment 1 - FD	0.2212	0.1552	0.2523	0.4001	0.1161	0.1581
Experiment 1 - WT	0.1205	0.0647	0.2423	0.4239	0.1252	0.1678
Experiment 1 - TS	0.0107	0.1470	0.2049	0.3694	0.1070	0.1356
Experiment 2 - FD	8.0801	0.5630	0.8249	0.3585	0.0932	0.1946
Experiment 2 - WT	4.9734	0.5915	1.1904	0.1559	0.0915	0.1957
Experiment 2 - TS	0.0093	0.0836	0.2060	0.3497	0.1021	0.1336

Table A.8: Fit for the SF^A model based on the validation data set.

Validation Calibration	Experiment 1			Experiment 2		
	FD	WT	TS	FD	WT	TS
Experiment 1 - FD	0.1066	0.0549	0.2239	0.1792	0.1081	0.1454
Experiment 1 - WT	0.0215	0.0864	0.2304	0.2132	0.1110	0.1494
Experiment 1 - TS	0.0189	0.0641	0.1993	0.2258	0.0920	0.1316
Experiment 2 - FD	0.7218	0.3212	0.3098	0.2242	0.0969	0.1576
Experiment 2 - WT	0.7803	0.2453	0.2645	0.0492	0.0782	0.1456
Experiment 2 - TS	0.0329	0.0484	0.1959	0.1784	0.0864	0.1297

Table A.9: Fit for the SF^B model based on the validation data set.

Calibration \ Validation	Experiment 1			Experiment 2		
	FD	WT	TS	FD	WT	TS
Experiment 1 - FD	0.0169	0.0516	0.1820	0.2314	0.1054	0.1439
Experiment 1 - WT	0.0031	0.0401	0.1785	0.2810	0.1094	0.1469
Experiment 1 - TS	0.0082	0.0190	0.1833	0.2532	0.1065	0.1429
Experiment 2 - FD	0.1333	0.1819	0.2035	0.1835	0.0960	0.1337
Experiment 2 - WT	0.3238	0.2915	0.2457	0.1433	0.0864	0.1312
Experiment 2 - TS	0.1856	0.2176	0.2147	0.1984	0.0875	0.1344

Table A.10: Fit for the SF^C model based on the validation data set.

Calibration \ Validation	Experiment 1			Experiment 2		
	FD	WT	TS	FD	WT	TS
Experiment 1 - FD	0.3290	0.4937	0.4986	1.0692	0.2611	0.3439
Experiment 1 - WT	0.1520	0.2972	0.3384	2.3157	0.2326	0.2678
Experiment 1 - TS	0.0440	0.2421	0.2833	2.3877	0.2612	0.2550
Experiment 2 - FD	0.1577	0.4836	0.4998	0.8873	0.2532	0.3394
Experiment 2 - WT	0.0401	0.2791	0.3193	2.2620	0.2514	0.2607
Experiment 2 - TS	0.1651	0.2407	0.2917	2.3884	0.2619	0.2547

Table A.11: Fit for the CA model based on the validation data set.

Calibration \ Validation	Experiment 1			Experiment 2		
	FD	WT	TS	FD	WT	TS
Experiment 1 - FD	0.0656	0.2550	0.2022	0.5421	0.1305	0.1290
Experiment 1 - WT	0.0650	0.2585	0.2003	0.5397	0.1275	0.1295
Experiment 1 - TS	0.0262	0.2479	0.2065	0.5318	0.1263	0.1303
Experiment 2 - FD	0.0665	0.2550	0.2016	0.5314	0.1318	0.1288
Experiment 2 - WT	0.0656	0.2533	0.2023	0.5413	0.1335	0.1291
Experiment 2 - TS	0.0262	0.2479	0.2065	0.5318	0.1263	0.1303

Table A.12: Fit for the ORCA model based on the validation data set.

Calibration \ Validation	Experiment 1			Experiment 2		
	FD	WT	TS	FD	WT	TS
Experiment 1 - FD	0.1117	0.2632	0.2832	0.3573	0.1264	0.2092
Experiment 1 - WT	0.1085	0.2454	0.2819	0.6507	0.1271	0.2028
Experiment 1 - TS	0.0831	0.2318	0.2678	0.6145	0.1312	0.1954
Experiment 2 - FD	0.1637	0.2687	0.2791	0.8190	0.1275	0.2012
Experiment 2 - WT	0.0941	0.2266	0.2804	0.5196	0.1265	0.2006
Experiment 2 - TS	0.1308	0.2580	0.2715	0.6160	0.1252	0.1958

Table A.13: Fit for the OSM^A model based on the validation data set.

Calibration \ Validation	Experiment 1			Experiment 2		
	FD	WT	TS	FD	WT	TS
Experiment 1 - FD	0.0163	0.1405	0.4560	1.7416	0.1113	0.3102
Experiment 1 - WT	0.0384	0.2726	0.2742	0.6046	0.1291	0.1960
Experiment 1 - TS	0.0783	0.2815	0.2629	0.8075	0.1381	0.1823
Experiment 2 - FD	2.9083	0.1738	0.4018	0.8443	0.1326	0.2058
Experiment 2 - WT	2.5978	0.1769	0.4018	0.9157	0.1230	0.2275
Experiment 2 - TS	0.1207	0.2975	0.2581	0.7182	0.1391	0.1824

Table A.14: Fit for the OSM^B model based on the validation data set.

Bibliography

- Antonini, G., Bierlaire, M., and Weber, M. (2006). Discrete Choice Models of Pedestrian Walking Behavior. *Transportation Research Part B: Methodological*, 40(8):667–687.
- Baltieri, D., Vezzani, R., and Cucchiara, R. (2011). 3DPes: 3D People Dataset for Surveillance and Forensics. In *Proceedings 1st International ACM Workshop on Multimedia access to 3D Human Objects*, pages 59–64, Scottsdale, Arizona, USA. ACM.
- Berclaz, J., Fleuret, F., Turetken, E., and Fua, P. (2011). Multiple Object Tracking Using K-Shortest Paths Optimization. *IEEE Transactions on Pattern Analysis and Machine Intelligence (PAMI)*, 33(9):1806–1819.
- Bernardin, K. and Stiefelhausen, R. (2008). Evaluating Multiple Object Tracking Performance: The CLEAR MOT Metrics. *EURASIP Journal on Image and Video Processing*, 2008:1–10.
- Berrou, J., Beecham, J., Quaglia, P., Kagarlis, M., and Gerodimos, A. (2007). Calibration and Validation of the Legion Simulation Model using Empirical Data. In *Proceedings of the Conference on Pedestrian and Evacuation Dynamics (PED 2005)*, pages 167–181, Vienna, Austria. Springer, Berlin, Heidelberg.
- Berseth, G., Kapadia, M., Haworth, B., and Faloutsos, P. (2014). SteerFit: Automated Parameter Fitting for Steering Algorithms. In *ACM SIGGRAPH/Eurographics Symposium on Computer Animation*, SCA '14, pages 113–122, Copenhagen, Denmark. ACM, New York, NY, USA.
- Bob Fisher (2010). Edinburgh Informatics Forum Pedestrian Database. <http://homepages.inf.ed.ac.uk/rbf/FORUMTRACKING/>. (accessed August 2015).
- Boltes, M. and Seyfried, A. (2013). Collecting Pedestrian Trajectories. *Neurocomputing*, 100:127–133.
- Boltes, M., Seyfried, A., Steffen, B., and Schadschneider, A. (2010). Automatic Extraction of Pedestrian Trajectories from Video Recordings. In *Proceedings of the Conference on Pedestrian and Evacuation Dynamics (PED 2008)*, pages 43–54, Wuppertal, Germany. Springer, Berlin, Heidelberg.

- Brunner, U., Kirchberger, H., Lebeda, C., Oswald, M., Könnecke, R., Kraft, M., Thoss, A., Mülli, L., Seyfried, A., Spennes, G., Hartnack, C., Wader, S., Braun, M., Tilly, R., Kretz, T., and Thumser, S. (2009). RiMEA – Richtlinie für Mikroskopische Entfluchtungs-Analysen. Guideline 2.2.1, RiMEA e.V. in German, <http://www.rimea.de/> (accessed August 2015).
- Bugaricic, H., Geers, L., and Meyer-Plate, E. (1992). *VDV-Schrift 152: Structural Requirements to Rail Vehicles for the Public Mass Transit in accordance with BOStrab*. Verband Deutscher Verkehrsbetriebe, Cologne, Germany, english edition.
- Burghardt, S., Seyfried, A., and Klingsch, W. (2013). Performance of Stairs - Fundamental Diagram and Topographical Measurements. *Transportation Research Part C: Emerging Technologies*, 37:268–278.
- Burstedde, C., Klauck, K., Schadschneider, A., and Zittartz, J. (2001). Simulation of Pedestrian Dynamics using a 2-dimensional Cellular Automaton. *Physica A*, 295:507–525.
- Calderara, S., Heinemann, U., Prati, A., Cucchiara, R., and Tishby, N. (2011). Detecting Anomalies in People’s Trajectories using Spectral Graph Analysis. *Computer Vision and Image Understanding*, 115:1099–1111.
- Campanella, M., Hoogendoorn, S., and Daamen, W. (2014). Quantitative and Qualitative Validation Procedure for General Use of Pedestrian Models. In *Proceedings of the Conference on Pedestrian and Evacuation Dynamics 2012 (PED 2012)*, pages 891–905, Zurich, Switzerland. Springer International Publishing.
- Cascetta, E. (2009). *Transportation Systems Analysis: Models and Applications*, volume 29 of *Springer Optimization and Its Applications*. Springer US, New York, NY, USA, second edition.
- Chattaraj, U., Seyfried, A., and Chakroborty, P. (2009). Comparison of Pedestrian Fundamental Diagram Across Cultures. *Advances in Complex Systems*, 12(03):393–405.
- Choi, W., Pantofaru, C., and Savarese, S. (2013). A General Framework for Tracking Multiple People from a Moving Camera. *IEEE Transactions on Pattern Analysis and Machine Intelligence (PAMI)*, 35(7):1577–1591.
- Chooramun, N., Lawrence, P. J., and Galea, E. R. (2012). An Agent Based Evacuation Model utilising Hybrid Space Discretisation. *Safety Science*, 50(8):1685–1694.
- Daamen, W. and Hoogendoorn, S. P. (2003). Experimental Research of Pedestrian Walking Behavior. *Transportation Research Record*, 1828:20–30.
- Daamen, W. and Hoogendoorn, S. P. (2006). Free Speed Distributions for Pedestrian Traffic. In *Proceedings of the Transportation Research Board 85th Annual Meeting (TRB 2006)*, pages 1–13, Washington D. C., USA. The National Academies.

- Daamen, W. and Hoogendoorn, S. P. (2012). Calibration of Pedestrian Simulation Model for Emergency Doors for Different Pedestrian Types. *Transportation Research Record: Journal of the Transportation Research Board*, 2316:69–75.
- Daniel, K., Nash, A., Koenig, S., and Felner, A. (2010). Theta*: Any-Angle Path Planning on Grids. *Journal of Artificial Intelligence Research*, 39:533–579.
- Davidich, M. and Köster, G. (2012). Towards Automatic and Robust Adjustment of Human Behavioral Parameters in a Pedestrian Stream Model to Measured Data. *Safety Science*, 50(5):1253–1260.
- Davidich, M. and Köster, G. (2013). Predicting Pedestrian Flow: A Methodology and a Proof of Concept Based on Real-Life Data. *PLoS ONE*, 8(12):e83355.
- De Boor, C. (2001). *A Practical Guide to Splines*. Springer-Verlag, New York, NY, USA, second edition.
- Dijkstra, E. W. (1959). A Note on Two Problems in Connexion with Graphs. *Numerische Mathematik*, 1(1):269–271.
- Dobler, C. and Lämmel, G. (2014). Integration of a Multi-modal Simulation Module into a Framework for Large-Scale Transport Systems Simulation. In *Proceedings of the Conference on Pedestrian and Evacuation Dynamics 2012 (PED 2012)*, pages 739–754, Zurich, Switzerland. Springer International Publishing.
- Duda, R., Hart, P., and Stork, D. (2001). *Pattern Classification*. Wiley, New York, NY, USA.
- Duives, D. C., Daamen, W., and Hoogendoorn, S. P. (2013). State-of-the-art Crowd Motion Simulation Models. *Transportation Research Part C: Emerging Technologies*, 37:193–209.
- Edie, L. (1965). Discussion of Traffic Stream Measurements and Definitions. In *Proceedings of the 2nd International Symposium On the Theory of Traffic Flow*, pages 139–154, London, UK. OECD, Paris, France.
- Eiter, T. and Mannila, H. (1994). Computing Discrete Fréchet Distance. Technical Report CD-TR 94/64, Vienna University of Technology.
- Eshel, R. and Moses, Y. (2010). Tracking in a Dense Crowd Using Multiple Cameras. *International Journal of Computer Vision*, 88(1):129–143.
- Fleuret, F., Berclaz, J., Lengange, R., and Fua, P. (2008). Multicamera People Tracking with a Probabilistic Occupancy Map. *IEEE Transactions of Pattern Analysis and Machine Intelligence*, 30(2):267–282.
- Forsyth, D. A. and Ponce, J. (2002). *Computer Vision: A Modern Approach*. Prentice Hall, New Jersey, NJ, USA, first edition.

- Frati, V. and Prattichizzo, D. (2011). Using Kinect for Hand Tracking and Rendering in Wearable Haptics. In *Proceedings of the IEEE World Haptics Conference (WHC 2011)*, pages 317–321, Istanbul, Turkey. IEEE.
- Fruin, J. J. (1971). *Pedestrian Planning and Design*. Metropolitan Association of Urban Designers and Environmental Planners, New York, NY, USA.
- Girshick, R., Shotton, J., Kohli, P., Criminisi, A., and Fitzgibbon, A. (2011). Efficient Regression of General-Activity Human Poses from Depth Images. In *Proceedings of the IEEE International Conference on Computer Vision (ICCV 2011)*, pages 415–422, Barcelona, Spain. IEEE.
- Gramoli, V. (2015). More Than You Ever Wanted to Know About Synchronization: Synchrobench, Measuring the Impact of the Synchronization on Concurrent Algorithms. In *Proceedings of the 20th ACM SIGPLAN Symposium on Principles and Practice of Parallel Programming (PPoPP 2015)*, pages 1–10, San Francisco, CA, USA. ACM, New York, NY, USA.
- Guo, R.-Y., Wong, S., Huang, H.-J., Zhang, P., and Lam, W. H. (2010). A Microscopic Pedestrian-Simulation Model and its Application to Intersecting Flows. *Physica A: Statistical Mechanics and its Applications*, 389(3):515–526.
- Gwynne, S., Kuligowski, E., Kratchman, J., and Milke, J. (2009). Questioning the Linear Relationship between Doorway Width and Achievable Flow Rate. *Fire Safety Journal*, 44(1):80–87.
- Hamacher, H., Heller, S., Klein, W., Köster, G., and Ruzika, S. (2011). A Sandwich Approach for Evacuation Time Bounds. In *Proceedings of the Conference on Pedestrian and Evacuation Dynamics (PED 2010)*, pages 503–513, Gaithersburg, MD USA. Springer, US.
- Harris, N. and Anderson, R. (2007). An International Comparison of Urban Rail Boarding and Alighting Rates. 221(4):521–526.
- Hart, P. E., Nilsson, N. J., and Raphael, B. (1968). A Formal Basis for the Heuristic Determination of Minimum Cost Paths. *IEEE Transactions on Systems Science and Cybernetics*, SSC-4(2):100–107.
- Hastie, T., Tibshirani, R., and Friedman, J. (2001). *The Elements of Statistical Learning*. Springer Series in Statistics. Springer New York Inc., New York, NY, USA.
- Heath, K. and Guibas, L. J. (2008). Multi-Person Tracking from Sparse 3d Trajectories in a Camera Sensor Network. In *Proceedings of the Second ACM/IEEE International Conference on Distributed Smart Cameras (ICDSC 2008)*, pages 1–9, Stanford, CA, US. IEEE.
- Helbing, D. (1992). A Fluid Dynamic Model for the Movement of Pedestrians. *Complex Systems*, 6:391–415.

- Helbing, D. and Johansson, A. (2009). Pedestrian, Crowd and Evacuation Dynamics. *Encyclopedia of Complexity and Systems Science*, 16(4):6476–6495.
- Helbing, D. and Molnár, P. (1995). Social Force Model for Pedestrian Dynamics. *Physical Review E*, 51:4282–4286.
- Helbing, D. and Molnár, P. (1997). Self-Organization Phenomena in Pedestrian Crowds. In *Self-Organization of Complex Structures: From Individual to Collective Dynamics*, pages 569–577. Gordon and Breach, London, UK.
- Henderson, L. F. (1971). The Statistics of Crowd Fluids. *Nature*, (229):381–383.
- Hirasaki, E., Moore, S., Raphan, T., and Cohen, B. (1999). Effects of Walking Velocity on Vertical Head and Body Movements during Locomotion. *Experimental Brain Research*, 127(2):117–130.
- Holl, S., Schadschneider, A., and Seyfried, A. (2014). Hermes: An Evacuation Assistant for Large Arenas. In *Proceedings of the Conference on Pedestrian and Evacuation Dynamics (PED 2012)*, pages 345–349, Zurich, Switzerland. Springer International Publishing.
- Hoogendoorn, S., Daamen, W., and Landman, R. (2007). Microscopic Calibration and Validation of Pedestrian Models – Cross-Comparison of Models using Experimental Data. In *Proceedings of the Conference on Pedestrian and Evacuation Dynamics 2005 (PED 2005)*, pages 253–265, Vienna, Austria. Springer Berlin Heidelberg.
- Hoogendoorn, S. P. (2003). Microscopic Simulation of Pedestrian Flows. In *Proceedings of the Transportation Research Board 82nd Annual Meeting (TRB 2003)*, pages 1–11, Washington D. C., USA. The National Academies.
- Hoogendoorn, S. P. and Bovy, P. H. L. (2000). Gas-kinetic Modeling and Simulation of Pedestrian Flows. *Transportation Research Record*, 1710:28–36.
- Hoogendoorn, S. P. and Bovy, P. H. L. (2004). Pedestrian Route-Choice and Activity Scheduling Theory and Models. *Transportation Research Part B: Methodological*, 38(2):169–190.
- Hoogendoorn, S. P. and Daamen, W. (2005). Pedestrian Behavior at Bottlenecks. *Transportation Science*, 39(2):147–159.
- Hoogendoorn, S. P., Daamen, W., and Bovy, P. H. L. (2003). Extracting Microscopic Pedestrian Characteristics from Video Data. In *Proceedings of the Transportation Research Board 82st Annual Meeting (TRB 2003)*, pages 1–15, Washington D. C., USA. The National Academies.
- Imber, M. (2011). A Unified Tooling Framework for Pedestrian Simulation. Master’s thesis, Vienna University of Technology.

- Isenhour, M. L. and Löhner, R. (2014). Verification of a Pedestrian Simulation Tool Using the NIST Recommended Test Cases. *Transportation Research Procedia*, 2(0):237–245. The Conference on Pedestrian and Evacuation Dynamics 2014 (PED 2014), 22-24 October 2014, Delft, The Netherlands.
- Izadi, S., Kim, D., Hilliges, O., Molyneaux, D., Newcombe, R., Kohli, P., Shotton, J., Hodges, S., Freeman, D., Davison, A., and Fitzgibbon, A. (2011). KinectFusion: Real-Time 3D Reconstruction and Interaction Using a Moving Depth Camera. In *Proceedings of the 24th Annual ACM Symposium on User Interface Software and Technology (UIST 2011)*, pages 559–568, Santa Barbara, CA, USA. ACM.
- Javed, O., Shafique, K., Rasheed, Z., and Shah, M. (2007). Modeling Inter-camera Spacetime and Appearance Relationships for Tracking Across Non-overlapping Views. *Computer Vision and Image Understanding*, 109(2):146–162.
- Johansson, A. and Helbing, D. (2010). Analysis of Empirical Trajectory Data of Pedestrians. In *Proceedings of the Conference on Pedestrian and Evacuation Dynamics (PED 2008)*, pages 203–214, Wuppertal, Germany. Springer, Berlin, Heidelberg.
- Johansson, A., Helbing, D., and Shukla, P. K. (2007). Specification of the Social Force Pedestrian Model by Evolutionary Adjustment to Video Tracking Data. *Advances in Complex Systems*, 10(2):271–288.
- Kirchner, A. and Schadschneider, A. (2002). Simulation of Evacuation Processes using a Bionics-inspired Cellular Automaton Model for Pedestrian Dynamics. *Physica A: Statistical Mechanics and its Applications*, 312(1-2):260–276.
- Kneidl, A., Borrmann, A., and Hartmann, D. (2012). Generation and Use of Sparse Navigation Graphs for Microscopic Pedestrian Simulation Models. *Journal Of Advanced Engineering Informatics*, 26(4):669–680.
- Ko, M., Kim, T., and Sohn, K. (2013). Calibrating a Social-Force-Based Pedestrian Walking Model based on Maximum Likelihood Estimation. *Transportation*, 40(1):91–107.
- Kogler, C., Seer, S., Matyus, T., and Stubenschrott, M. (2014). A Practical Approach to Assess the Design of Urban Transit Vehicles using Microscopic Simulations. In *Proceedings of the Transportation Research Board 93rd Annual Meeting (TRB 2014)*, pages 1–15, Washington D. C., USA. The National Academies.
- Konolige, K. and Mihelich, P. (2012). Technical Description of Kinect Calibration. http://wiki.ros.org/kinect_calibration/technical. (accessed August 2015).
- Kretz, T. (2009). Applications of the Dynamic Distance Potential Field Method. In *Traffic and Granular Flow '09*, Shanghai, China. accepted for publications.

- Lagarias, J. C., Reeds, J. A., Wright, M. H., and Wright, P. E. (1998). Convergence Properties of the Nelder-Mead Simplex Method in Low Dimensions. *SIAM Journal of Optimization*, 9:112–147.
- Lakoba, T. I., Kaup, D. J., and Finkelstein, N. M. (2005). Modifications of the Helbing-Molnar-Farkas-Vicsek Social Force Model for Pedestrian Evolution. *Simulation*, 81(5):339–352.
- Lämmel, G., Seyfried, A., and Steffen, B. (2014). Large-scale and Microscopic: A Fast Simulation Approach for Urban Areas. In *Proceedings of the Transportation Research Board 93rd Annual Meeting (TRB 2014)*, pages 1–17, Washington D. C., USA. The National Academies.
- Løvås, G. (1994). Modeling and Simulation of Pedestrian Traffic Flow. *Transportation Research Part B: Methodological*, 28:429–443.
- Loy, C., Xiang, T., and Gong, S. (2009). Multi-camera Activity Correlation Analysis. In *Proceedings IEEE Intl. Conference on Computer Vision and Pattern Recognition (CVPR 2009)*, pages 1988–1995, Miami, FL, USA. IEEE.
- Massey, F. J. (1951). The Kolmogorov-Smirnov Test for Goodness of Fit. *Journal of the American Statistical Association*, 46(253):68–78.
- Mavrinac, A., Chen, X., and Tepe, K. (2010). An Automatic Calibration Method for Stereo-based 3D Distributed Smart Camera Networks. *Computer Vision and Image Understanding*, 114(8):952–962.
- Microsoft Corp. (2012a). Kinect for Xbox 360. Redmond, WA, USA.
- Microsoft Corp. (2012b). Microsoft Kinect for Windows SDK. <http://www.microsoft.com/en-us/kinectforwindows/>. (accessed August 2015).
- Moussaïd, M., Helbing, D., Garnier, S., Johansson, A., Combe, M., and Theraulaz, G. (2009). Experimental Study of the Behavioural Mechanisms underlying Self-organization in Human Crowds. *Proceedings of the Royal Society - Biological Sciences*, 276(1668):2755–2762.
- Moussaïd, M., Helbing, D., and Theraulaz, G. (2011). How Simple Rules Determine Pedestrian Behavior and Crowd Disasters. *Proceedings of the National Academy of Sciences*, 108(17):6884–6888.
- Moussaïd, M., Perozo, N., Garnier, S., Helbing, D., and Theraulaz, G. (2010). The Walking Behaviour of Pedestrian Social Groups and Its Impact on Crowd Dynamics. *PLoS ONE*, 5(4):e10047.
- Noonan, P. J., Cootes, T. F., Hallett, W. A., and Hinz, R. (2011). The Design and Initial Calibration of an Optical Tracking System using the Microsoft Kinect. In *Proceedings of the IEEE Nuclear Science Symposium and Medical Imaging Conference (NSS/MIC 2011)*, pages 3614–3617, Valencia, Spain. IEEE.

- Oh, S., Hoggs, A., Perero, A., Cuntoor, N., Chen, C., Lee, J., Mikherjee, S., Aggarwal, J., Lee, H., Davis, L., Swears, E., Wang, X., Ji, Q., Reddy, K., Shah, M., Vondrick, C., Pirsiavash, H., Ramanan, D., Yuen, J., Torralba, A., Song, B., Fong, A., Roy-Chowdhury, A., and M., D. (2011). A Large-scale Benchmark Dataset for Event Recognition in Surveillance Video. In *Proceedings IEEE Conference on Computer Vision and Pattern Recognition (CVPR 2011)*, pages 3153–3160, Colorado Springs, CO, USA. IEEE.
- Parisi, D. R., Gilman, M., and Moldovan, H. (2009). A Modification of the Social Force Model can Reproduce Experimental Data of Pedestrian Flows in Normal Conditions. *Physica A: Statistical Mechanics and its Applications*, 388(17):3600–3608.
- Pellegrini, S., Ess, A., Schindler, K., and van Gool, L. (2009). You’ll Never Walk Alone: Modeling Social Behavior for Multi-Target Tracking. In *Proceedings of the IEEE International Conference on Computer Vision (ICCV 2009)*, pages 261–268, Kyoto, Japan. IEEE.
- PETS (2009). PETS Dataset - Performance Evaluation of Tracking and Surveillance. <http://www.cvg.reading.ac.uk/PETS2009/>. (accessed August 2015).
- Pflugfelder, R. and Bischof, H. (2010). Localization and Trajectory Reconstruction in Surveillance Cameras with Non Overlapping Views. *IEEE Transactions of Pattern Analysis and Machine Intelligence*, 34(2):709–721.
- Plaue, M., Chen, M., Bärwolff, G., and Schwandt, H. (2011). Trajectory Extraction and Density Analysis of Intersecting Pedestrian Flows from Video Recordings. In *Proceedings of the 2011 ISPRS Conference on Photogrammetric Image Analysis (PIA 2011)*, pages 285–296, Munich, Germany. Springer, Berlin, Heidelberg.
- Predtetschenski, W. M. and Milinski, A. I. (1971). *Personenströme in Gebäuden – Berechnungsmethoden für die Projektierung*. Verlagsgesellschaft Rudolf Müller, Köln-Braunsfeld.
- Rastogi, R., Ilango, T., and Chandra, S. (2013). Pedestrian Flow Characteristics for Different Pedestrian Facilities and Situations. *European Transport*, 53:1–21.
- Rodríguez, G. (2007). Lecture Notes on Generalized Linear Models.
- Rogsch, C., Klüpfel, H., Könnecke, R., and Winkens, A. (2014). RiMEA: A Way to Define a Standard for Evacuation Calculations. In *Proceedings of the Conference on Pedestrian and Evacuation Dynamics 2012 (PED 2012)*, pages 455–467, Zurich, Switzerland. Springer International Publishing.
- Ronchi, E., Kuligowski, E. D., Reneke, P. A., Peacock, R. D., and Nilsson, D. (2013). The Process of Verification and Validation of Building Fire Evacuation Models. Technical Report 1822, National Institute of Standards and Technology.

- Rudloff, C., Bauer, D., Matyus, T., and Seer, S. (2011a). Mind The Gap: Boarding and Alighting Processes using the Social Force Paradigm Calibrated on Experimental Data. In *14th International IEEE Conference on Intelligent Transportation Systems (ITSC 2011)*, pages 353–358, Washington, D.C., USA. IEEE.
- Rudloff, C., Matyus, T., and Seer, S. (2014). Comparison of Different Calibration Techniques on Simulated Data. In *Proceedings of the Conference on Pedestrian and Evacuation Dynamics 2012 (PED 2012)*, pages 657–672. Springer International Publishing, Zurich, Switzerland.
- Rudloff, C., Matyus, T., Seer, S., and Bauer, D. (2011b). Can Walking Behavior be Predicted? An Analysis of the Calibration and Fit of Pedestrian Models. *Transportation Research Record*, 2264:101–109.
- Seer, S., Bauer, D., Brändle, N., and Ray, M. (2008). Estimating Pedestrian Movement Characteristics for Crowd Control at Public Transport Facilities. In *11th International IEEE Conference on Intelligent Transportation Systems (ITSC 2008)*, pages 742–747, Beijing, China. IEEE.
- Seer, S., Brändle, N., and Ratti, C. (2014a). Kinects and Human Kinetics: A New Approach for Studying Pedestrian Behavior. *Transportation Research Part C: Emerging Technologies*, 48:212–228.
- Seer, S., Rudloff, C., Matyus, T., and Brändle, N. (2014b). Validating Social Force based Models with Comprehensive Real World Motion Data. *Transportation Research Procedia*, 2:724–732. The Conference on Pedestrian and Evacuation Dynamics 2014 (PED 2014), 22-24 October 2014, Delft, The Netherlands.
- Seitz, M. J. and Köster, G. (2012). Natural Discretization of Pedestrian Movement in Continuous Space. *Phys. Rev. E*, 86:046108.
- Seitz, M. J. and Köster, G. (2014). How Update Schemes influence Crowd Simulations. *Journal of Statistical Mechanics: Theory and Experiment*, 2014(7):P07002.
- Sethian, J. (1999). *Level Set Methods and Fast Marching Methods: Evolving Interfaces in Computational Geometry, Fluid Mechanics, Computer Vision, and Materials Science*. Cambridge Monographs on Applied and Computational Mathematics. Cambridge University Press, New York, NY, USA.
- Seyfried, A., Boltes, M., Kähler, J., Klingsch, W., Portz, A., Rupperecht, T., Schadschneider, A., Steffen, B., and Winkens, A. (2010). Enhanced Empirical Data for the Fundamental Diagram and the Flow Through Bottlenecks. In *Proceedings of the Conference on Pedestrian and Evacuation Dynamics (PED 2008)*, pages 145–156, Wuppertal, Germany. Springer Berlin Heidelberg.
- Seyfried, A., Steffen, B., and Lippert, T. (2006). Basics of Modelling the Pedestrian Flow. *Physica A: Statistical Mechanics and its Applications*, 368(1):232–238.

- Shi, C., Zhong, M., Nong, X., He, L., Shi, J., and Feng, G. (2012). Modeling and safety strategy of passenger evacuation in a metro station in china. *Safety Science*, 50(5):1319–1332.
- Shotton, J., Fitzgibbon, A., Cook, M., Sharp, T., Finocchio, M., Moore, R., Kipman, A., and Blake, A. (2011). Real-Time Human Pose Recognition in Parts from Single Depth Images. In *Proceedings of the IEEE Conference on Computer Vision and Pattern Recognition (CVPR 2011)*, pages 1297–1304, Colorado Springs, CO, USA. IEEE.
- Sochman, J. and Hogg, D. (2011). Who Knows Who – Inverting the Social Force Model for Finding Groups. In *IEEE International Conference on Computer Vision Workshops (ICCV Workshops)*, pages 830–837, Barcelona, Spain. IEEE.
- Stauffer, C. and Grimson, W. E. L. (2000). Learning Patterns of Activity Using Real-Time Tracking. *IEEE Transactions on Pattern Analysis and Machine Intelligence (PAMI)*, 22(8):747–757.
- Steffen, B. and Seyfried, A. (2010). Methods for Measuring Pedestrian Density, Flow, Speed and Direction with Minimal Scatter. *Physica A: Statistical Mechanics and its Applications*, 389(9):1902–1910.
- Sternig, S., Mauthner, T., Irschara, A., Roth, P., and Bischof, H. (2011). Multi-camera Multi-object Tracking by Robust Hough-based Homography Projections. In *Proceedings of the Eleventh IEEE International Workshop on Visual Surveillance (ICCV Workshops)*, pages 1689–1696, Barcelona, Spain. IEEE.
- Stubenschrott, M., Kogler, C., Matyus, T., and Seer, S. (2014). A Dynamic Pedestrian Route Choice Model Validated in a High Density Subway Station. *Transportation Research Procedia*, 2:376–384. The Conference on Pedestrian and Evacuation Dynamics 2014 (PED 2014), 22-24 October 2014, Delft, The Netherlands.
- The Apache Software Foundation (2014). ActiveMQ. <http://activemq.apache.org/>. (accessed August 2015).
- United Nations (2014). World Urbanization Prospects: The 2014 Revision, (ST/ESA/SER.A/366). Technical report, Department of Economic and Social Affairs, Population Division.
- University of Cyprus Computer Graphics Lab (2011). Crowds-by-Example Data Set. <https://graphics.cs.ucy.ac.cy/research/downloads/crowd-data>. (accessed August 2015).
- van den Berg, J., Guy, S. J., Lin, M. C., and Manocha, D. (2011). Reciprocal n-Body Collision Avoidance. In *Robotics Research*, volume 70 of *Springer Tracts in Advanced Robotics*, pages 3–19. Springer Berlin Heidelberg.

- Wagoum, A., Chraïbi, M., Eilhardt, C., Nowak, S., Kulkov, I., Weber, D., Sauer, K., Klüpfel, H., and Schadschneider, A. (2014). OpenPedSim: A Framework for Pedestrian Flow Analysis. In *Proceedings of the Conference on Pedestrian and Evacuation Dynamics 2012 (PED 2012)*, pages 1323–1330, Zurich, Switzerland. Springer International Publishing.
- Wang, H., Su, H., Zheng, K., Sadiq, S., and Zhou, X. (2013). An Effectiveness Study on Trajectory Similarity Measures. In *Proceedings of the Twenty-Fourth Australasian Database Conference - Volume 137, ADC '13*, pages 13–22, Darlinghurst, Australia, Australia. Australian Computer Society, Inc.
- Weidmann, U. (1993). Transporttechnik der Fussgänger - Transporttechnische Eigenschaften des Fussgängerverkehrs (Literaturstudie). Literature Research 90, Institut für Verkehrsplanung, Transporttechnik, Strassen- und Eisenbahnbau IVT an der ETH Zürich, Zurich, Switzerland. in German.
- Weiss, A., Hirshberg, D., and Black, M. (2011). Home 3D Body Scans from Noisy Image and Range Data. In *Proceedings of the IEEE International Conference on Computer Vision (ICCV 2011)*, pages 1951–1958, Barcelona, Spain. IEEE.
- Zeiler, I., Rudloff, C., and Bauer, D. (2011). Modelling Random Taste Variations on Level Changes in Passenger Route Choice in a Public Transport Station. In *Proceedings of the Conference on Pedestrian and Evacuation Dynamics 2010 (PED 2010)*, pages 185–195, Gaithersburg, MD USA. Springer.
- Zhang, J., Britto, D., Chraïbi, M., Löhner, R., Haug, E., and Gawenat, B. (2014). Quantitative Validation of PEDFLOW for Description of Unidirectional Pedestrian Dynamics. *Transportation Research Procedia*, 2:733–738. The Conference on Pedestrian and Evacuation Dynamics 2014 (PED 2014), 22-24 October 2014, Delft, The Netherlands.

Abbreviations

CA	Cellular Automaton
CAD	Computer-Aided Design
CSV	Comma-Separated Values
FD	Fundamental Diagram
GUI	Graphical User Interface
KDE	Kernel Density Estimation
MOTP	Multiple Object Tracking Precision
NIST	United States' National Institute of Standards and Technology
OD	Origin-Destination
ORCA	Optimal Reciprocal Collision Avoidance
OSM	Optimal Steps Model
PDR	Pedestrian Detection Rate
RMSE	Root-Mean-Square Error
RiMEA	Richtlinie für Mikroskopische Evakuierungs Analysen - Guideline for Microscopic Evacuation Analyses
SF	Social Force
SSE	Sum of Squared Error
TS	Trajectory Similarity
WT	Walking Time
XML	Extensible Markup Language

STEFAN SEER

PERSONAL INFORMATION

Born in Vienna, Austria, November 28th, 1981

email stefan.seer@gmail.com

website <http://www.stefanseer.com>

WORK EXPERIENCE

2005 – Present Scientist, AIT AUSTRIAN INSTITUTE OF TECHNOLOGY

Leader of the "Dynamic Crowd Solutions" research group. Development of models and algorithms for pedestrian flow simulation including technologies to collect and analyze data on crowd behavior in the context of urban transportation. Project leader of the AIT-MIT cooperation on "Persuasive Urban Mobility" (with MIT Media Lab) and on "Perception Based Modeling" (with MIT SENSEable City Lab).

Reference: Christian CHIMANI · +43 50550-6233 · christian.chimani@ait.ac.at

2011 – 2012 Visiting Researcher, MIT Massachusetts Institute of Technology

Research at the MIT SENSEable City Lab on novel methods for collecting movement data of crowd dynamics based on the Microsoft Kinect. (see also <http://senseable.mit.edu/kinectkinetics/>).

Reference: Prof. Carlo RATTI · +1 617-2537926 · ratti@mit.edu

EDUCATION

2008 – 2015 Vienna University of Technology

Doctoral Degree in Technical Sciences · Faculty of Informatics

Thesis: *A Unified Framework for Evaluating Microscopic Pedestrian Simulation Models*

Description: This thesis developed a framework that constitutes an optimal basis for structured investigation on strengths and weaknesses of various microscopic pedestrian movement simulation models.

Advisor: Prof. Frank RATTAY · +43 1-58801-10114 · frank.rattay@tuwien.ac.at

2001 – 2004 University of Applied Sciences Technikum Wien

Masters Degree in Electronics Engineering · Department of Electronics

Description: This degree focused on Computer Science and Systems Technology, and Audio- and Video Engineering.

1995 – 2000 Higher Technical Education Institute TGM

University Entrance Qualification – A levels · Department of Electronics

Description: This degree focused on Electronics and Biomedical Engineering.

AWARDS

2008

National Award for Traffic 2008

Awarded by the Austrian Ministry for Transport, Innovation and Technology (BMVIT) in the category *Logistic Traffic Solutions at Major Events* for the project RAVE.

2006

Best Poster Paper Award

"Pedestrian Detection and Tracking for Counting Applications in Crowded Situations" with O. Sidla, Y. Lypetsky and N. Brändle, IEEE International Conference on Advanced Video and Signal based Surveillance (AVSS2006), Sydney, Australia.

PUBLICATIONS

M. Wunsch, A. Stibe, A. Millonig, S. Seer, C. Dai, K. Schechtner and R. C. C. Chin, "What Makes You Bike? Exploring Persuasive Strategies to Encourage Low-Energy Mobility", In: *Persuasive Technology*, Springer International Publishing, Volume 9072, ISBN: 978-3-319-20305-8, DOI: 10.1007/978-3-319-20306-5_5, pp. 53-64, 2015.

S. Seer, N. Brändle and C. Ratti, "Kinects and Human Kinetics: A New Approach for Studying Pedestrian Behavior", In: *Transportation Research Part C: Emerging Technologies*, DOI: 10.1016/j.trc.2014.08.012, pp. 212-228, 2014.

S. Seer, C. Rudloff, T. Matyus and N. Brändle, "Validating Social Force Based Models with Comprehensive Real World Motion Data", In: *Transportation Research Procedia*, Volume 2, pp. 724-732, ISSN 2352-1465, 2014.

M. Stubenschrott, C. Kogler, T. Matyus and S. Seer, "A Dynamic Pedestrian Route Choice Model Validated in a High Density Subway Station", In: *Transportation Research Procedia*, Volume 2, pp. 376-384, ISSN 2352-1465, 2014.

H. Schrom-Feiertag, C. Schinko, V. Settgast and S. Seer, "Evaluation of Guidance Systems in Public Infrastructures Using Eye Tracking in an Immersive Virtual Environment", In: *Proceedings of the 2nd International Workshop on Eye Tracking for Spatial Research (ET4S2014)*, Vienna, Austria, September 23, 2014.

C. Kogler, S. Seer, T. Matyus and M. Stubenschrott, "A Practical Approach to Assess the Design of Urban Transit Vehicles using Microscopic Simulations", In: *Proceedings of the Transportation Research Board 93rd Annual Meeting (TRB2014)*, Washington, D.C., USA, January, 2014.

C. Rudloff, T. Matyus and S. Seer, "Comparison of different Calibration Techniques on Simulated Data", In: *Proceedings of the 6th International Conference on Pedestrian and Evacuation Dynamics (PED2012)*, ISBN: 978-3-319-02446-2, pp. 657-672, Zurich, Switzerland, 2012.

C. Rudloff, D. Bauer, T. Matyus and S. Seer, "Mind the gap: Boarding and Alighting Processes using the Social Force Paradigm Calibrated on Experimental Data", In: *Proceedings of the 14th International IEEE Annual Conference on Intelligent Transportation Systems (ITSC2011)*, Washington, D.C., USA, October 5-7, 2011.

C. Rudloff, T. Matyus, S. Seer and D. Bauer, "Can walking behavior be predicted? An analysis of the calibration and fit of pedestrian models", In: *Transportation Research Record*, Volume 2264, ISSN: 0361-1981, pp. 101-109, 2011.

D. Bauer, M. Ray and S. Seer, "Using Simple Sensors for Measuring Service Times and Counting Pedestrians: Strengths and Weaknesses", In: Transportation Research Record, Volume 2214, ISSN: 0361-1981, pp. 77-84, 2011.

D. Bauer, N. Brändle, S. Seer, M. Ray and K. Kitazawa, "Measurement of Pedestrian Movements: A Comparative Study on Various Existing Systems", In: Pedestrian Behaviour: Models, Data Collection and Application, H. Timmermanns, G. Imho (Hrg.); Emerald Group, Publishing Limited, Bingley BD16 1WA, United Kingdom, ISBN: 978-1-84855-750-5, pp. 301-320, 2009.

S. Seer, D. Bauer, N. Brändle and M. Ray, "Estimating Pedestrian Movement Characteristics for Crowd Control at Public Transport Facilities", In: Proceedings of the 11th International IEEE Conference on Intelligent Transportation Systems (ITSC2008), Beijing, China, 2008.

S. Seer, D. Bauer and N. Brändle. "Design of Decision Rules for Crowd Controlling using Macroscopic Pedestrian Flow Simulation", In: Proceedings of the 4th International Conference on Pedestrian and Evacuation Dynamics (PED2008), Wuppertal, Germany, 2008.

D. Bauer, S. Seer and N. Brändle. "Macroscopic Pedestrian Flow Simulation for Designing Crowd Control Measures in Public Transport after Special Events", In: Proceedings of the Summer Computer Simulation Conference (SCSC2007), San Diego, USA, July 15-18, 2007.

O. Sidla, Y. Lypetsky, N. Brändle and S. Seer. "Pedestrian Detection and Tracking for Counting Applications in Crowded Situations", In: Proceedings of the IEEE International Conference on Advanced Video and Signal based Surveillance (AVSS2006), Sydney, Australia, November, 2006.

N. Brändle, D. Bauer and S. Seer. "Track-based Finding of Stopping Pedestrians - A Practical Approach for Analyzing a Public Infrastructure". In: Proceedings of the 9th International IEEE Conference on Intelligent Transportation Systems (ITSC2006), Toronto, Canada, 2006.

D. Bauer, N. Brändle, S. Seer and R. Pflugfelder. "Finding Highly Frequent Paths in Video Sequences". In: Proceedings of the 18th International Conference on Pattern Recognition (ICPR2006), Hong Kong. August 20-24, 2006.

PROGRAM COMMITTEE MEMBER

Workshop on Complex Collective Systems (CCS 2015), Conference on Cellular Automata for Research and Industry (ACRI 2014)

REVIEWER

Computer-Aided Civil and Infrastructure Engineering (CACAIIE), Public Transport: Planning and Operations, Mathematical Biosciences and Engineering (MBE), Transportation Research Part C: Emerging Technologies (TRC), IEEE Intelligent Transportation Systems Conference (ITSC)